

DTIC FILE COPY

2

AD-A227 581

TECHNICAL REPORT BRL-TR-3153

BRL

EVALUATION OF THE HULL AND SHARC HYDROCODES
IN SIMULATING THE REFLECTION OF
A MACH 2.12 NON-DECAYING SHOCK
ON WEDGES OF VARIOUS ANGLES

DTIC
SELECTE
OCT 11 1990
S
D
D
ce

RICHARD E. LOTTERO
JOHN D. WORTMAN

SEPTEMBER 1990

APPROVED FOR PUBLIC RELEASE; DISTRIBUTION UNLIMITED.

U.S. ARMY LABORATORY COMMAND

BALLISTIC RESEARCH LABORATORY
ABERDEEN PROVING GROUND, MARYLAND

NOTICES

Destroy this report when it is no longer needed. DO NOT return it to the originator.

Additional copies of this report may be obtained from the National Technical Information Service, U.S. Department of Commerce, 5285 Port Royal Road, Springfield, VA 22161.

The findings of this report are not to be construed as an official Department of the Army position, unless so designated by other authorized documents.

The use of trade names or manufacturers' names in this report does not constitute indorsement of any commercial product.

UNCLASSIFIED

REPORT DOCUMENT PAGE			<i>Form Approved</i> <i>OMB No. 0704-0188</i>
Public reporting burden for this collection of information is estimated to average 1 hour per response, including the time for reviewing instructions, searching existing data sources, gathering and maintaining the data needed, and completing and reviewing the collection of information. Send comments regarding this burden estimate or any other aspect of this collection of information, including suggestions for reducing this burden, to Washington Headquarters Services, Directorate for Information Operations and Reports, 1215 Jefferson Davis Highway, Suite 1204, Arlington, VA 22202-4302, and to the Office of Management and Budget, Paperwork Reduction Project(0704-0188), Washington, DC 20503.			
1. AGENCY USE ONLY (Leave blank)	2. REPORT DATE September 1990	3. REPORT TYPE AND DATES COVERED Final, Aug 89 - Jul 90	
4. TITLE AND SUBTITLE Evaluation of the HULL and SHARC Hydrocodes in Simulating the Reflection of a Mach 2.12 Non-Decaying Shock on Wedges of Various Angles		5. FUNDING NUMBERS 1L162120AH25	
6. AUTHOR(S) Richard E. Lottero John D. Wortman		8. PERFORMING ORGANIZATION REPORT NUMBER	
7. PERFORMING ORGANIZATION NAME(S) AND ADDRESS(ES) Director U.S. Army Ballistic Research Laboratory ATTN: SLCBR-TB-BD Aberdeen Proving Ground, MD 21005-5066			
9. SPONSORING/MONITORING AGENCY NAMES(S) AND ADDRESS(ES) Director US Army Ballistic Research Laboratory ATTN: SLCBR-DD-T Aberdeen Proving Ground, MD 21005-5066		10. SPONSORING/MONITORING AGENCY REPORT NUMBER BRL-TR-3153	
11. SUPPLEMENTARY NOTES Research was performed under the auspices of the U.S. Army Harry Diamond Laboratories, ATTN: SLCHD-NW-P, 2800 Powder Mill Road, Adelphi, MD 20783-1197.			
12a. DISTRIBUTION/AVAILABILITY STATEMENT Approved for public release; distribution is unlimited.		12b. DISTRIBUTION CODE	
13. ABSTRACT (Maximum 200 words) Hydrodynamic computer code simulations of the interaction of a non-decaying Mach 2.12 shock wave with wedges of various angles are presented. Techniques for simulating this interaction with the HULL and SHARC hydrocodes are evaluated by running the codes in various geometric configurations commonly used to simulate Mach reflection. Fluid dynamics aspects of each geometry are evaluated and discussed. The codes are also run with systematic variations in differencing method and artificial viscosity options. Most of these variations are done in the SHARC code computations. SHARC also includes the option of using half hydrodynamic and half rigid flow field cells to simulate a smooth wedge surface in a rectangular finite difference grid. These computations are based on experimental and computational work performed at the Ernst Mach Institute, Freiburg, Federal Republic of Germany.			
14. SUBJECT TERMS Shock Waves, Blast Waves, Mach Reflection, HULL Hydrocode, SHARC Hydrocode, STEALTH Hydrocode, BLAST2D Hydrocode, Shock on Wedge		15. NUMBER OF PAGES 122	
17. SECURITY CLASSIFICATION OF REPORT UNCLASSIFIED		16. PRICE CODE	
		20. LIMITATION OF ABSTRACT UNLIMITED	
18. SECURITY CLASSIFICATION OF THIS PAGE UNCLASSIFIED	19. SECURITY CLASSIFICATION OF ABSTRACT UNCLASSIFIED		

INTENTIONALLY LEFT BLANK.

Acknowledgement

The authors wish to thank Dr. Werner Heilig of the Ernst Mach Institute, Freiburg, Federal Republic of Germany, for his guidance and assistance in providing the data describing the experiment on which this work is based, in providing results from his computations with the STEALTH hydrocode for comparison, and for his permission to reproduce some of his plots in this report. Thanks are extended to Ms. Dixie M. Hisley, a colleague at the BRL, for providing an informational subset of her results from her BLAST2D hydrocode for the same problem. Thanks are also extended to Drs. Jonas A. Zukas and W. Don Allison for their reviews of this report and helpful comments.



Accession For	
NTIS CRA&I	<input checked="" type="checkbox"/>
DTIC TAB	<input type="checkbox"/>
Unannounced	<input type="checkbox"/>
Justification	
By	
Distribution /	
Availability Codes	
Dist	Avail and/or Special
A-1	

INTENTIONALLY LEFT BLANK.

Table of Contents

	<u>Page</u>
List of Figures	vii
List of Tables	xiii
I. Introduction	1
II. The Experiment at the Ernst Mach Institute	2
III. The Hydrocode Computations at the Ernst Mach Institute	4
1. The EMI 30 Degree Wedge Computation	4
2. The EMI 60 Degree Wedge Computation	10
IV. The Hydrocode Computations at the BRL	11
1. The 30 Degree Wedge	19
a. The Basic Grid for the 30 Degree Wedge on a Reflecting Plane	19
b. SHARC Computations 9003.23 and 9002.12	22
c. SHARC Computations 9003.23, 9003.26, 9003.27, and 9003.28	32
d. HULL122 Computations 8912.071 and 9001.181	40
e. SHARC Computations 9003.23 and 9003.121, and HULL122 9001.181	50
f. SHARC 9003.23, HULL122 9001.181, BLAST2D, and EMI STEALTH Computations	60
g. SHARC 9003.23, 9003.30, and 9003.121 Computations	66
2. The 60 Degree Wedge	75
a. SHARC Computations 9003.121 and 9003.251, and HULL122 Computation 9001.181	75
3. The 45 Degree Wedge	84
a. SHARC Computation 9003.241 and HULL122 Computation 9001.031	86
V. Conclusion	97
References	101
Distribution List	103

INTENTIONALLY LEFT BLANK.

List of Figures

<u>Figure</u>		<u>Page</u>
1	Regions of RR, SMR, CMR, and DMR and Their Transition Boundaries in the M_I , Θ Plane for Polytropic Air ($\gamma = 1.4$, Solid Lines) and Calorically Imperfect Air (Variable γ , Broken Lines).	1
2	The EMI Shock Tube. (Courtesy of W. Heilig, EMI.)	2
3	Single Mach Reflection. (Courtesy of W. Heilig, EMI.)	3
4	EMI 30 Degree Wedge Computational Grid. (Courtesy of W. Heilig, EMI.)	6
5	Absolute Static Pressures at Point <i>A</i> , EMI 30 Degree Wedge Computation. (Courtesy of W. Heilig, EMI.)	7
6	Absolute Static Pressures at Point <i>B</i> , EMI 30 Degree Wedge Computation. (Courtesy of W. Heilig, EMI.)	8
7	Absolute Static Pressures at Point <i>C</i> , EMI 30 Degree Wedge Computation. (Courtesy of W. Heilig, EMI.)	9
8	Absolute Static Pressures at Point <i>D</i> , EMI 30 Degree Wedge Computation. (Courtesy of W. Heilig, EMI.)	10
9	Absolute Static Pressures at Point <i>E</i> , EMI 30 Degree Wedge Computation. (Courtesy of W. Heilig, EMI.)	11
10	Absolute Static Pressures at Point <i>F</i> , EMI 30 Degree Wedge Computation. (Courtesy of W. Heilig, EMI.)	12
11	EMI 60 Degree Wedge Computation. (Courtesy of W. Heilig, EMI.)	12
12	Shock Interaction with a Wedge Approximated by a Rigid Stair Step Surface, Mounted on a Reflecting Ground Plane.	14
13	Shock Interaction with a Smooth Wedge Mounted on a Reflecting Ground Plane.	15
14	Shock Interaction with a Rectangular Block in the Flow Field, Rotated Shock and Orthogonally Positioned Block.	17
15	Interaction of a Rotated Shock with an Infinite Reflecting Plane on the Boundary of the Flow Field.	18
16	SHARC Problem 9003.23, 30 Degree Smooth Wedge, Absolute Pressure Contours at 50 μs	22
17	SHARC Problem 9003.23, 30 Degree Smooth Wedge, Density Contours at 50 μs	24

List of Figures (Continued)

<u>Figure</u>		<u>Page</u>
18	SHARC Problem 9002.12, 30 Degree Stair Step Wedge, Absolute Pressure Contours at 50 μ s.	25
19	SHARC Problem 9002.12, 30 Degree Stair Step Wedge, Density Contours at 50 μ s.	26
20	SHARC Problems 9003.23 and 9002.12, Absolute Pressure at Point A_w^{30}	27
21	SHARC Problems 9003.23 and 9002.12, Absolute Pressure at Point B_w^{30}	28
22	SHARC Problems 9003.23 and 9002.12, Absolute Pressure at Point C_w^{30}	29
23	SHARC Problems 9003.23 and 9002.12, Absolute Pressure at Point D_w^{30}	30
24	SHARC Problems 9003.23 and 9002.12, Absolute Pressure at Point E_w^{30}	31
25	SHARC Problems 9003.23 and 9002.12, Absolute Pressure at Point F_w^{30}	32
26	SHARC Problems 9003.23, 9003.26, 9003.27, and 9003.28, Absolute Pressure at Point A_w^{30}	33
27	SHARC Problems 9003.23, 9003.26, 9003.27, and 9003.28, Absolute Pressure at Point B_w^{30}	35
28	SHARC Problems 9003.23, 9003.26, 9003.27, and 9003.28, Absolute Pressure at Point C_w^{30}	36
29	SHARC Problems 9003.23, 9003.26, 9003.27, and 9003.28, Absolute Pressure at Point D_w^{30}	37
30	SHARC Problems 9003.23, 9003.26, 9003.27, and 9003.28, Absolute Pressure at Point E_w^{30}	38
31	SHARC Problems 9003.23, 9003.26, 9003.27, and 9003.28, Absolute Pressure at Point F_w^{30}	39
32	HULL122 Problem 8912.071, 30 Degree Stair Step Wedge, Absolute Pressure Contours at 50 μ s.	40
33	HULL122 Problem 8912.071, 30 Degree Stair Step Wedge, Density Contours at 50 μ s.	41
34	HULL122 Problem 9001.181, 30 Degree Smooth Wedge (Bottom) and 60 Degree Smooth Wedge (Left), Absolute Pressure Contours at 50 μ s.	42
35	HULL122 Problem 9001.181, 30 Degree Smooth Wedge (Bottom) and 60 Degree Smooth Wedge (Left), Density Contours at 50 μ s.	43

List of Figures (Continued)

<u>Figure</u>		<u>Page</u>
36	HULL122 Problems 8912.071 and 9001.181, Absolute Pressure at Points A_w^{30} and A_{bb}^{30} , Respectively.	45
37	HULL122 Problems 8912.071 and 9001.181, Absolute Pressure at Points B_w^{30} and B_{bb}^{30} , Respectively.	46
38	HULL122 Problems 8912.071 and 9001.181, Absolute Pressure at Points C_w^{30} and C_{bb}^{30} , Respectively.	47
39	HULL122 Problems 8912.071 and 9001.181, Absolute Pressure at Points D_w^{30} and D_{bb}^{30} , Respectively.	48
40	HULL122 Problems 8912.071 and 9001.181, Absolute Pressure at Points E_w^{30} and E_{bb}^{30} , Respectively.	49
41	HULL122 Problems 8912.071 and 9001.181, Absolute Pressure at Points F_w^{30} and F_{bb}^{30} , Respectively.	50
42	SHARC Problem 9003.121, 30 Degree Smooth Wedge (Bottom) and 60 Degree Smooth Wedge (Left), Absolute Pressure Contours at 50 μs	52
43	SHARC Problem 9003.121, 30 Degree Smooth Wedge (Bottom) and 60 Degree Smooth Wedge (Left), Density Contours at 50 μs	53
44	SHARC Problems 9003.23 and 9003.121, and HULL122 Problem 9001.181, Absolute Pressure at Points A_w^{30} and A_{bb}^{30}	54
45	SHARC Problems 9003.23 and 9003.121, and HULL122 Problem 9001.181, Absolute Pressure at Points B_w^{30} and B_{bb}^{30}	55
46	SHARC Problems 9003.23 and 9003.121, and HULL122 Problem 9001.181, Absolute Pressure at Points C_w^{30} and C_{bb}^{30}	56
47	SHARC Problems 9003.23 and 9003.121, and HULL122 Problem 9001.181, Absolute Pressure at Points D_w^{30} and D_{bb}^{30}	57
48	SHARC Problems 9003.23 and 9003.121, and HULL122 Problem 9001.181, Absolute Pressure at Points E_w^{30} and E_{bb}^{30}	58
49	SHARC Problems 9003.23 and 9003.121, and HULL122 Problem 9001.181, Absolute Pressure at Points F_w^{30} and F_{bb}^{30}	59
50	SHARC 9003.23, HULL122 9001.181, EMI STEALTH, and the BLAST2D Computations, Absolute Pressure at Points A_w^{30} , A_{bb}^{30} , and A	60
51	SHARC 9003.23, HULL122 9001.181, EMI STEALTH, and the BLAST2D Computations, Absolute Pressure at Points B_w^{30} , B_{bb}^{30} , and B	61

List of Figures (Continued)

<u>Figure</u>		<u>Page</u>
52	SHARC 9003.23, HULL122 9001.181, EMI STEALTH, and the BLAST2D Computations, Absolute Pressure at Points C_w^{30} , C_{bb}^{30} , and C	62
53	SHARC 9003.23, HULL122 9001.181, EMI STEALTH, and the BLAST2D Computations, Absolute Pressure at Points D_w^{30} , D_{bb}^{30} , and D	63
54	SHARC 9003.23, HULL122 9001.181, EMI STEALTH, and the BLAST2D Computations, Absolute Pressure at Points E_w^{30} , E_{bb}^{30} , and E	64
55	SHARC 9003.23, HULL122 9001.181, EMI STEALTH, and the BLAST2D Computations, Absolute Pressure at Points F_w^{30} , F_{bb}^{30} , and F	65
56	SHARC Problem 9003.30, 30 Degree Smooth "Wedge," (Rotated Shock and Infinite Plane), Pressure Contours at 50 μ s.	67
57	SHARC Problem 9003.30, 30 Degree Smooth "Wedge," (Rotated Shock and Infinite Plane), Density Contours at 50 μ s.	68
58	SHARC Computations 9003.23, 9003.30, and 9003.121, Absolute Pressure at Points A_w^{30} , A_{pt}^{30} , and A_{bb}^{30} , Respectively.	69
59	SHARC Computations 9003.23, 9003.30, and 9003.121, Absolute Pressure at Points B_w^{30} , B_{pt}^{30} , and B_{bb}^{30} , Respectively.	70
60	SHARC Computations 9003.23, 9003.30, and 9003.121, Absolute Pressure at Points C_w^{30} , C_{pt}^{30} , and C_{bb}^{30} , Respectively.	71
61	SHARC Computations 9003.23, 9003.30, and 9003.121, Absolute Pressure at Points D_w^{30} , D_{pt}^{30} , and D_{bb}^{30} , Respectively.	72
62	SHARC Computations 9003.23, 9003.30, and 9003.121, Absolute Pressure at Points E_w^{30} , E_{pt}^{30} , and E_{bb}^{30} , Respectively.	73
63	SHARC Computations 9003.23, 9003.30, and 9003.121, Absolute Pressure at Points F_w^{30} , F_{pt}^{30} , and F_{bb}^{30} , Respectively.	74
64	SHARC Problem 9003.251, 60 Degree Smooth Wedge, Absolute Pressure Contours at 50 μ s.	77
65	SHARC Problem 9003.251, 60 Degree Smooth Wedge, Density Contours at 50 μ s.	78
66	SHARC 9003.121 and 9003.251, and HULL122 9001.181 Computations, Absolute Pressure at Points A_{bt}^{60} and A_w^{60}	79
67	SHARC 9003.121 and 9003.251, and HULL122 9001.181 Computations, Absolute Pressure at Points B_{bt}^{60} and B_w^{60}	81

List of Figures (Continued)

<u>Figure</u>		<u>Page</u>
68	SHARC 9003.121 and 9003.251, and HULL122 9001.181 Computations, Absolute Pressure at Points C_{bl}^{60} and C_w^{60}	82
69	SHARC 9003.121 and 9003.251, and HULL122 9001.181 Computations, Absolute Pressure at Points D_{bl}^{60} and D_w^{60}	83
70	SHARC 9003.121 and 9003.251, and HULL122 9001.181 Computations, Absolute Pressure at Points E_{bl}^{60} and E_w^{60}	84
71	SHARC 9003.121 and 9003.251, and HULL122 9001.181 Computations, Absolute Pressure at Points F_{bl}^{60} and F_w^{60}	85
72	SHARC Problem 9003.241, 45 Degree Smooth Wedge, Absolute Pressure Contours at 50 μ s.	87
73	SHARC Problem 9003.241, 45 Degree Smooth Wedge, Density Contours at 50 μ s.	88
74	HULL122 Problem 9001.031, 45 Degree Smooth Wedge (Left and Bottom), Absolute Pressure Contours at 50 μ s.	89
75	HULL122 Problem 9001.031, 45 Degree Smooth Wedge (Left and Bottom), Density Contours at 50 μ s.	90
76	SHARC 9003.241 and HULL122 9001.031 Computations, Absolute Pressure at Points A_w^{45} and A_{bb}^{45}	91
77	SHARC 9003.241 and HULL122 9001.031 Computations, Absolute Pressure at Points B_w^{45} and B_{bb}^{45}	92
78	SHARC 9003.241 and HULL122 9001.031 Computations, Absolute Pressure at Points C_w^{45} and C_{bb}^{45}	93
79	SHARC 9003.241 and HULL122 9001.031 Computations, Absolute Pressure at Points D_w^{45} and D_{bb}^{45}	94
80	SHARC 9003.241 and HULL122 9001.031 Computations, Absolute Pressure at Points E_w^{45} and E_{bb}^{45}	95
81	SHARC 9003.241 and HULL122 9001.031 Computations, Absolute Pressure at Points F_w^{45} and F_{bb}^{45}	96

INTENTIONALLY LEFT BLANK.

List of Tables

<u>Table</u>		<u>Page</u>
1	The EMI Shot 8891 Shock Wave Flow Conditions	5
2	EMI Points A - F , and BRL Points A_w^{30} - F_w^{30} for the 30 Degree Wedge Computation	6
3	Summary of Hydrocode Computations	20
4	BRL Points A_{bb}^{30} - F_{bb}^{30} for the Rotated Shock and Rectangular Block Bottom Boundary, 30 Degree "Wedge" Computation	44
5	BRL Points A_{pt}^{30} - F_{pt}^{30} for the Rotated Shock and Infinite Top Reflective Boundary, 30 Degree "Wedge" Computation	66
6	BRL Points A_{bl}^{60} - F_{bl}^{60} for the Rotated Shock and Rectangular Block Left Boundary, 60 Degree "Wedge" Computation	76
7	BRL Points A_w^{60} - F_w^{60} for the 60 Degree Wedge Computation	76
8	BRL Points A_w^{45} - F_w^{45} for the 45 Degree Wedge SHARC Computation 9003.241	87
9	BRL Points A_{bb}^{45} - F_{bb}^{45} for the Rotated Shock and Rectangular Block Bottom Boundary, 45 Degree "Wedge" Computation	88
10	Summary of Results for Points E for the 30 Degree Wedge	98
11	Summary of Results for Points E for the 45 Degree Wedge	99
12	Summary of Results for Points E for the 60 Degree Wedge	99

INTENTIONALLY LEFT BLANK.

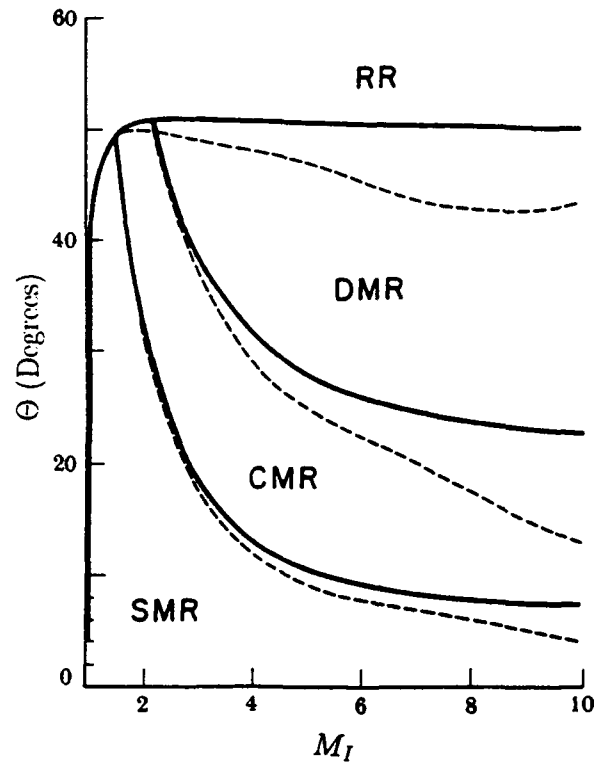


Figure 1. Regions of RR, SMR, CMR, and DMR and Their Transition Boundaries in the M_I , Θ Plane for Polytropic Air ($\gamma = 1.4$, Solid Lines) and Calorically Imperfect Air (Variable γ , Broken Lines).

I. Introduction

This report describes a computational study of the use of a limited set of locally available hydrodynamic computer codes, hereinafter referred to as "hydrocodes," in the study of the oblique interaction of a planar shock with a non-responding planar surface simulating a wedge. The primary purpose of this study was to explore the differences, if any, in the results of the computations by using various geometric configurations that are commonly used to simulate this interaction process, and the fluid dynamic implications of each. Systematic variations of various options within the hydrocodes were also exercised to isolate the effects of each on the subsequent solution. Among those options varied were the differencing method and its order, the use of artificial viscosity to control numerical oscillations, and the use of half hydrodynamic and half rigid flow field cells to model smooth ramps in a rectangular computational grid. The simulated shock and wedge interaction angle was also varied.

An excellent summary of the theoretical and experimental aspects of oblique shock reflection may be found in Glaz, *et al.*¹ It is also an excellent source of references for further reading. Figure 1, reproduced along with an edited caption with minor nomenclature modifications from Glaz, *et al.*,¹ shows the various regions of Regular Reflection (RR), which

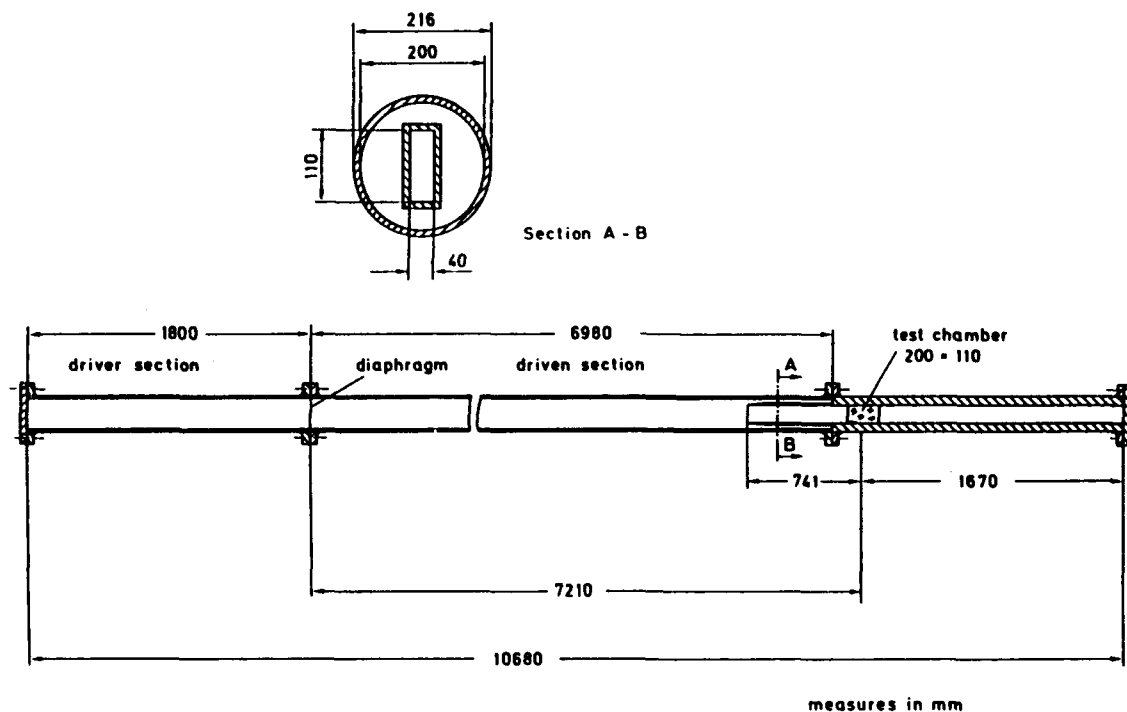


Figure 2. The EMI Shock Tube. (Courtesy of W. Heilig, EMI.)

includes simple oblique reflection and normal reflection, Single Mach Reflection (SMR), Complex Mach Reflection (CMR), and Double Mach Reflection (DMR), as related to the incident shock Mach number M_I and the wedge angle Θ .

II. The Experiment at the Ernst Mach Institute

The computational studies performed at the US Army Ballistic Research Laboratory (BRL) are based on a series of experiments performed² at the Ernst Mach Institute (EMI), Freiburg, Federal Republic of Germany. The experimental shot of particular interest here is Shot Number 8891 in a constant area, rectangular 40 mm deep by 110 mm high, test section of the EMI shock tube shown in Figure 2, which produced a non-decaying incident shock wave with a Mach number $M_I = 2.12$. During the course of performing their computations with the STEALTH³ code, some discrepancies in the computational results for the interaction of this shock with a wedge having an angle $\Theta = 60$ degrees with the horizontal were noted by the EMI personnel. A schematic showing a typical single Mach reflection of an incident shock on a wedge of angle Θ is shown in Figure 3. The incident shock is labeled with an "I," and in this study is taken to be a non-decaying shock wave moving from left to right into the undisturbed region 1. Region 1 in this case represents the air in the driven (or "expansion") section of the shock tube. The reported⁴ thermodynamic and flow parameters in region 1 are an absolute static pressure $p_1 = 0.09$ bar (9.0 kPa, or 1.3053 psi), a static temperature

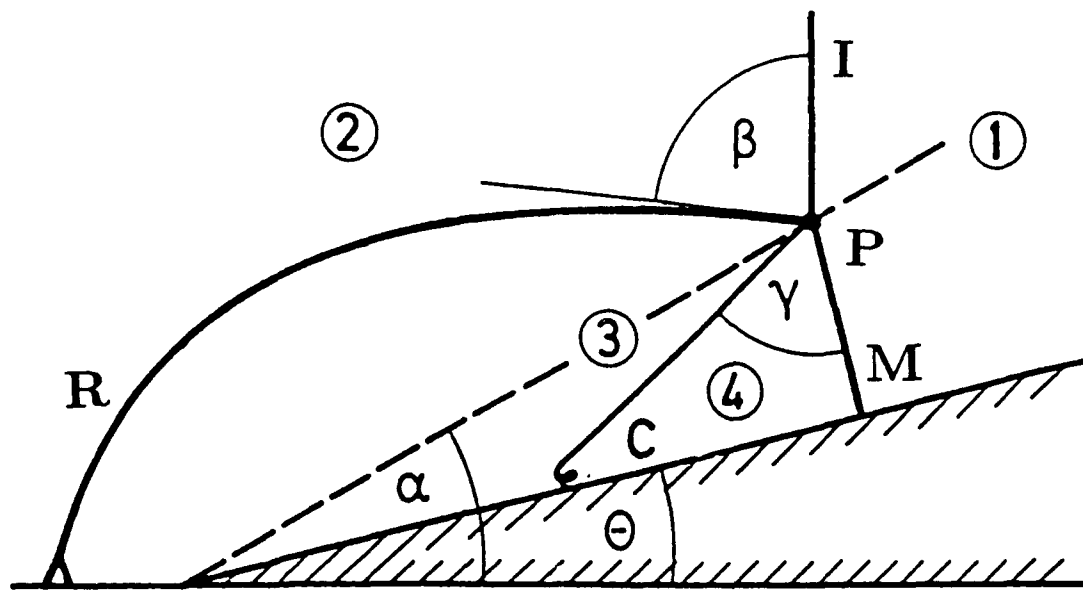


Figure 3. Single Mach Reflection. (Courtesy of W. Heilig, EMI.)

$T_1 = 294.65 \text{ K}$ (21.5 C), a particle velocity $u_1 = 0$ in laboratory reference coordinates, and a static density $\rho_1 = 0.106 \text{ kg/m}^3$. The reported⁴ parameters behind incident shock I are an absolute static pressure $p_2 = 0.457 \text{ bar}$ (45.7 kPa , or 6.6282 psi), and hence a static overpressure $p_{2-1} = 0.367 \text{ bar}$ (36.7 kPa , or 5.3229 psi), a static density $\rho_2 = 0.302 \text{ kg/m}^3$, and a particle velocity $u_2 = 472.46 \text{ m/s}$. Hereinafter, any reference to “pressure” may be construed as meaning “absolute pressure” unless specifically stated otherwise.

The driver stagnation pressure was reported⁴ as $P_{04} = 7.358 \text{ bar}$ (735.8 kPa , or 106.7 psi), which in the absence of a definitive statement was assumed to be an absolute value, and no driver temperature was reported. This caused some initial confusion when trying to make a full determination of the thermodynamic and flow parameters in the system. To illustrate this, a simplifying assumption is made that the shock tube operated with no losses, so that all interactions between the four definable states in the flow in a straight shock tube were the result of the application of the relations governing the ideal thermodynamics and gas dynamics of a Riemann problem.⁵ The initial assumption was that the driver gas was air, as reported, in thermal equilibrium with the laboratory temperature, so the absolute driver gas stagnation temperature $T_{04} = T_1 = 294.65 \text{ K}$. If that were the case, then the required driver absolute pressure to produce this $M_I = 2.12$ shock would have been $P_{04} = 4.331 \text{ bar}$ (62.8158 psi), instead of the reported $P_{04} = 7.358 \text{ bar}$.

One direct reason for requiring a larger stagnation pressure in the driver than that called for by the theoretical computations is the losses that occur in the shock tube. A study of the EMI shock tube shown in Figure 2 shows that considerable losses can occur. The initial shock wave must travel along a relatively long 200 mm diameter expansion section prior to being “cut out” by the 40 mm deep by 110 mm high test section. The section of the incident shock that actually enters the rectangular cross section test section is the incident shock that

the experimental model experiences. This is a logical way to use the shock tube: a clean laboratory shock is achieved in exchange for the penalty incurred by requiring a higher than theoretical driver stagnation pressure. It assures that a sharp, well formed shock is formed for precise theoretical studies, while having the additional benefit of cutting off the boundary layer that had developed in the long travel of the shock down the circular expansion section.

III. The Hydrocode Computations at the Ernst Mach Institute

The results from the EMI STEALTH computations, plus some experimental data, were communicated to the BRL in both written form⁴ and during technical discussions.⁶ Computations were performed by EMI for wedge angles (see Figure 3) of $\Theta = 10, 20, 30, 45, 60,$ and 70 degrees. Experimental measurements that were taken for the $M_I = 2.12$ and $\Theta = 30$ degrees experiment were reported⁶ in some detail, as was the STEALTH computation for that angle. As may be seen through careful measuring in Figure 1, this combination of shock Mach number and wedge angle is very close to the border between CMR and SMR, but in the CMR region.

1. The EMI 30 Degree Wedge Computation

The complete set of experimental conditions, including those parameters derived theoretically from the directly measured values in EMI shot number 8891, are summarized in Table 1 and are expressed in the *cgs* units system employed by HULL⁷ and SHARC.⁸

The computational grid used by EMI^{2,4} for the STEALTH³ hydrocode computations is shown in Figure 4. This grid, as were the others done by EMI, was designed to simulate the physical space in the EMI shock tube. The EMI shock tube test section has a rectangular cross section, which for this particular experiment with the wedge and mounting plate in position has an actual height of 10.0 cm and a depth of 4.0 cm. The wedge for the EMI experiments was designed to span the entire 4.0 cm depth of the shock tube to make the problem two-dimensional (2-D). For this problem, the computational space was assumed to be of unit depth. The grid had 26 vertex lines in the vertical (y) direction, the measure of height of the wedge projected onto the vertical axis. This produced 25 cells in that direction which were evenly spaced with a grid size of $\Delta y = 0.40$ cm at the left boundary of the grid. The grid had 99 vertex lines in the horizontal (x) direction, the measure of length of the wedge projected onto the horizontal axis. This produced 98 cells that were evenly spaced across the entire grid with a grid size of $\Delta x = 0.25$ cm. The relative coarseness of this grid was undoubtedly a matter of necessity, because the computer available to EMI was a VAX 11/750 running under the VMS operating system, certainly a competent machine, but overmatched by a large scale continuum mechanics code. The positions of the EMI points A

Table 1. The EMI Shot 8891 Shock Wave Flow Conditions

Parameter (Units)	Region 1 (Ambient)	Region 2 (Shocked)
γ (-)	1.4	1.4
R (ergs/g/K)	2.87054×10^6	2.87054×10^6
p (dynes/cm ²)	8.99973×10^4	4.56998×10^5
P_0 (dynes/cm ²)	8.99973×10^4	8.93543×10^5
ρ (g/cm ³)	1.06405×10^{-4}	3.02251×10^{-4}
ρ_0 (g/cm ³)	1.06405×10^{-4}	4.87942×10^{-4}
T (K)	2.94650×10^2	5.26730×10^2
T_0 (K)	2.94650×10^2	6.37952×10^2
I (ergs/g)	2.11450×10^9	3.77998×10^9
u (cm/s)	0.	4.72742×10^4
c (cm/s)	3.44109×10^4	4.60084×10^4
c_0 (cm/s)	3.44109×10^4	5.06334×10^4
M (-)	0.	1.02751
$M_I = 2.12022$		
$p_{2-1} = 3.67001 \times 10^5 \text{ dynes/cm}^2$		

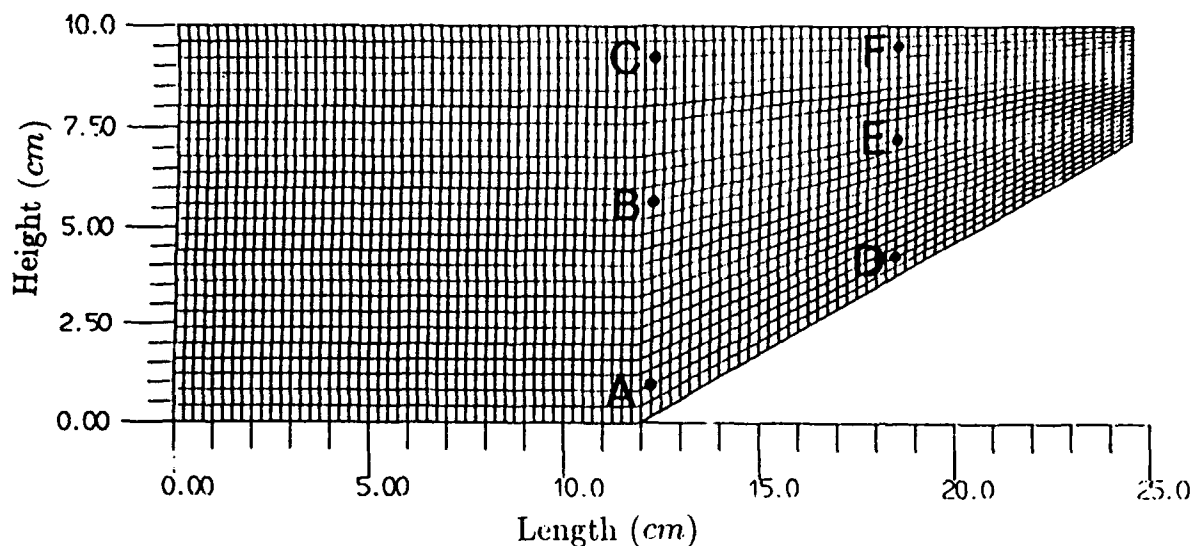


Figure 4. EMI 30 Degree Wedge Computational Grid. (Courtesy of W. Heilig, EMI.)

through F shown in Figure 4, redefined as points A_w^{30} through F_w^{30} to match the coordinates shown in Figure 4 and to the same accuracy as reported, are shown in Table 2. The final

Table 2. EMI Points $A - F$, and BRL Points $A_w^{30} - F_w^{30}$ for the 30 Degree Wedge Computation

Position	EMI/STEALTH		Position	BRL (Redefined)	
	x-Position (cm)	y-Position (cm)		x-Position (cm)	y-Position (cm)
A	12.250	0.9328	A_w^{30}	0.250	0.9328
B	12.250	5.6635	B_w^{30}	0.250	5.6635
C	12.250	9.21155	C_w^{30}	0.250	9.21155
D	18.500	4.2526	D_w^{30}	6.501	4.2526
E	18.500	7.2512	E_w^{30}	6.501	7.2512
F	18.500	9.50023	F_w^{30}	6.501	9.50023

two columns in Table 2 show the same point in a coordinate system used by the BRL which references all critical space and time parameters to zero at the leading edge of the wedge. The slight positive offset of 0.001 cm in x for points D_w^{30} through F_w^{30} was introduced to keep the hydrocode data station points from being ambiguously placed on computational cell boundaries. The notation for point A_w^{30} , for example, has a subscript "w" to indicate that the geometry is for an orthogonal shock striking a wedge on a reflecting plane, and a superscript "30" to indicate the simulated wedge angle in degrees. In the discussions that

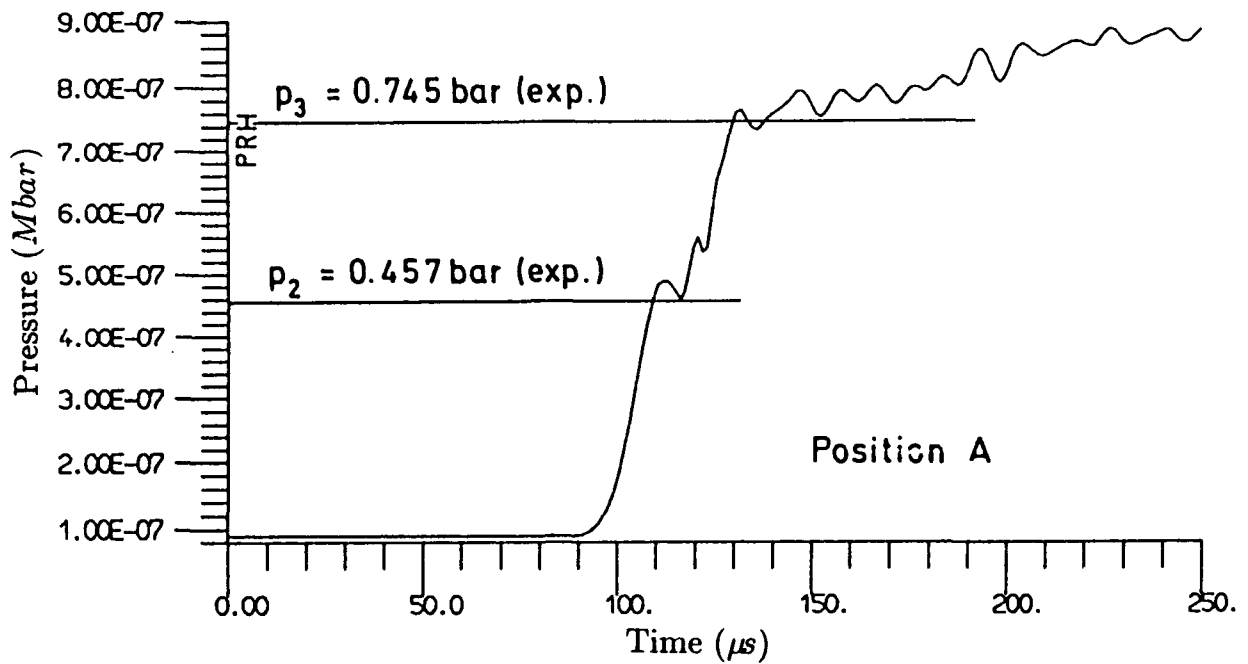


Figure 5. Absolute Static Pressures at Point A, EMI 30 Degree Wedge Computation. (Courtesy of W. Heilig, EMI.)

follow later, the subscript “*bb*” will indicate “block bottom,” “*bl*” will indicate “block left,” “*pt*” will indicate “planar top,” and the absence of a subscript will be a general reference toward the set of points of that letter designation and simulated wedge angle.

Figure 5 shows the computed absolute static pressure versus time at point A. The time $t = 0.0$ in the EMI STEALTH computation is apparently defined at the start of the computation, with the incident shock I at its initial (unspecified) position upstream from the leading edge of the wedge. The experimentally measured incident shock pressure of 0.457 bar (6.63 psi) is noted on the plot, as is the reflected shock pressure of 0.745 bar (10.81 psi). The relatively coarse mesh used in the computation causes the shock wave to be spread out among several flow field cells. The shock arrival time $t = 103.5 \mu\text{s}$ is defined for purposes of this report as occurring at one half of the pressure rise from the ambient expansion section pressure of 0.09 bar (1.31 psi) to the incident shock pressure. (It was measured on a larger scale plot for this report with a Gerber scale. The estimated reading error is $\pm 0.5 \mu\text{s}$.) The STEALTH computation gives a good indication of this incident shock strength, but the computational reflected wave arrives quickly enough that the actual value of the computational prediction of the incident shock strength at this point is uncertain. The computation also shows good initial agreement with the experimentally measured reflected shock pressure. Position A never experiences the passage of a Mach stem because of the combination of its proximity to the leading edge of the wedge and its height above it. The arrival of this reflected shock occurs at $t = 125.5 \mu\text{s}$, for a time difference

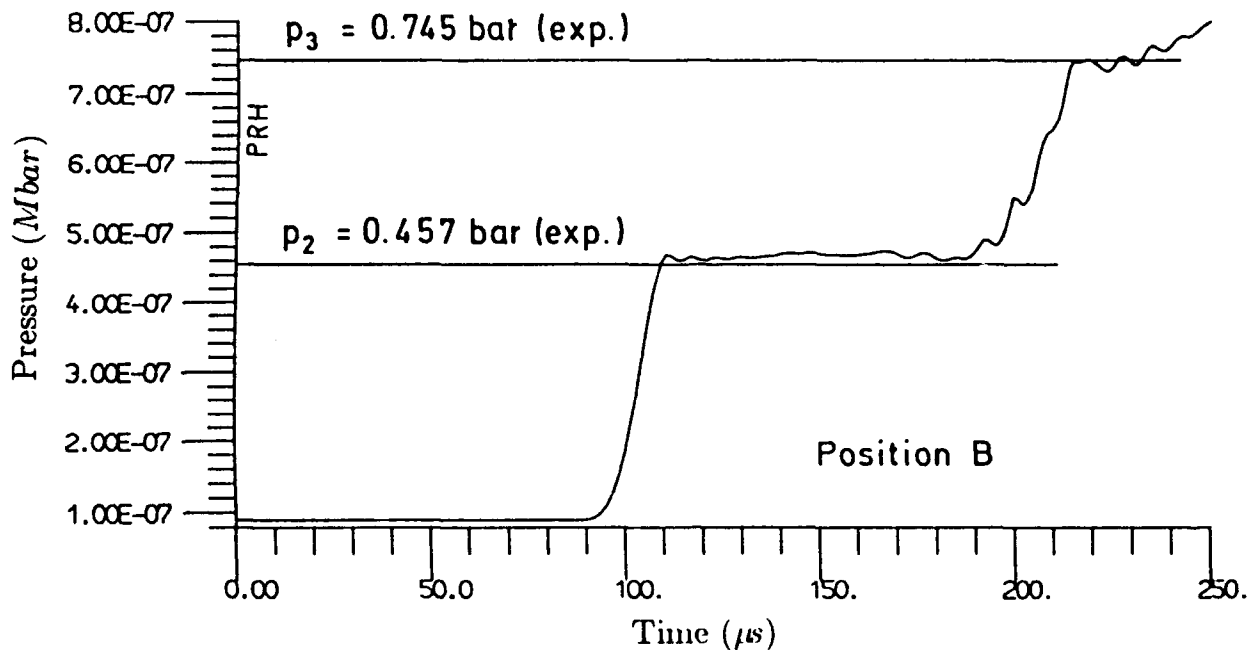


Figure 6. Absolute Static Pressures at Point *B*, EMI 30 Degree Wedge Computation. (Courtesy of W. Heilig, EMI.)

between the two shocks of $22.0 \mu\text{s}$. The upward drift of the pressure after the passage of the reflected shock is due to a combined effect of the upstream disturbance of the flow by the expanding reflected shock, and the confining effects of the finite height of the test section.

Figure 6 shows the computed static pressure versus time at point *B*. The experimentally measured incident shock pressure of 0.457 bar and the reflected shock pressure of 0.745 bar are noted on the plot. The STEALTH computation predicted an incident shock pressure level of approximately 0.467 bar , and a reflected shock pressure of 0.745 bar . The incident shock arrival time, measured as for point *A*, is $t = 102.8 \mu\text{s}$, and the reflected shock arrival time is $t = 204.5 \mu\text{s}$, for a time difference of $101.7 \mu\text{s}$. Point *B* never experiences the passage of a Mach stem because of its position in space above the wedge. There is some uncertainty as to whether its position was reported correctly. This will be discussed later.

Figure 7 shows the computed static pressure versus time at point *C*. This point only experiences the passage of the incident shock during the time presented. The experimentally measured incident shock pressure of 0.457 bar is noted on the plot, with the computed value of 0.463 bar , at an arrival time of $102.3 \mu\text{s}$.

Figure 8 shows the computed static pressure at point *D*. This point should not experience the passage of the incident shock, because at this position along the wedge surface, a Mach stem large enough to pass over point *D* should form. It appears that the STEALTH computation, even with the relatively low resolution in the grid, has predicted the passage

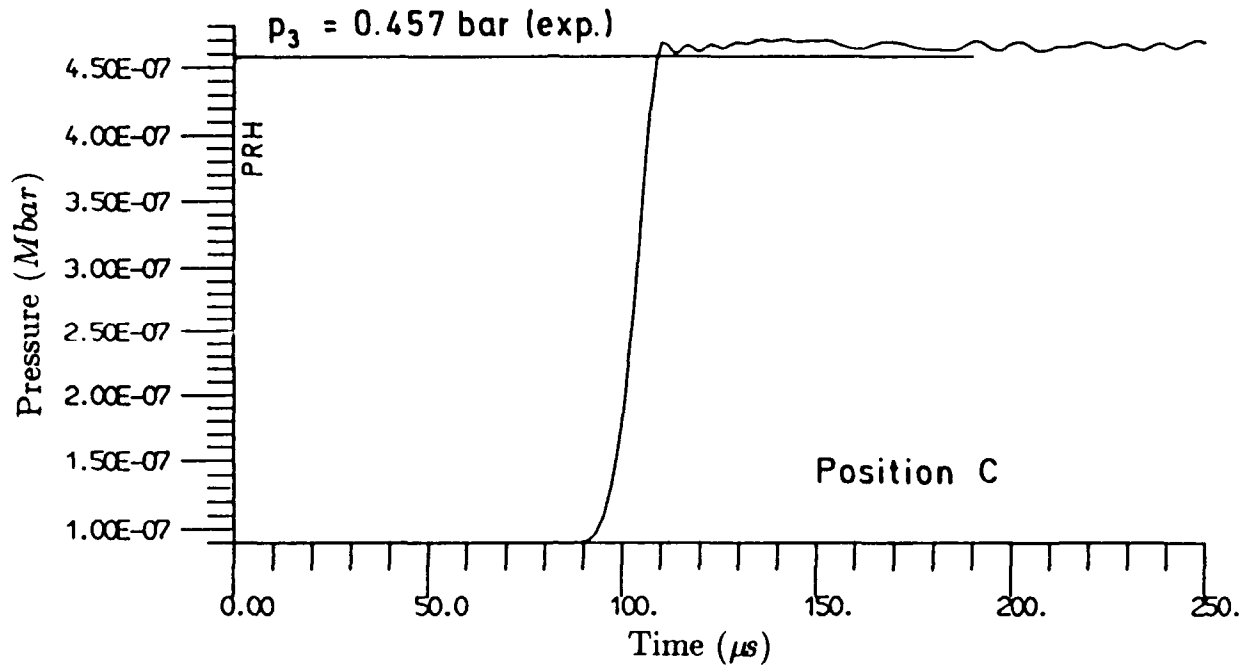


Figure 7. Absolute Static Pressures at Point *C*, EMI 30 Degree Wedge Computation. (Courtesy of W. Heilig, EMI.)

of a somewhat smeared out Mach stem. As may be seen in Figure 3, the reflected shock “R” is straight near the triple point “P,” so in the immediate vicinity of point P and the Mach stem “M” the pressure equilibrium condition shown in Equation 1

$$p_3 = p_4, \quad (1)$$

applies, with p_4 being the theoretical pressure behind the Mach stem M. However, the reflected shock R in Figure 3 is shown as a curved shock, because there is an expansion wave (not shown in Figure 3) that emanates from the corner at the leading edge of the wedge. The leading edge of this expansion wave follows the triple point system at a distance that increases in a self-similar manner for this combination of shock Mach number and wedge angle. The expansion wave weakens the section of the reflected shock where it comes into contact with it, causing the downward curvature of the reflected shock. This process also reduces the pressure in all regions through which the expansion wave travels by an amount consistent with the local strength of the expansion wave. Thus, while Equation 1 still is correct, the actual values of p_3 , and hence p_4 , are varying in that region affected by the expansion wave. Figure 8 shows a disturbance in the computed pressure at $t = 187.0 \mu\text{s}$ at a pressure of 0.592 bar, probably due to a smeared precursor to the Mach stem, followed by a pressure level very close to the experimental value of 0.745 bar behind the actual Mach stem. The approximate arrival time of this computational Mach stem is $t = 184.0 \mu\text{s}$.

Figure 9 shows the computed static pressure at point *E*. Because of its height above

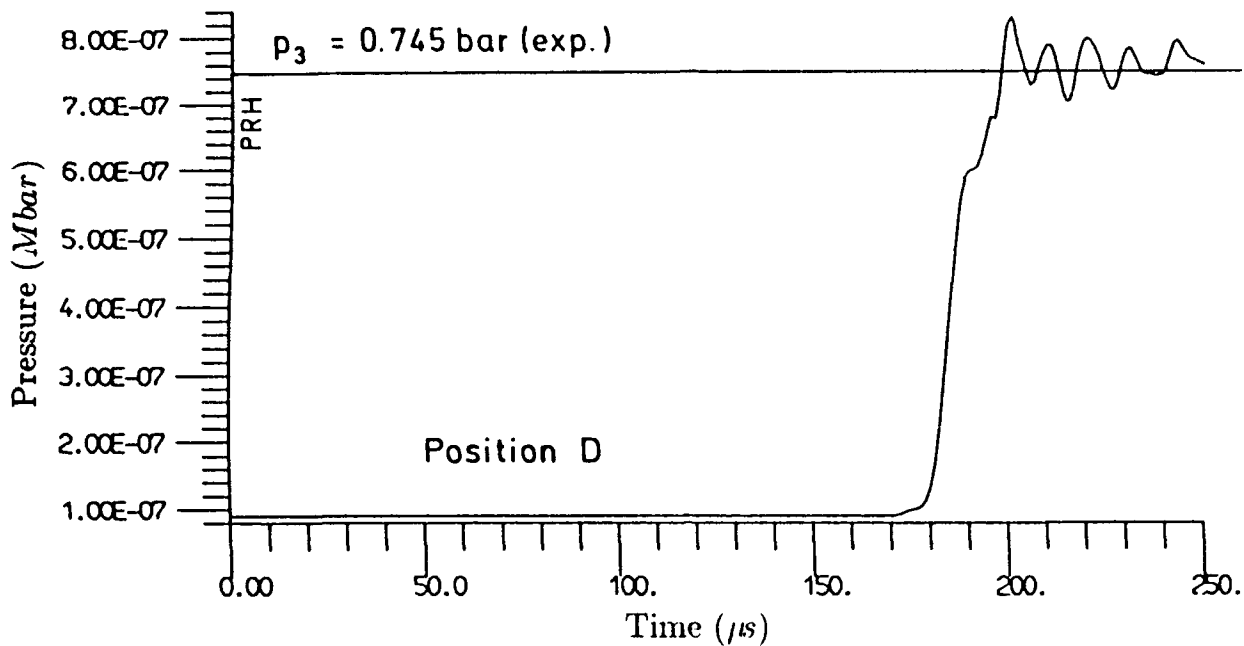


Figure 8. Absolute Static Pressures at Point *D*, EMI 30 Degree Wedge Computation. (Courtesy of W. Heilig, EMI.)

the wedge surface, point *E* first experiences the passage of the incident shock *I*, followed by the reflected shock *R*. As before, the computed pressure of 0.467 bar for the incident shock agrees well with the experimentally measured value of 0.457 bar. The computed arrival time is approximately 189 μs . The computed pressure of the reflected wave at point *E* is difficult to estimate from Figure 9 because the computation was ended very soon after its arrival there. It is estimated from Figure 9 that the reflected wave pressure is approximately 0.728 bar, slightly below the experimental value of 0.745 bar, with an arrival time of 221.0 μs .

Figure 10 shows the computed static pressure at point *F*. As with point *C*, point *F* is high enough above the wedge surface that it only experiences the passage of the incident shock. The computed pressure of 0.468 bar, arriving at 189 μs , is only slightly above the experimentally measured pressure of 0.457 bar. The STEALTH computation simulating this interaction produced good estimates of the various pressure plateaus in spite of the relatively low resolution computational grid, although the shock rise times were extremely long, as would be expected with such a grid.

2. The EMI 60 Degree Wedge Computation

The EMI STEALTH computation for the same incident shock Mach number, $M_I = 2.12$, interacting with a wedge with an angle $\Theta = 60$ degrees showed an anomaly that provided

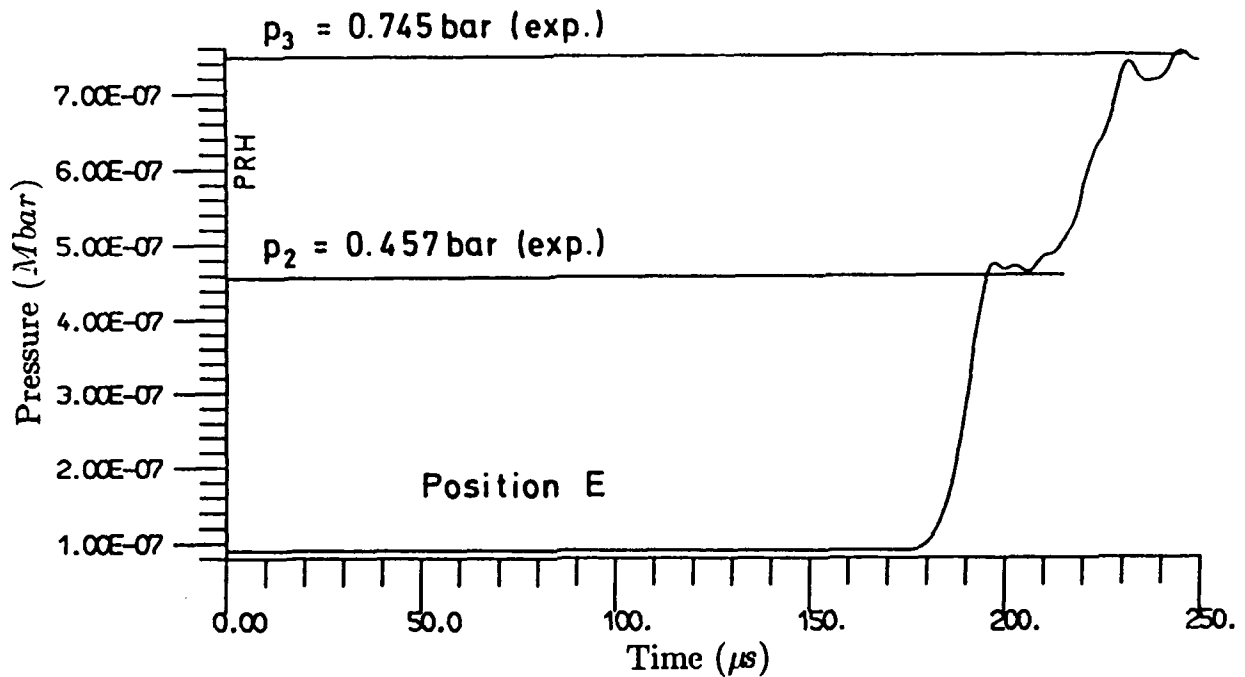


Figure 9. Absolute Static Pressures at Point *E*, EMI 30 Degree Wedge Computation. (Courtesy of W. Heilig, EMI.)

the impetus for the consultation with the BRL. According to EMI, the computation had proceeded in what appeared to be a normal manner. However, post processing showed a high gradient region that had the appearance of a computational attached shock at the leading edge of the wedge in both pressure and density contour plots just after the arrival and subsequent reflection of the incident shock. This is shown in Figure 11. There is no physical basis for the existence of any type of shock in this configuration at this time in the interaction, so EMI presumed that there was either a defect in the STEALTH code, or that the code was possibly not appropriate for this problem. At that time, EMI was in the process of obtaining the SHARC⁸ hydrocode from S-Cubed. Because the BRL had been using the code for several years, it was agreed that the BRL would run some matching computations with its identical version of the SHARC code, the HULL⁷ hydrocode, and the BLAST2D⁹ code.

IV. The Hydrocode Computations at the BRL

All computations were run with the planar, steady $M_I = 2.12$ incident shock, the steady flow conditions behind it, and the ambient conditions ahead of it as reported to the BRL by EMI and summarized in Table 1. Many SHARC and HULL computations were run as this study developed, partially because interesting aspects of the different ways

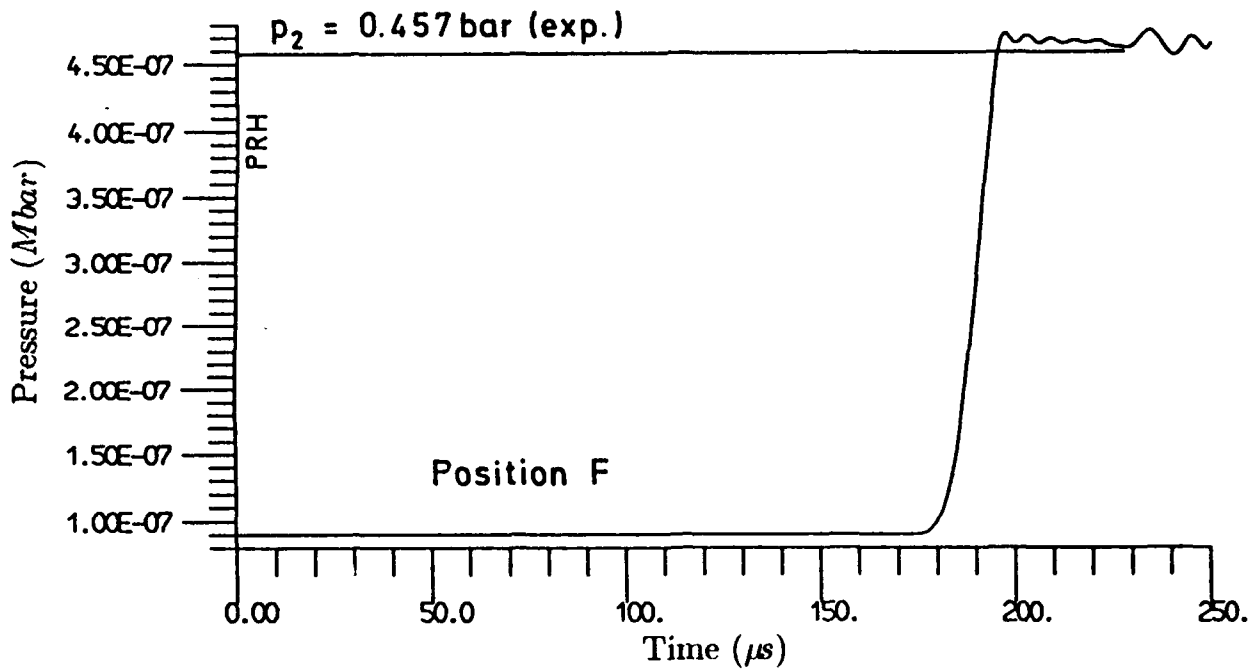


Figure 10. Absolute Static Pressures at Point *F*, EMI 30 Degree Wedge Computation. (Courtesy of W. Heilig, EMI.)

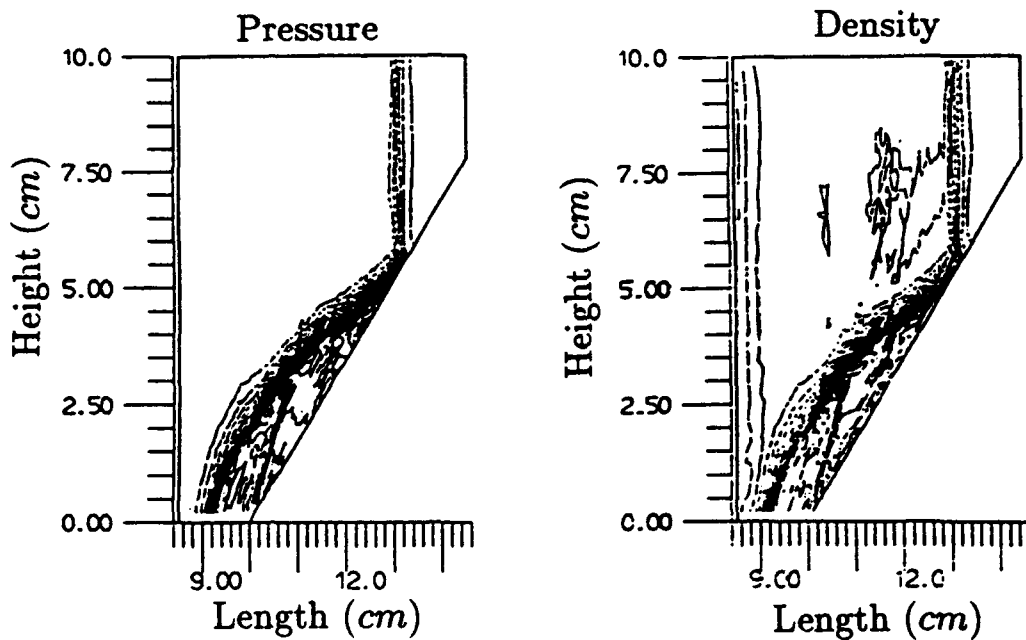


Figure 11. EMI 60 Degree Wedge Computation. (Courtesy of W. Heilig, EMI.)

of modeling the interaction became evident. As inevitably occurs, minor code errors in SHARC were discovered (it was run the most) and corrected, and problems were rerun. The most fundamental difference between the SHARC and HULL codes and the STEALTH code is that SHARC and HULL are ultimately Eulerian codes (with a second order Lagrangian first phase in the differencing for flow field cells of equal size), whereas STEALTH is a Lagrangian code. Only one of the BLAST2D code computations by Ms. Hisley¹⁰ is shown here for comparison. The BLAST2D results will be discussed in a separate report¹¹ by Ms. Hisley.

The SHARC code was used in several configurations of operational parameters and physical space simulations, all in 2-D Cartesian coordinates. The SHARC code can simulate a wedge mounted on a reflecting plane in two ways. The wedge can be made up only of rigid "island" cells whose aspect ratio, defined in Equation 2,

$$A_r = \frac{\Delta y}{\Delta x}, \quad (2)$$

is chosen such that it is equal to the tangent of the wedge angle, as shown in Equation 3,

$$\tan\Theta = A_r, \quad (3)$$

so that the wedge surface is a series of small steps one cell high and one cell long in its most simple stepped form. A simplified schematic view of this type of configuration is shown in Figure 12. The island cells are denoted by an "I" placed in the cell, and a subset of the purely hydrodynamic cells along the stepped wedge surface by an "H." The unmarked cells are also purely hydrodynamic cells. This approach has some difficulties. The most severe problem is that the wedge surface is not smooth, but rather consists of a series of small normal reflection surfaces. This may not be of great importance if the interest is in the flow field away from the wedge surface. However, many applications do require accurately simulated wedge surfaces, such as the study of the process of transition to Mach reflection which is of interest here. Another problem is that the SHARC code begins to experience stability problems when there are high gradients in flow field cells with $A_r > 3.0$, and computational accuracy degrades when $A_r \neq 1.0$. This can be circumvented by making the individual steps comprising a simulated wedge surface out of whatever number of cells high or long are necessary to approximate the angle. To a reasonable limit, the error in simulating the surface drops with decreasing cell size, but then computational costs rise geometrically. Because of their common origin (SHARC is a now significantly modified offshoot of HULL), the HULL hydrocode can simulate a wedge in very much the same manner, with positive and negative aspects similar to those for SHARC.

An alternative to simulating the entire 2-D wedge in SHARC with only island cells is to simulate the subsurface with island cells and the surface with "shore" cells. Shore¹² cells are half island and half hydrodynamic, divided along either cell diagonal, so there are four possible types of shore cells. A simplified schematic view of this type of configuration is shown in Figure 13. The island cells are denoted by an "I" placed in the cell, the shore cells by an "S," and a subset of the purely hydrodynamic cells along the wedge surface by an "H."

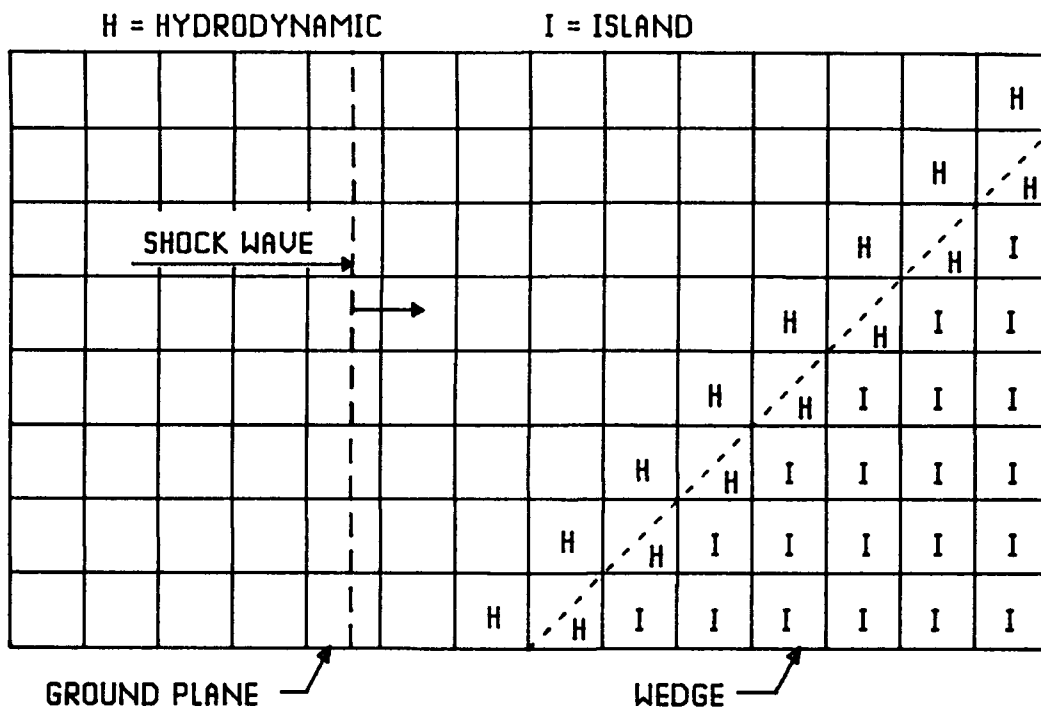


Figure 12. Shock Interaction with a Wedge Approximated by a Rigid Stair Step Surface, Mounted on a Reflecting Ground Plane.

The rigid half of each shore cell in Figure 13 lies below and to the right of the dotted line coinciding with the diagonals of each shore cell and indicating the simulated wedge surface, and the hydrodynamic half lies above and to the left of the dotted line. These shore cells were incorporated into S-Cubed's HULL code version (a predecessor to SHARC) several years ago after a transfer from the BRL of the BRL's version of the HULL airblast code. While the shore cells do make a more smooth wedge surface, they are limited by the same considerations of cell aspect ratio, while also posing their own additional stability problems and limitations on the explicitly computed time step. The HULL hydrocode does not have a similar option for fractional hydrodynamic and island cells. The BRL offered the coding changes to Orlando Technology, Inc., (OTI) but the offer was declined because the use of such cells did not conform to the coding philosophy and plans of OTI, certainly a defensible position to take.

Both methods described above are valid ways to model a wedge resting on a perfectly reflecting ground plane in a laboratory configuration with a shock wave approaching it and having its velocity vector parallel to the ground plane. It is worth noting here that three critically important hydrodynamic phenomena are also correctly modeled in a theoretical sense with this configuration. The first is that the leading edge of the wedge, a clearly defined starting point for the shock reflection process, is established. The second is that the expansion wave that originates from the leading edge of the wedge is also modeled. The third is that a clearly defined reflecting plane upstream from the wedge is modeled, which then requires the reflected shock that travels upstream from the wedge to have the correct boundary condition with the reflected shock front perpendicular to the ground plane and hence no velocity vector normal to the surface at the ground plane. These conditions are met for any wedge angle using this configuration.

This is not necessarily the best way to simulate the interaction of a blast wave from an above ground nuclear burst with the ground. That configuration does not start with a corner at a leading edge and its associated expansion wave. Thermal and debris effects aside, an above ground nuclear burst interaction starts with a normal shock reflection at ground zero, directly below the burst point, and then moves out radially in an oblique shock reflection process that at some point will develop into a Mach reflection. Thus, the driving flow behind the interaction point can be very different from that for a laboratory shock interacting with a wedge on a reflecting plane.

A third way to model the interaction of a shock and a wedge with either SHARC or HULL is to generate a rectangular block out of island cells, and position it out in the simulated flow field. The oncoming shock and its blast flow field behind it are then rotated in the computational grid so that it approaches a corner of the block at the desired angle relative to one of the sides of the block. This also allows a coincident computation on the second side at an interaction angle equal to the complement of the interaction angle of the first side. A simplified schematic view of this type of configuration is shown in Figure 14. The island cells are denoted by an "I" placed in the cell, and a subset of the purely hydrodynamic cells by an "H." This configuration produces a shock interaction pattern that is superficially similar to that for a wedge on a ground plane, but is distinct in a critically important way. The reflected shock no longer has the specific boundary condition imposed on it by the reflecting

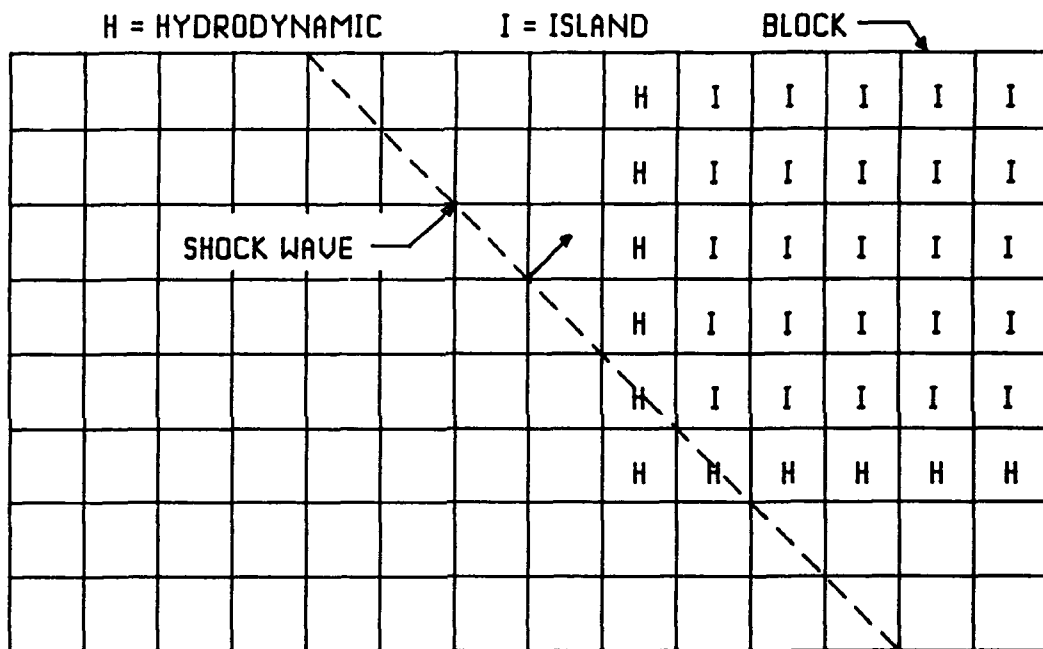


Figure 14. Shock Interaction with a Rectangular Block in the Flow Field, Rotated Shock and Orthogonally Positioned Block.

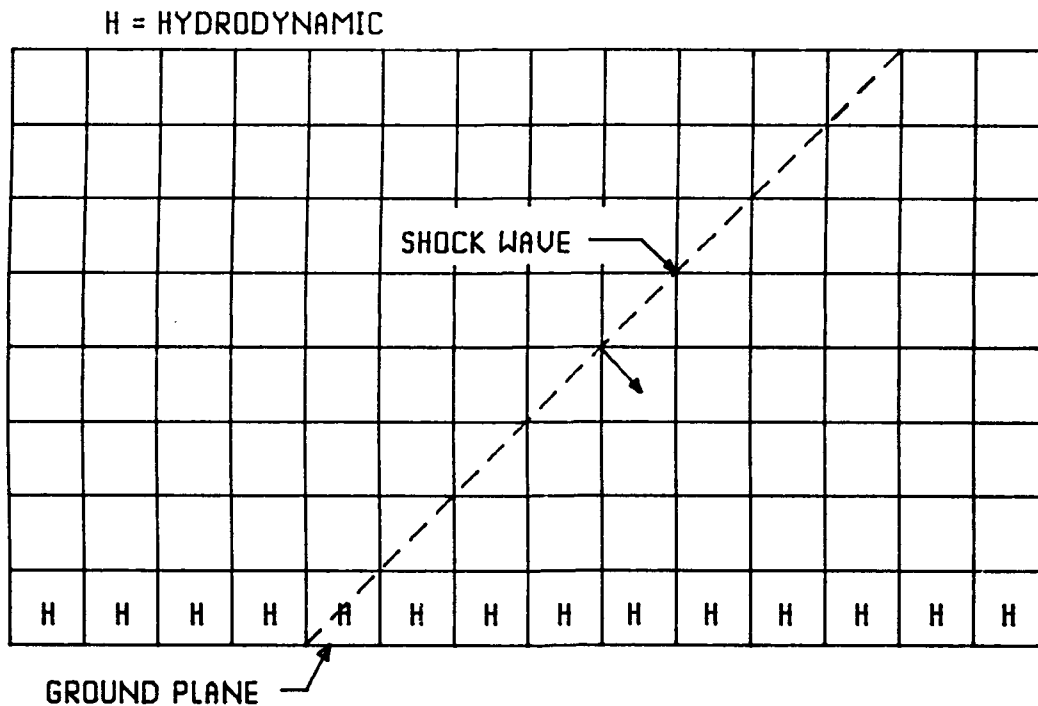


Figure 15. Interaction of a Rotated Shock with an Infinite Reflecting Plane on the Boundary of the Flow Field.

ground plane upstream from the leading edge of the wedge in the configuration discussed above, so the reflected shock curvature as a function of distance is not necessarily the same. Also, because (a) the curved reflected shock moves upstream away from the leading edge, (b) the flow behind it is typically subsonic, and (c) the rate of change of the curvature is not necessarily constant, the flow conditions behind it are variable and flow communication around the corner can occur. This configuration does not accurately represent either a laboratory wedge or a nuclear height of burst configuration.

Finally, a fourth way to computationally simulate a shock interaction with a wedge with these codes is to strike an infinitely long orthogonally positioned reflecting plane with a rotated shock. A simplified schematic view of this type of configuration is shown in Figure 15. The subset of purely hydrodynamic cells immediately adjacent to the reflecting plane are denoted by an "H." This configuration does not correctly model the laboratory configuration of a wedge on a reflecting ground plane because it lacks not only a leading edge with its associated initiation of the interaction but also its following expansion wave. It approximates the interaction of a nuclear burst with a ground plane away from ground zero, but without the transition history from normal to oblique reflection driving it.

Comparisons will be made for all of the above configurations, primarily with the SHARC code. The SHARC code was also used in a variety of parametric configurations of fluxing

method and artificial viscosity usage. These are discussed below, as are a set of companion HULL runs. The final set of BRL SHARC and HULL computations is briefly summarized in Table 3. Because of the great profusion of computations, especially those which were rerun after errors in the SHARC code were discovered, the simplified problem identification systems normally used for reports became cumbersome. Thus, the basic problem numbers that are normally used at run time are retained for use in the report. The first two digits correspond to the year, the second two to the month, the first two after the decimal point to the day of the month, and any added digits to a permutation on the same date.

1. The 30 Degree Wedge

a. The Basic Grid for the 30 Degree Wedge on a Reflecting Plane

The first set of computations is for a wedge with an angle $\Theta = 30$ degrees. The physical space in the computational grids used by the BRL for the SHARC⁸ and HULL⁷ hydrocode computations for the 30 degree wedge on a reflecting plane were designed to be as close as possible to that for the EMI STEALTH computation, although the grid resolution itself was higher in the SHARC and HULL computations. It is important to note that the area of interest in the experiment and the computations is immediately on and above the angled wedge surface. It is not necessary to model the shock tube test section precisely, as long as none of the physics of the shock movement and the interaction at the wedge surface are altered. The dominant direction of the motion of the shock and gas flow, except for the interactions on the wedge, is in the x direction. Therefore, to minimize effects caused by differences in the flow field cell sizes that must inevitably occur, the flow field cell size in the x direction, Δx , will be kept the same at $\Delta x = 0.10$ cm in the grid designs for all three values of Θ : 30 degrees, 45 degrees, and 60 degrees. The flow field cell size in the y direction, Δy , will be varied to fit the needed vertical space and the required wedge angle. The EMI shock tube had a height $y_t = 10.0$ cm, which will be approximated but not modeled exactly, as it is not necessary to do so. The length of the actual wedge surface used by EMI appears to be approximately $L_w^{30} = 15.0$ cm. With this approximation, the wedge length in the x direction is $x_w^{30} = L_w^{30} \cos 30 = 12.99$ cm. Because of the decision to use a fixed $\Delta x = 0.10$ cm, the rounded value $x_w^{30} = 13.00$ cm was chosen, so that the wedge is represented by $J_w^{30} = 130$ cells in the x direction. From $\tan \Theta = \Delta y / \Delta x$, the cell size in the y direction is chosen as $\Delta y = 0.0577350$ cm, and correspondingly $J_w^{30} = 130$ cells are used to represent the wedge in the y direction, producing a wedge height $y_w^{30} = 7.505550$ cm. The closest approximation to the overall EMI shock tube height $y_t = 10.0$ cm using this fixed Δy is produced by having a total number of y direction active flow field cells $J_t^{30} = 173$. This produces a simulated active flow field shock tube height $y_t^{30} = 9.988155$ cm to the top reflective boundary. The floor of the shock tube, and hence the bottom reflective boundary in the computation is defined as $y = 0.0$.

Because the areas of interest are directly on or above the wedge surface, and the flow behind the incident shock is slightly supersonic, there is no need to simulate much of the

Table 3. Summary of Hydrocode Computations

PROBLEM NUMBER	CODE	WEDGE ANGLE DEGREES	GEOMETRIC CONFIGURATION WEDGE/SHOCK	FLUXING METHOD	ARTIFICIAL VISCOSITY FLAG
8912.071	HULL122	30	STEP/ ORTHOGONAL	2	0
9001.031	HULL122	45	BLOCK/ ROTATED	2	0
9001.181	HULL122	30 & 60	BLOCK/ ROTATED	2	0
9002.12	SHARC	30	STEP/ ORTHOGONAL	4	0
9003.121	SHARC	30 & 60	BLOCK/ ROTATED	4	0
9003.23	SHARC	30	SHORE/ ORTHOGONAL	4	0
9003.241	SHARC	45	SHORE/ ORTHOGONAL	4	0
9003.251	SHARC	60	SHORE/ ORTHOGONAL	4	0
9003.26	SHARC	30	SHORE/ ORTHOGONAL	2	0
9003.27	SHARC	30	SHORE/ ORTHOGONAL	4	1
9003.28	SHARC	30	SHORE/ ORTHOGONAL	2	1
9003.30	SHARC	30	PLANE, TOP/ ROTATED	4	0
-	BLAST2D	30	WEDGE/ MAPPED	ROE/ RIEMANN	TVD
-	STEALTH	30	WEDGE/ LAGRANGE	EXPLICIT	-

horizontal region beyond the right-most end of the wedge. The x direction velocity of the incident shock I in laboratory coordinates is $W_I = 7.29589 \times 10^4$ cm/s, or in another view, I requires 13.7063 μ s to travel 1.0 cm. The only truly relevant x direction measure in this problem is the distance along the wedge surface from the leading edge of the wedge, and thus that leading edge is defined as $x = 0.0$. These redefinitions of the (x, y) origin were used to produce the BRL coordinates for points A_w^{30} through F_w^{30} in Table 2. To allow an opportunity for the incident shock I to become "worked in" to the computational grid, it is mapped in at the time of grid generation with the shock front at $x = -1.0$ cm. The reference time for the computation is defined as $t = 0.0$ at shock arrival at the leading edge of the wedge, so the problem starting time with I at $x = -1.0$ cm is $t_0^{30} = -13.7063$ μ s. The time required for I to travel from $x = -1.0$ cm to point F at $x = 6.50$ cm is $t_F^{30} = 102.7973$ μ s. Figure 10 shows approximately 70 μ s of computational time after the theoretical arrival of incident shock I. For ease of comparison, this computation set was initially designed to provide a similar amount of time, so the minimum total real time to be simulated is $t_i^{30} = 172.7973$ μ s, resulting in a final simulated real time, rounded up, of $t_f^{30} = 160.0$ μ s. (This was later increased to $t_f^{30} = 250.0$ μ s for this and all other computations to aid in the analysis of the results at points D_w^{30} , E_w^{30} , and F_w^{30} .)

The right computational boundary was a simple transmissive outflow boundary at $x = 13.0$ cm. The left computational boundary was set up as a transmissive boundary delivering shocked air at the fixed, continuous flow conditions behind the incident shock I. The placement of this boundary in space was computed by assuming a worst-case normal reflection, shock R_n , of incident shock I at the leading edge of the wedge at $x = 0.0$. The upstream velocity in laboratory coordinates of R_n is $W_R = -3.51395 \times 10^4$ cm/s. The theoretical start of the upstream motion of R_n occurs at $t = 0.0$ at $x = 0.0$, and in a worst-case situation continues until t_f^{30} . During that time, originally 160 μ s, the upstream travel can be at most to $x = -5.622320$ cm. For simplicity, the upstream transmissive input boundary was placed at $x = -6.0$ cm for this and all other computations at this wedge angle. Thus, the total x direction active flow field length simulated was $x_i^{30} = 19.0$ cm, requiring $I_i^{30} = 190$ cells, all at $\Delta x = 0.10$ cm. The extension to $t_f^{30} = 250$ μ s did not result in any disturbing waves from the upstream boundary arriving in the area near the wedge because of the conservativeness built into the wave speed estimates. All gases in this and all other computations were air modeled as a polytropic gas, with the ratio of specific heats $\gamma = 1.4$. As noted before, all shocked air and ambient air conditions are shown in Table 1.

The HULL and SHARC codes permit the designation of numerical data sampling points called "stations" to be defined at points of interest in the flow field. A large set of fluid dynamic parameters is stored for each station, depending on whether the station has experienced either a static overpressure or a velocity magnitude change greater than a predefined limit value. Stations were defined at each of the points A_w^{30} through F_w^{30} that were used by EMI, along the wedge surface, and at various points around the flow field to monitor the progress of the computation. Complete images of the flow field were stored at various time intervals, typically every 10.0 μ s at early time in the computations.

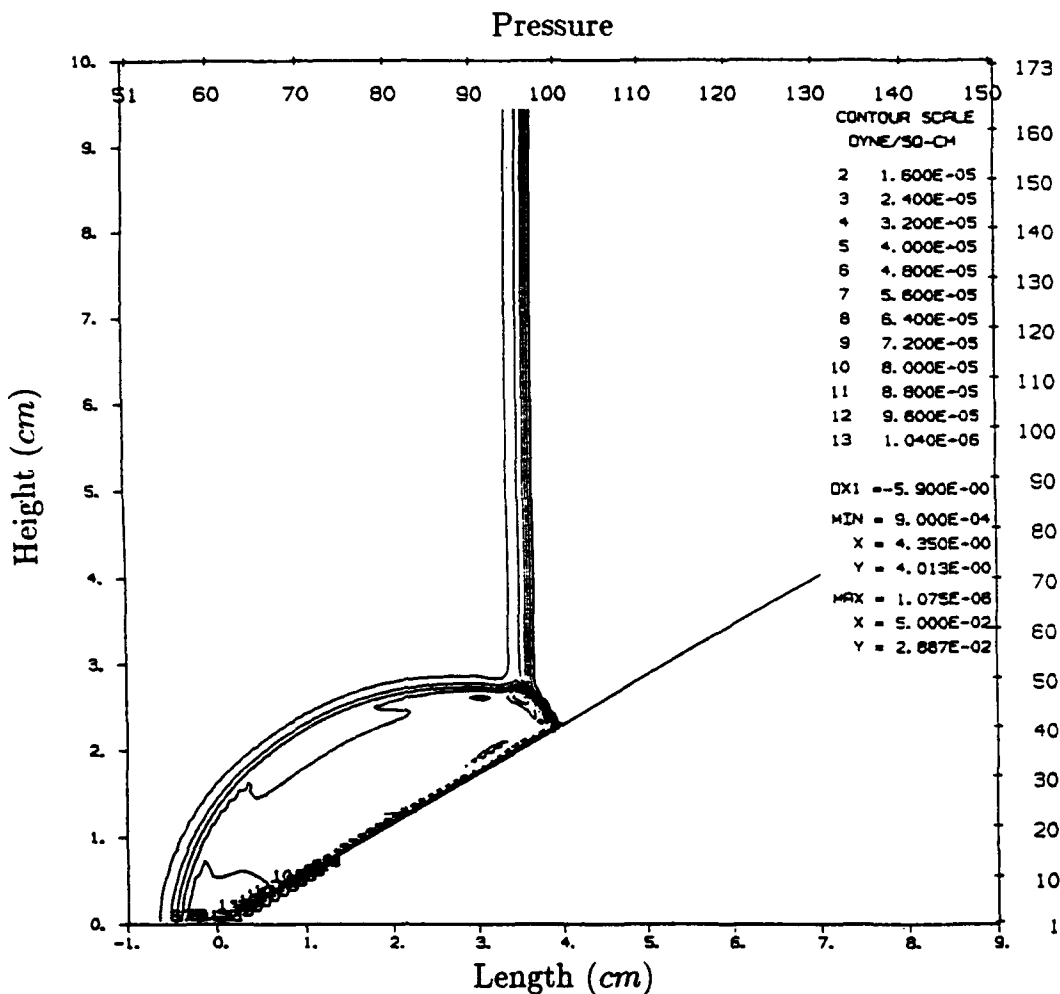


Figure 16. SHARC Problem 9003.23, 30 Degree Smooth Wedge, Absolute Pressure Contours at $50 \mu\text{s}$.

b. SHARC Computations 9003.23 and 9002.12

As may be seen in Table 3 computation 9003.23 was run with the SHARC code, using a combination of island and shore cells to model a 30 degree wedge on a reflecting plane being struck by the reference incident shock I traveling toward the wedge with its velocity vector parallel to the reflecting plane. The artificial viscosity option was turned off ($\text{visc}=0$), and the second order advection differencing ($\text{method}=4$) was used. Figure 16 shows the shock interaction with the wedge at $t = 50 \mu\text{s}$. The vertical set of pressure contours corresponds to the incident shock I which is traveling from left to right. The shock with its plane normal to the wedge surface is the Mach stem M, which is traveling to the right but with its velocity vector parallel to the wedge surface. The curved shock expanding and traveling upward and to the left is the reflected shock R. The primary purpose of Figure 16, and the many similar pressure contour and density contour figures that follow, is to give a qualitative,

not quantitative, presentation of the computational flow field to aid in understanding the results. The horizontal axis at the bottom, labeled "Length (cm)," indicates the x direction measure, and the vertical axis at the left, labeled "Height (cm)," indicates the y direction measure of the subsection of the computational grid selected for presentation. The label "Pressure" appearing above the top of the figure is provided to aid in quickly differentiating the pressure and density contour plots (labeled "Density") from one another, as they look superficially similar at a quick glance. The row of numbers along the top axis corresponds to the x direction computational cell numbers for this subsection of the computational grid, and is not of direct interest here. The column of numbers along and to the right of the right vertical axis corresponds to the y direction computational cell numbers for this subsection of the grid. The data printed in a vertical column starting at the interior upper right corner of the figure includes a list of matched pressure contour numbers and corresponding pressure levels, but the size of the figure and the overwriting of the contour numbers reduces the utility of this column significantly. Also included in this column are other summary data not essential to the present discussion. Figure 17 shows the density contours for 9003.23, also at $t = 50 \mu s$. SHARC computation 9002.12 was identical to 9003.23, except that the wedge was modeled without the use of shore cells, resulting in the stair step ramp shape discussed earlier. Figure 18 shows the shock interaction for 9002.12 with the stair step wedge at $t = 50 \mu s$. Figure 19 shows the density contours for 9002.12, also at $t = 50 \mu s$.

Figure 20 shows the pressure at point A_w^{30} for SHARC computations 9003.23 and 9002.12, which is at the same location relative to the wedge leading edge as the corresponding point A in the EMI STEALTH computation. The plots are essentially the same until approximately $30 \mu s$, after which the plot for computation 9002.12 rises above that for 9003.23. This is because of the stair step nature of 9002.12, which causes a series of small normal reflections at each island step face. Both computations show an overshoot in the pressure at the incident shock front to 51.3 kPa , 12.3 percent above the correct value of 45.7 kPa , to which it returns after $10 \mu s$. The theoretical shock pressure, the same as that measured by EMI, is shown by the lower of the two horizontal lines. Both computations are using the new SHARC second order differencing method, and both also have the artificial viscosity function turned off. Each of these options chosen in this way contributes to the severity of the pressure peak overshoot. This will be elaborated upon in later discussions of computations where permutations on these options are executed and evaluated. The second large increase in pressure in Figure 20 is caused by the passage of the reflected shock. Computation 9003.23 gives a very good indication of the passage of this reflected shock, in excellent agreement with the reference measured pressure of 74.5 kPa behind the straight section of the reflected shock, shown by the higher of the two horizontal lines, and then rises slowly because of the deceleration of the upstream flow by the expanding, but somewhat confined, reflected shock. Until the arrival of the expansion wave from the leading edge of the wedge, the pressure immediately behind the Mach stem, once it forms, is the same as that behind the straight section of the reflected shock near the triple point. The expansion wave, which is the mechanism by which the reflected shock is curved, also produces a reduced pressure behind any curved section of the reflected shock.

Figure 21 shows the pressure at point B_w^{30} for SHARC computations 9003.23 and

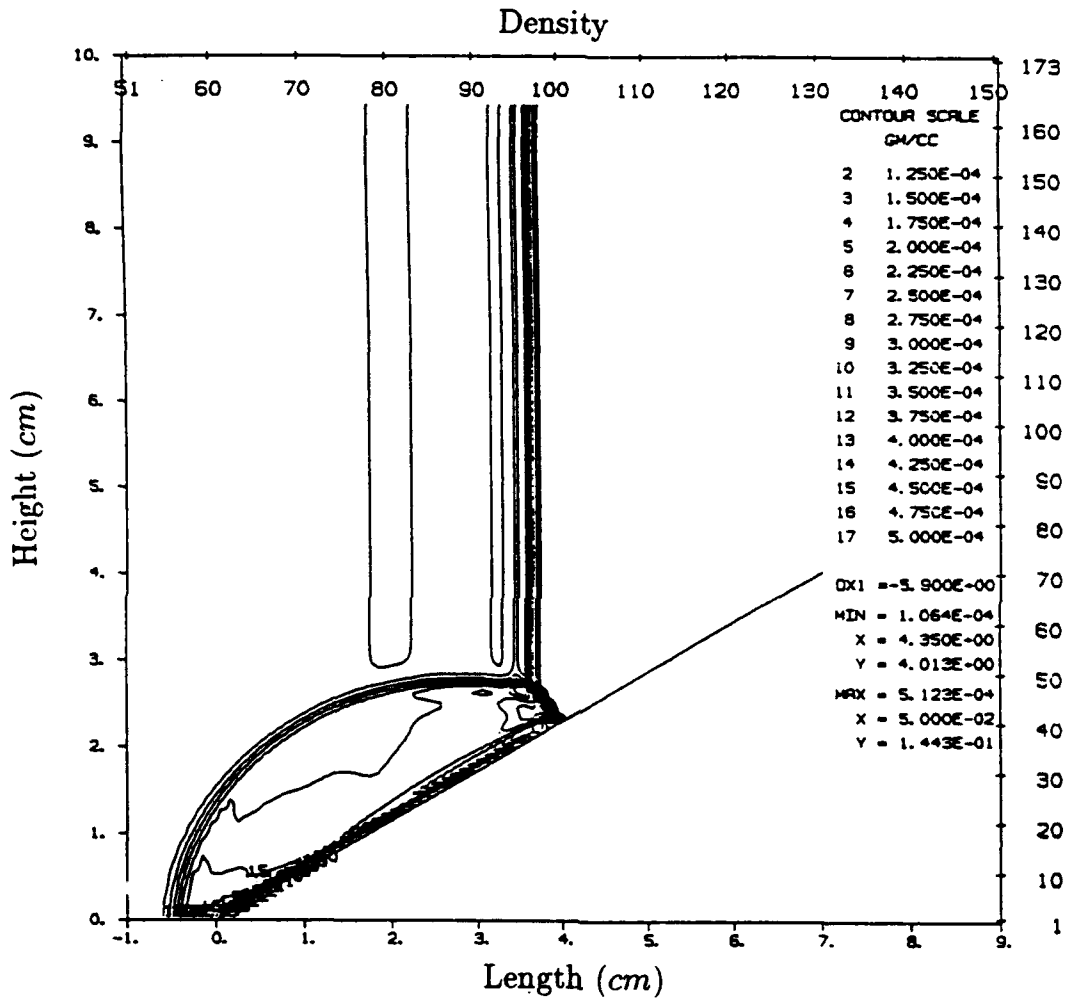


Figure 17. SHARC Problem 9003.23, 30 Degree Smooth Wedge, Density Contours at 50 μ s.

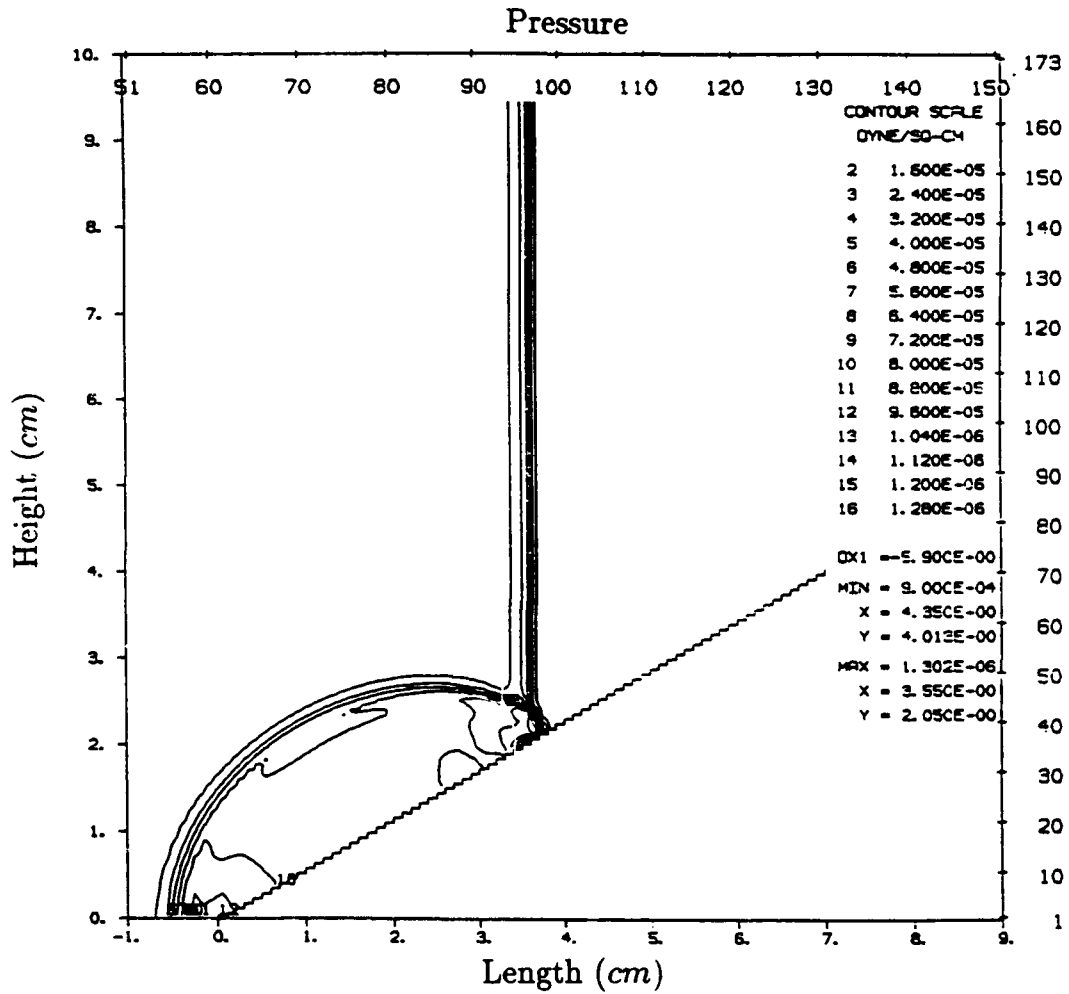


Figure 18. SHARC Problem 9002.12, 30 Degree Stair Step Wedge, Absolute Pressure Contours at 50 μ s.

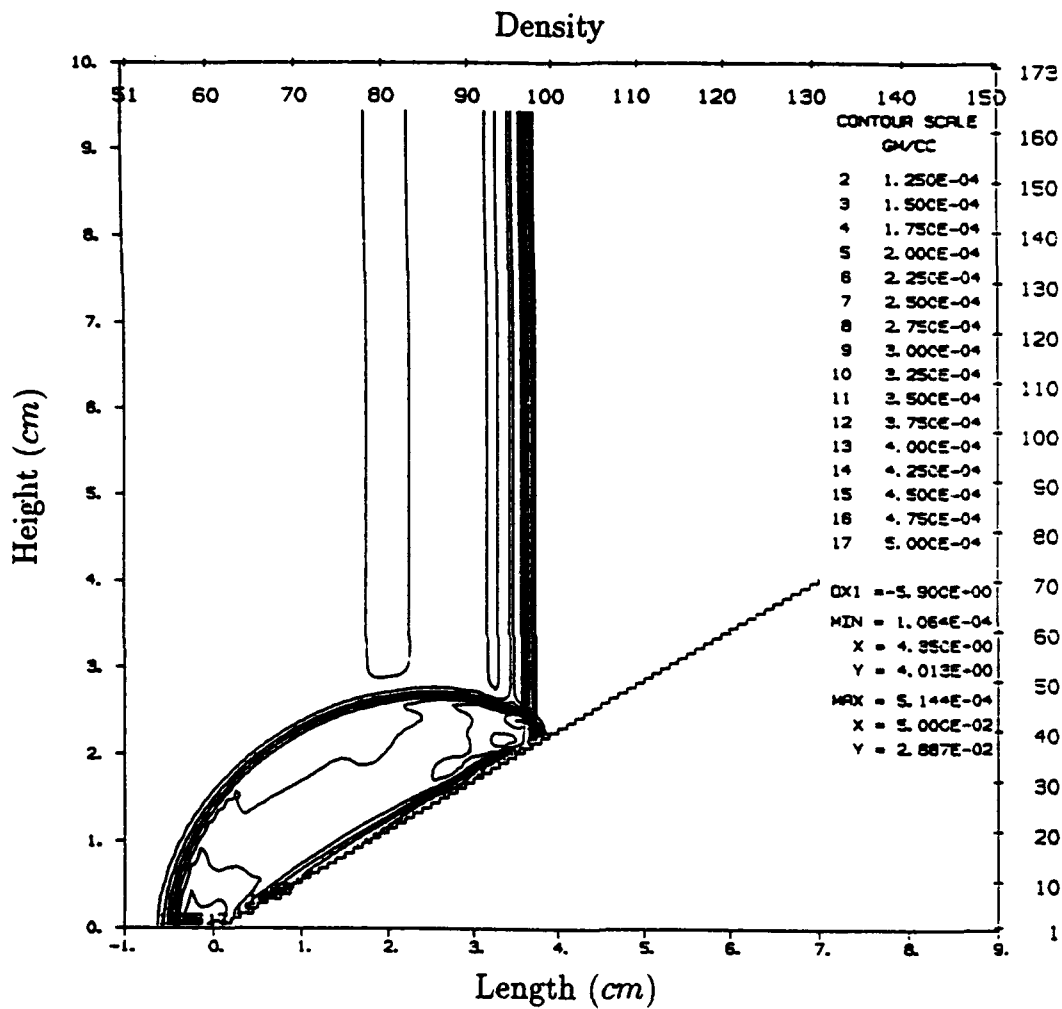


Figure 19. SHARC Problem 9002.12, 30 Degree Stair Step Wedge, Density Contours at 50 μ s.

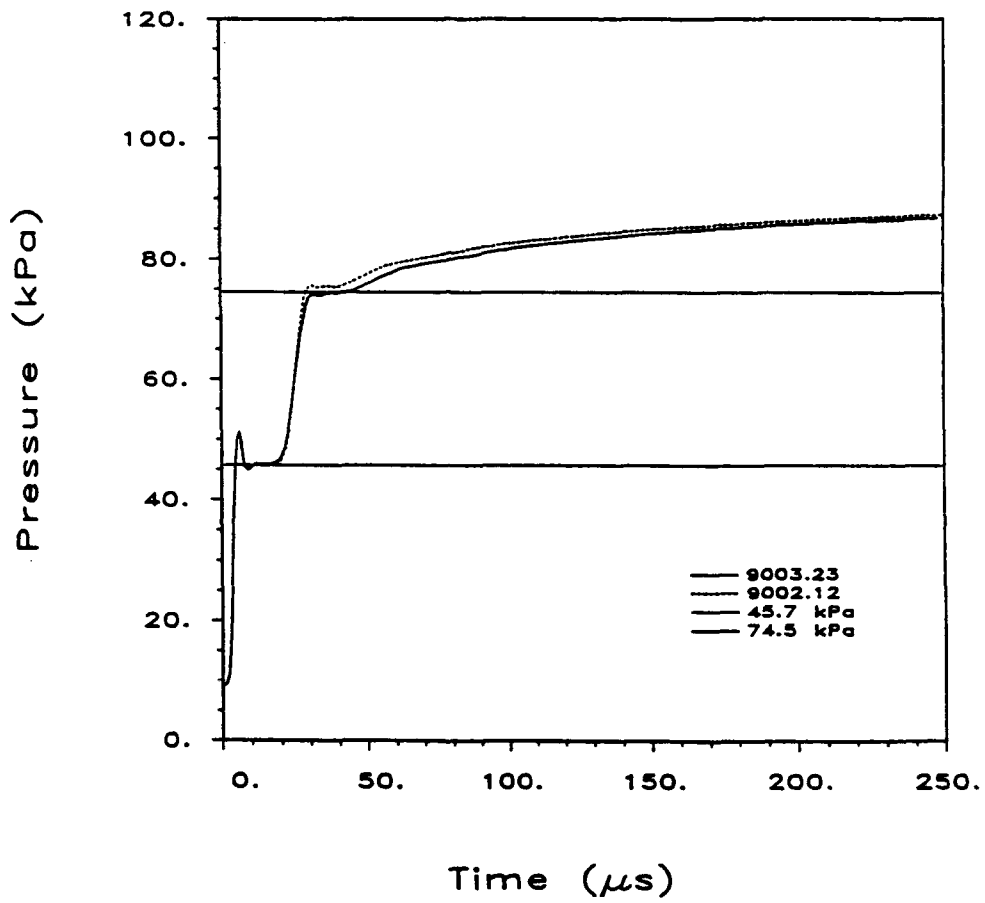


Figure 20. SHARC Problems 9003.23 and 9002.12, Absolute Pressure at Point A_w^{30} .

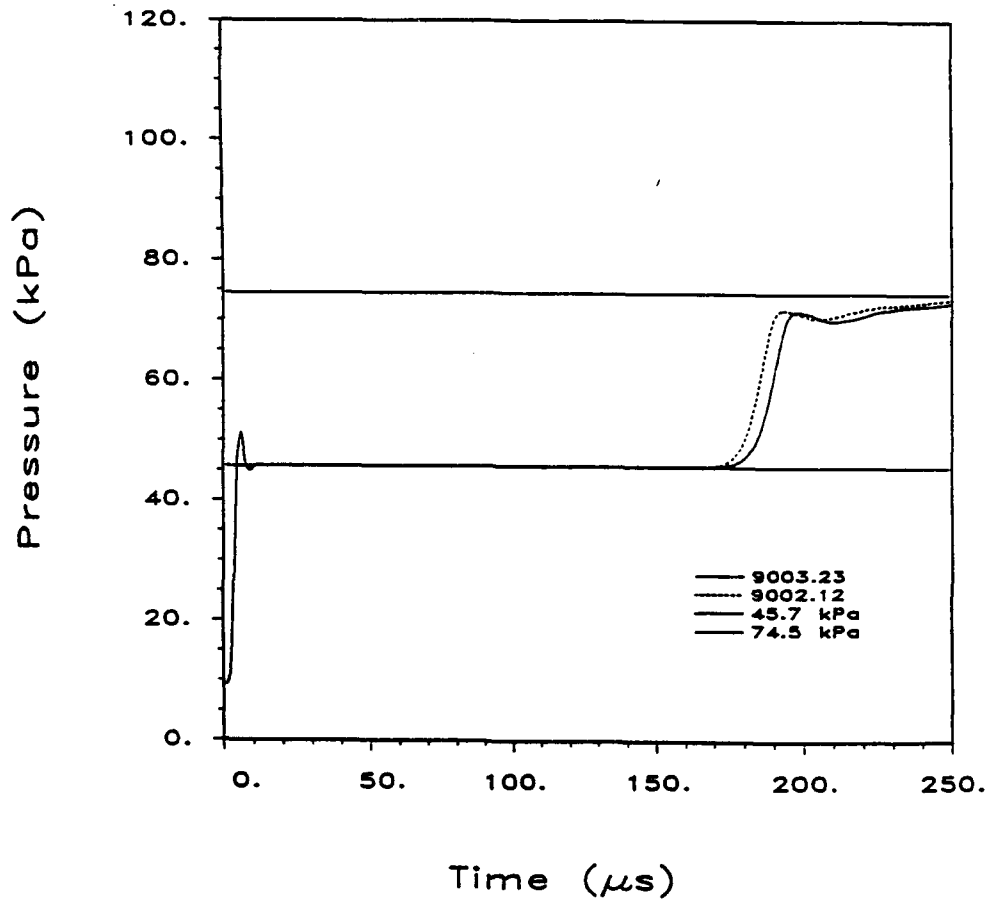


Figure 21. SHARC Problems 9003.23 and 9002.12, Absolute Pressure at Point B_w^{30} .

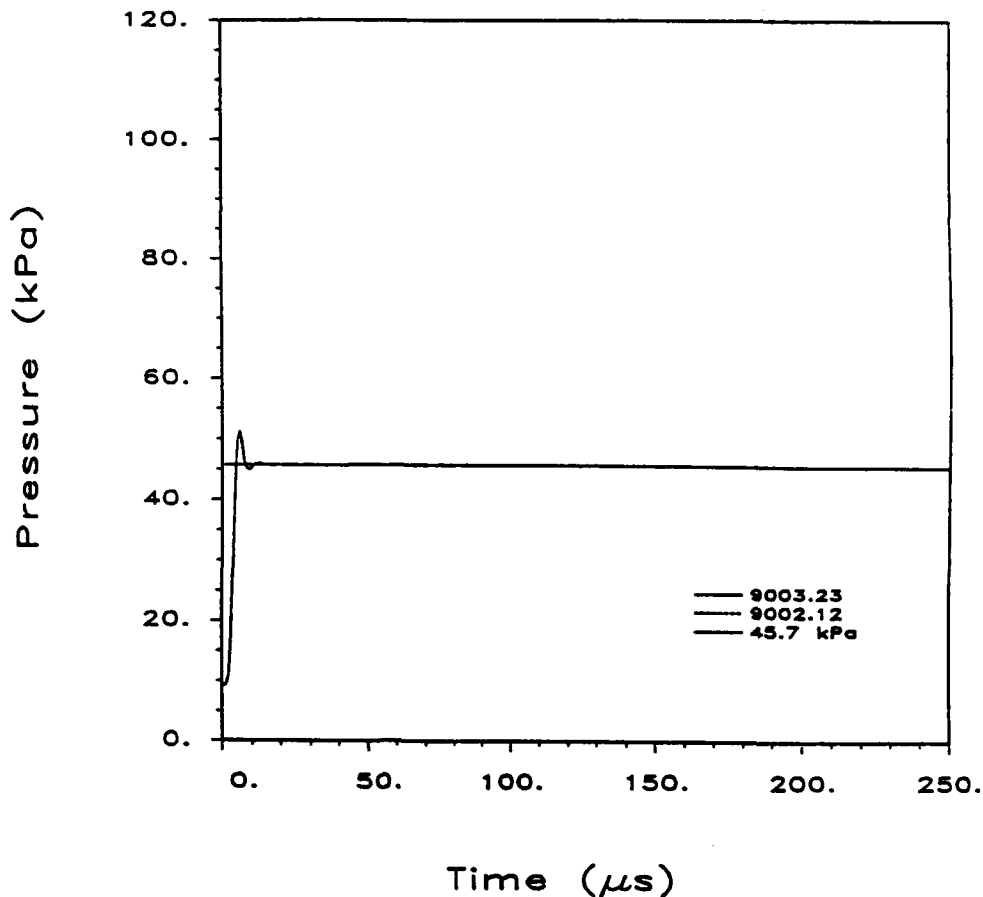


Figure 22. SHARC Problems 9003.23 and 9002.12, Absolute Pressure at Point C_w^{30} .

9002.12, which is at the same location relative to the wedge leading edge as the corresponding point B in the EMI STEALTH computation, or at least the position for point B as reported by EMI. (There is some unresolved confusion as to the actual position of point B in the EMI STEALTH computation.) Point B_w^{30} experiences both the passage of the incident shock, shown by the lower horizontal line, and the reflected shock, shown by the upper horizontal line. The plots are essentially the same until approximately $168 \mu s$, after which the plot for 9002.12 shows an early pressure increase because of the series of small normal shock interactions at the wedge stair steps. Both computations show the initial overshoot in pressure and the return to the correct incident shock pressure. They are both just below the measured reflected shock pressure of 74.5 kPa at $250 \mu s$ and still increasing.

Figure 22 shows the pressure at point C_w^{30} for SHARC computations 9003.23 and 9002.12, which is at the same location relative to the wedge leading edge as the corresponding point C in the EMI STEALTH computation. The plots overlay one another through the entire $250 \mu s$ computation time. Both computations show the initial overshoot in pressure and the return to the correct incident shock pressure of 45.7 kPa (the horizontal line) where

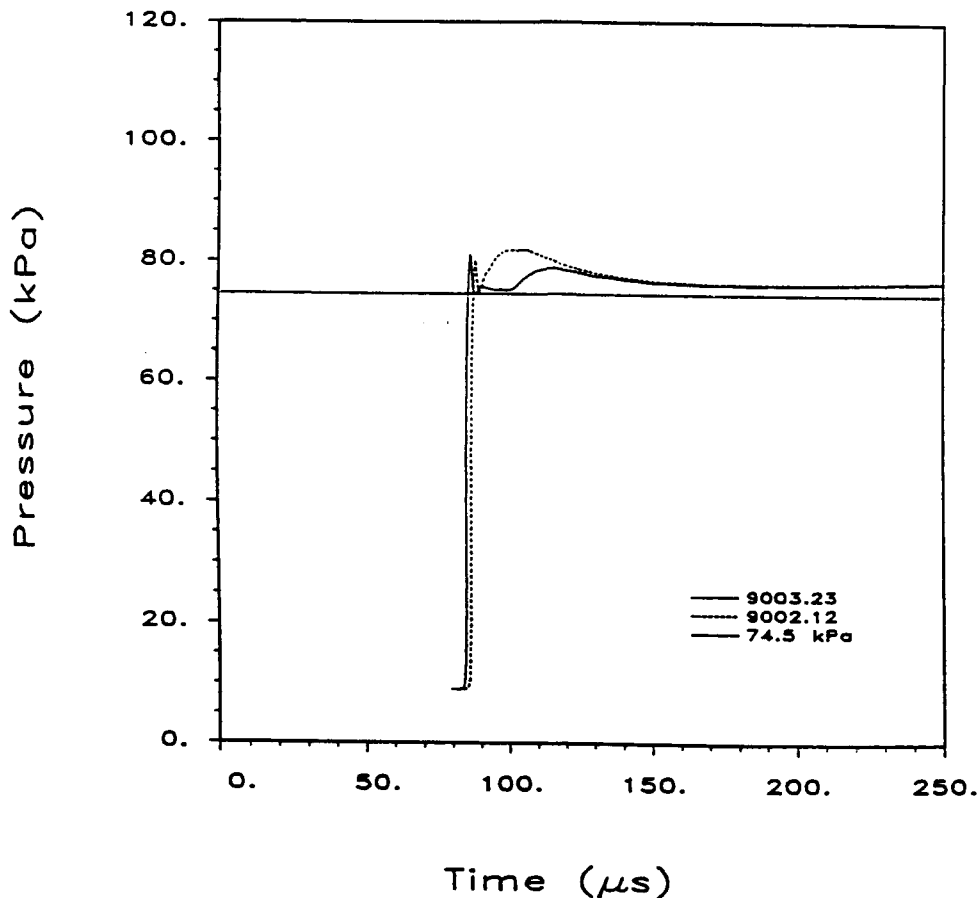


Figure 23. SHARC Problems 9003.23 and 9002.12, Absolute Pressure at Point D_w^{30} .

they remain. The simulated time of $250 \mu s$ is short enough that the reflected shock has not yet arrived at point C_w^{30} , which it ultimately should.

Figure 23 shows the pressure at point D_w^{30} for SHARC computations 9003.23 and 9002.12, which is at the same location relative to the wedge leading edge as the corresponding point D in the EMI STEALTH computation. Point D_w^{30} experiences only the passage of the Mach stem. Both computations seem to have a leading overshoot in pressure behind the Mach stem that is similar in relative size to that on the incident shock. Computation 9003.23 gives a good indication of the Mach stem pressure by $100 \mu s$, with a value of $75.2 kPa$, 0.9 percent above the experimental value of $74.5 kPa$. The disruption of the Mach stem that can be detected qualitatively by comparing Figures 17 and 19 can be seen in a more quantitative way here. The series of small normal shock reflections in computation 9002.12 as the incident shock interacts with the wedge delays the progress of the Mach stem up the wedge, and changes its pressure (and other flow parameters) immediately behind the Mach stem. This disruption can be made less severe by reducing the flow field cell sizes in 9002.12, (*i.e.*, going to higher grid resolution), but at a cost in a required increase in

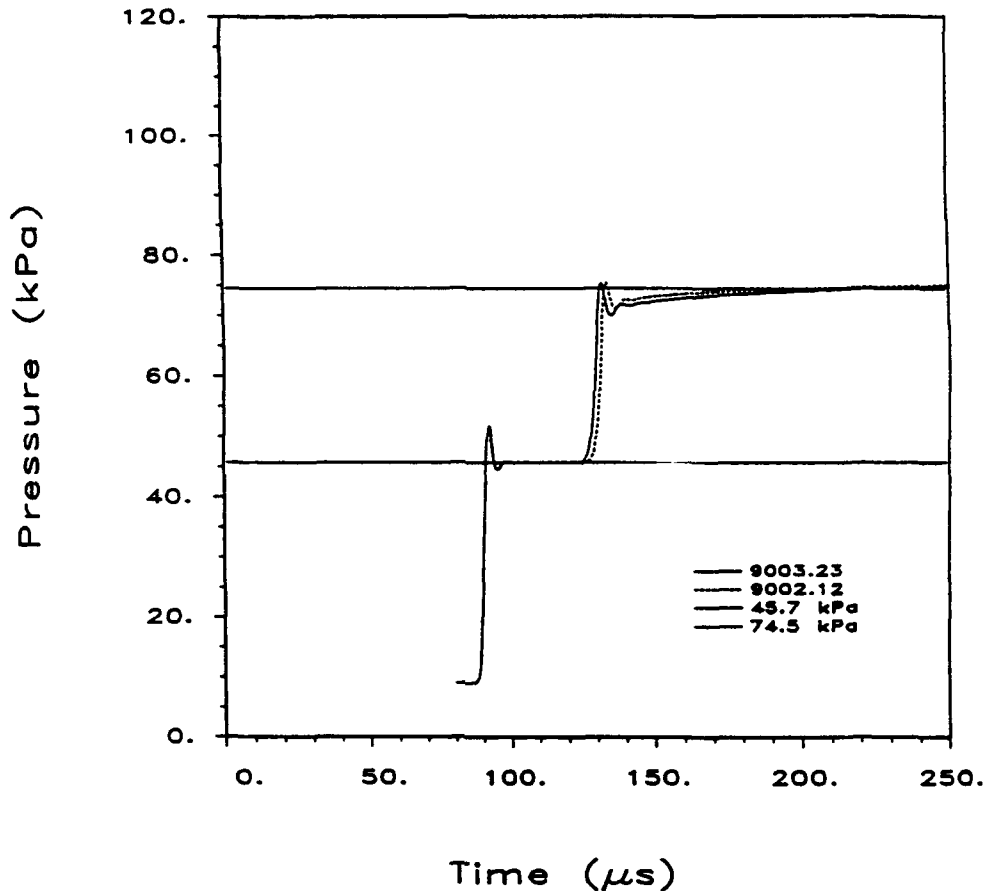


Figure 24. SHARC Problems 9003.23 and 9002.12, Absolute Pressure at Point E_w^{30} .

computational resources. This also serves to illustrate an important point. Computation 9002.12 does show “reasonable” looking pressure contours in Figure 18 and density contours in Figure 19 if evaluated alone, or possibly even compared with shadowgraphs. The actual timing of waves and numerical values of pressure and wave speeds must also be compared to make a definitive comparison. Put in mathematical terms, similarity of contours to shadowgraphs is a necessary, but not sufficient, condition to declare equality of a computation to an experiment. As may be seen in Figure 23, the pressures at position D_w^{30} in the two computations are essentially the same after 150 μs .

Figure 24 shows the pressure at point E_w^{30} for SHARC computations 9003.23 and 9002.12, which is at the same location relative to the wedge leading edge as the corresponding point E in the EMI STEALTH computation. As with point B_w^{30} , point E_w^{30} experiences the passage of the incident shock and the reflected shock. The delay and disruption of the Mach stem in computation 9002.12 is shown only indirectly here through a relatively minor time delay in the passage of the reflected shock. Both computations show essentially the same pressure at 250 μs .

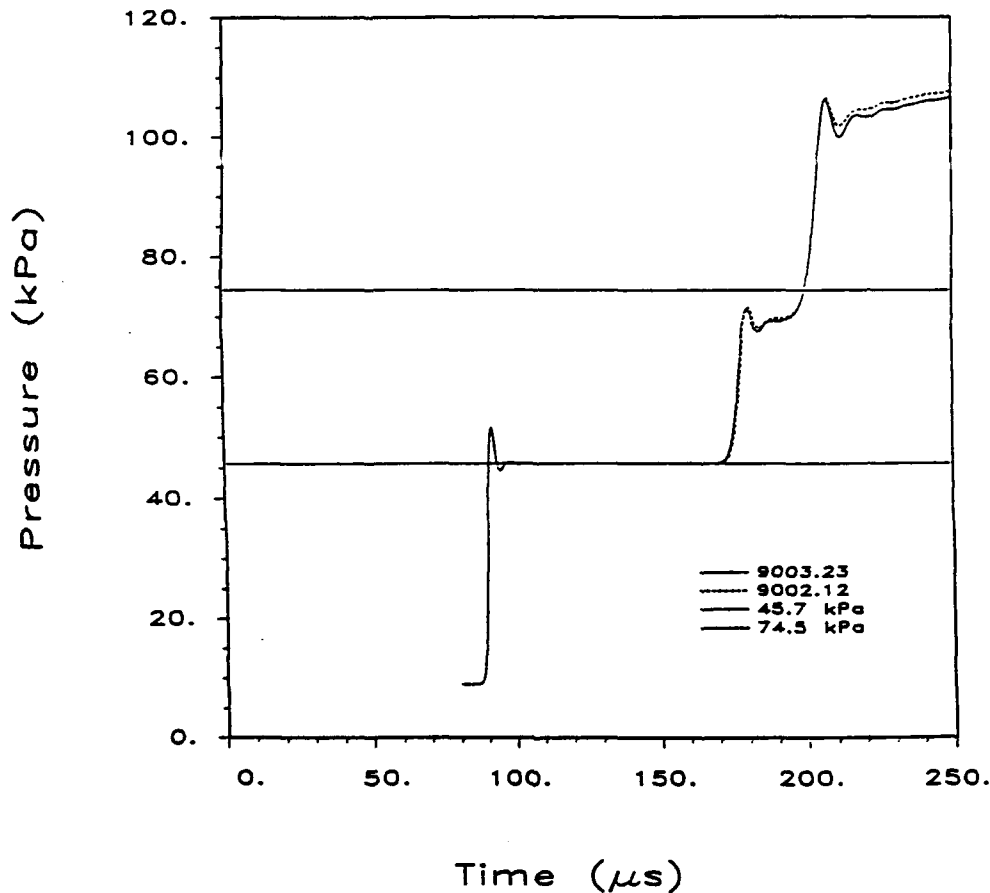


Figure 25. SHARC Problems 9003.23 and 9002.12, Absolute Pressure at Point F_w^{30} .

Figure 25 shows the pressure at point F_w^{30} for SHARC computations 9003.23 and 9002.12, which is at the same location relative to the wedge leading edge as the corresponding point F in the EMI STEALTH computation. Point F_w^{30} experiences the passage of both the incident shock and the reflected shock, and then a reflection from the top reflective computational boundary of the reflected shock arriving at about $195 \mu s$ which is not relevant here. This point gives a good indication that if far field effects are the primary item of interest, the modeling of the wedge surface with either the shore cells or a stair step is not important for this configuration of incident shock strength and wedge angle.

c. SHARC Computations 9003.23, 9003.26, 9003.27, and 9003.28

It was indicated above that results from performing permutations on the differencing method and artificial viscosity options would be discussed. Computation 9003.23, serving here as a reference computation, was run with a Mach 2.12 shock wave traveling orthogonally through the grid, a simulated 30 degree wedge of island plus shore cells modeled on a bottom

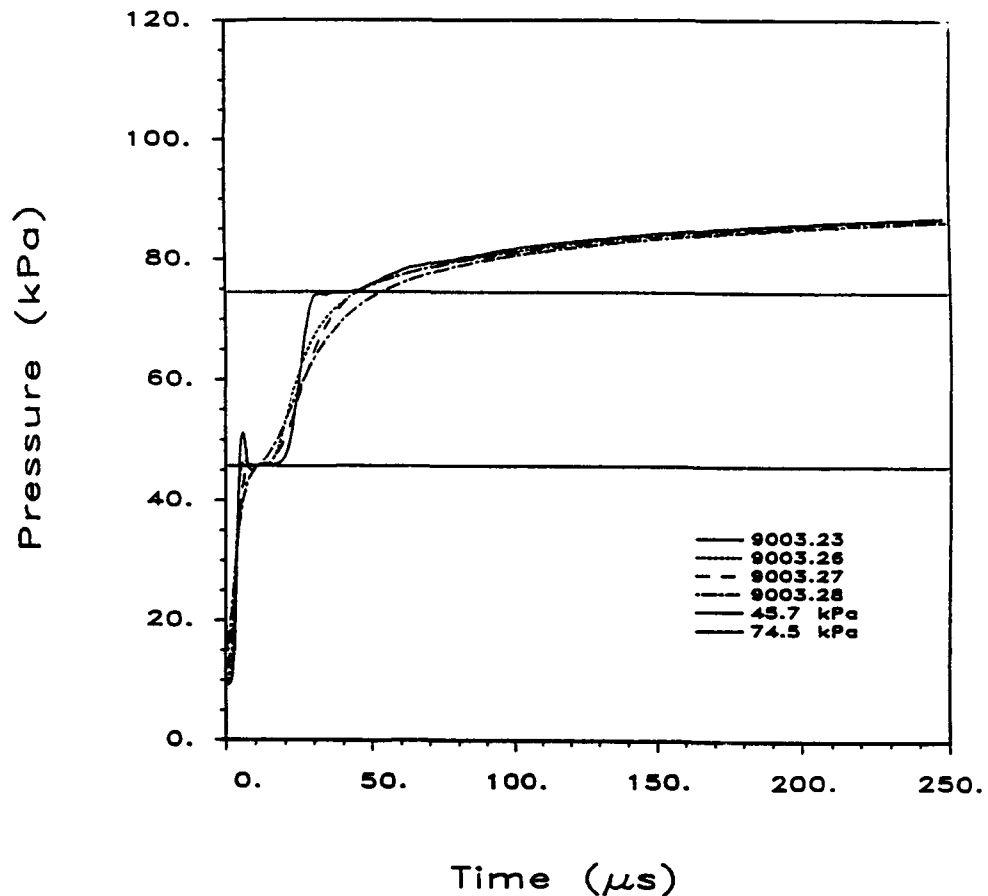


Figure 26. SHARC Problems 9003.23, 9003.26, 9003.27, and 9003.28, Absolute Pressure at Point A_w^{30} .

reflecting plane, artificial viscosity turned off ($\text{visc} = 0$), and with the new SHARC second order advection ($\text{method} = 4$). This is summarized in Table 3. Also listed in Table 3 are the other computations to be discussed here, computations 9003.26, 9003.27, and 9003.28. These computations differ from 9003.23 only in the selection of the artificial viscosity and differencing method option. Computation 9003.26 was run with artificial viscosity turned off, and with the net first order differencing ($\text{method} = 2$), which is very similar to the standard HULL differencing method. Computation 9003.27 was run with the second order advection differencing, and with artificial viscosity turned on ($\text{visc} = 1$). To complete this set, computation 9003.28 was run with the net first order differencing method, and with artificial viscosity turned on. All other aspects of the computational grids and the positions of the points A_w^{30} through F_w^{30} are the same. Thus, the effects of each option individually and in combination with the other can be determined.

Figure 26 shows the pressure at point A_w^{30} for these SHARC computations. Differences in the plots begin to appear immediately after the computations are started. Computation 9003.23 has already been discussed in some detail, so little more about it needs to be directly

discussed. The pressure versus time for computation 9003.23 is represented by the solid curve. The solid horizontal lines at 45.7 kPa and 74.5 kPa represent the experimentally measured incident and reflected shock pressures as previously defined. Computation 9003.26, shown by the short dash curve, shows the diffusive effects of the first order donor cell differencing. The computational shock is spread out over a longer period of time, and hence physical space, than that for 9003.23. The diffusive nature of the computation does greatly reduce the initial overshoot. The incident shock level of 45.7 kPa is shown clearly. Comparing 9003.23 (the solid line) with 9003.26 immediately isolates the second order advection method as the cause of the overshoot in the incident shock pressure in 9003.23. While there is relatively little slowing of the shock rise time in 9003.26 relative to 9003.23, that may be misleading here because of the very limited distance that the shock has traveled so far in the grid. Also, 9003.26 does still have a small overshoot.

The variation in results shown in Figure 26 for the reflected shock at point A_w^{30} is considerably greater. Computation 9003.23, as noted before, gives an excellent indication of the briefly steady reflected shock pressure, with a relatively rapid rise time. The other computations, ranked from least to most diffusive, are 9003.26, 9003.27, and 9003.28. None give a good indicator of the 74.5 kPa reflected shock pressure before upstream reflected wave effects cause the general upward drift in pressure. Computation 9003.27, represented by the long dash curve, shows similar behavior to that for 9003.26, but with variations. The initial shock rise time is slightly longer than that for 9003.26, while the reflected shock has a similar rise time but a different shape. Finally, computation 9003.28, shown by the alternating long and short dash curve, is by far the most diffusive, having both artificial viscosity and the first order donor cell differencing. All computations eventually predict nearly the same pressure at late time. It should be noted that comparisons at point A_w^{30} are a relatively stringent test of the computations because of the close proximity of point A_w^{30} to both the leading edge of the wedge and the wedge surface itself.

Figure 27 shows the results for the same four computations for point B_w^{30} . The trends are similar to those for point A_w^{30} , with the computations showing great differences in the rise times for the reflected shock. Figure 28 simply shows the passage across point C_w^{30} of the incident shock. Except for the actual shock rise time, the computations are essentially identical, with all of them showing the correct pressure behind the incident shock. Figure 29 is very interesting. It shows the passage of only the Mach stem at point D_w^{30} . Because this is a much stronger shock than the incident shock, it has more intrinsic self steepening characteristics. As a result, the shock rise times are nearly identical, with some transient divergent behavior afterward, followed by convergence to the same solution. Figure 30 for point E_w^{30} is interesting because it has the same two shock types, incident and reflected, as does point B_w^{30} . Although the various rise times for the incident shock for the four computations are nearly the same for the two points, the rise times for point E_w^{30} are all quicker than for point B_w^{30} , with the computations for point E_w^{30} clearly associated within the set of computations by the use of artificial viscosity. Finally, Figure 31 shows the pressure versus time for the four computations for point F_w^{30} . Here again, the grouping of the results is associated with the choice of artificial viscosity. None of the computations show a plateau at the reference reflected shock pressure of 74.5 kPa, but it is unclear whether or not an

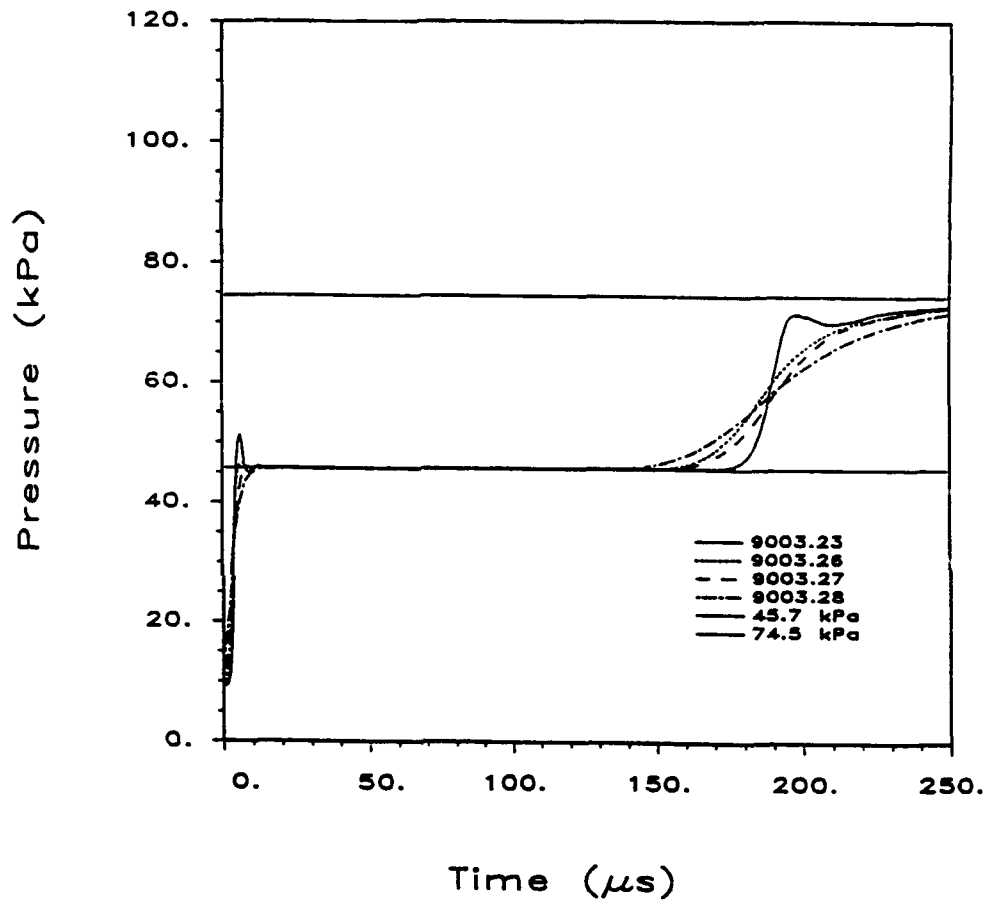


Figure 27. SHARC Problems 9003.23, 9003.26, 9003.27, and 9003.28, Absolute Pressure at Point B_w^{30} .

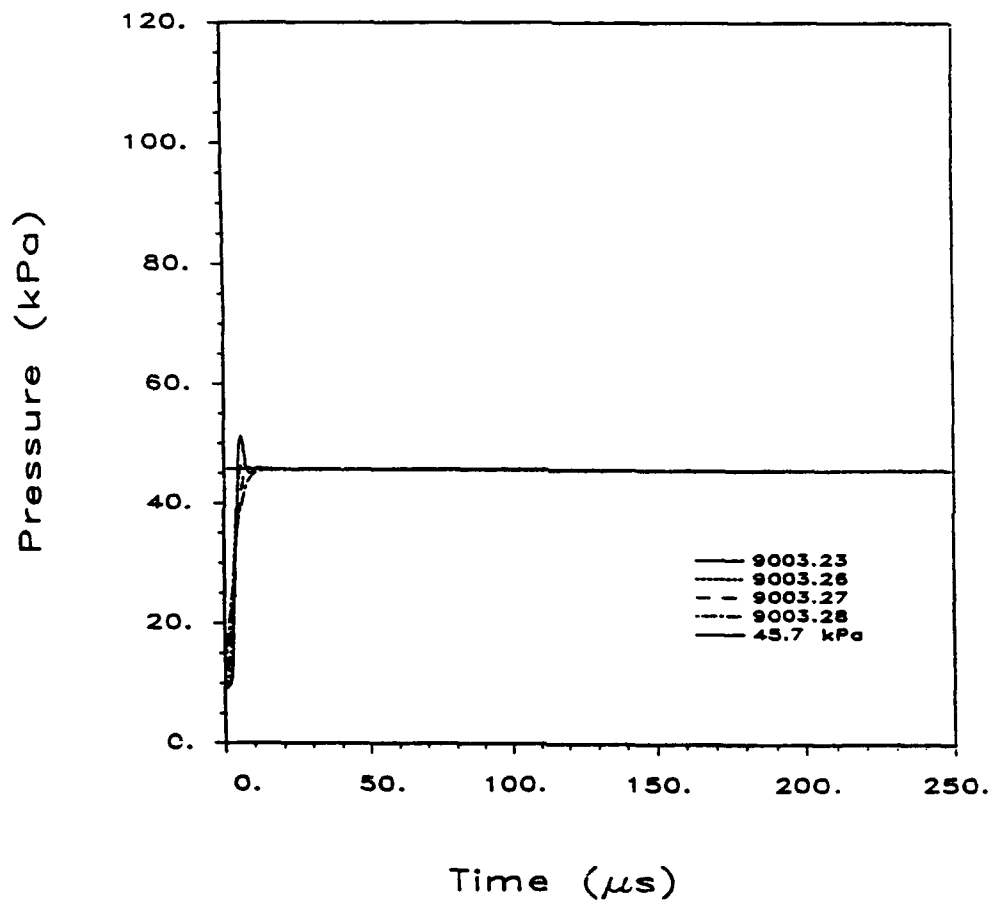


Figure 28. SHARC Problems 9003.23, 9003.26, 9003.27, and 9003.28, Absolute Pressure at Point C_w^{30} .

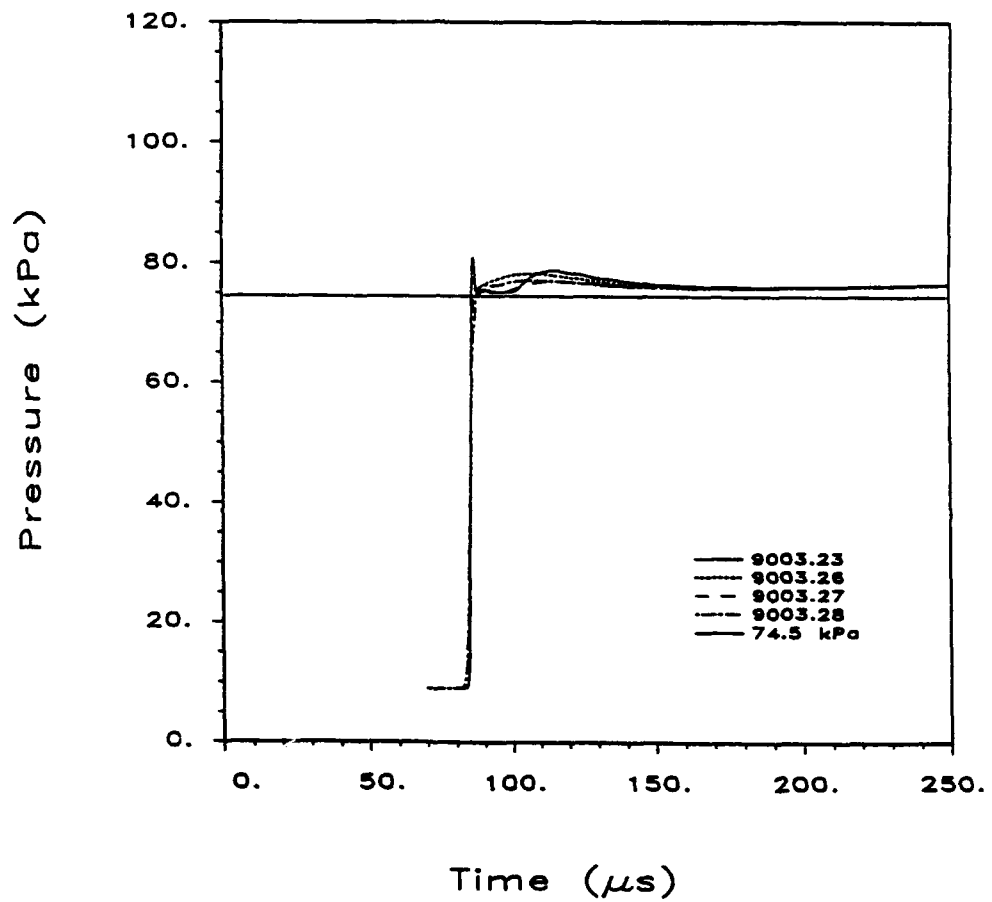


Figure 29. SHARC Problems 9003.23, 9003.26, 9003.27, and 9003.28, Absolute Pressure at Point D_w^{30} .

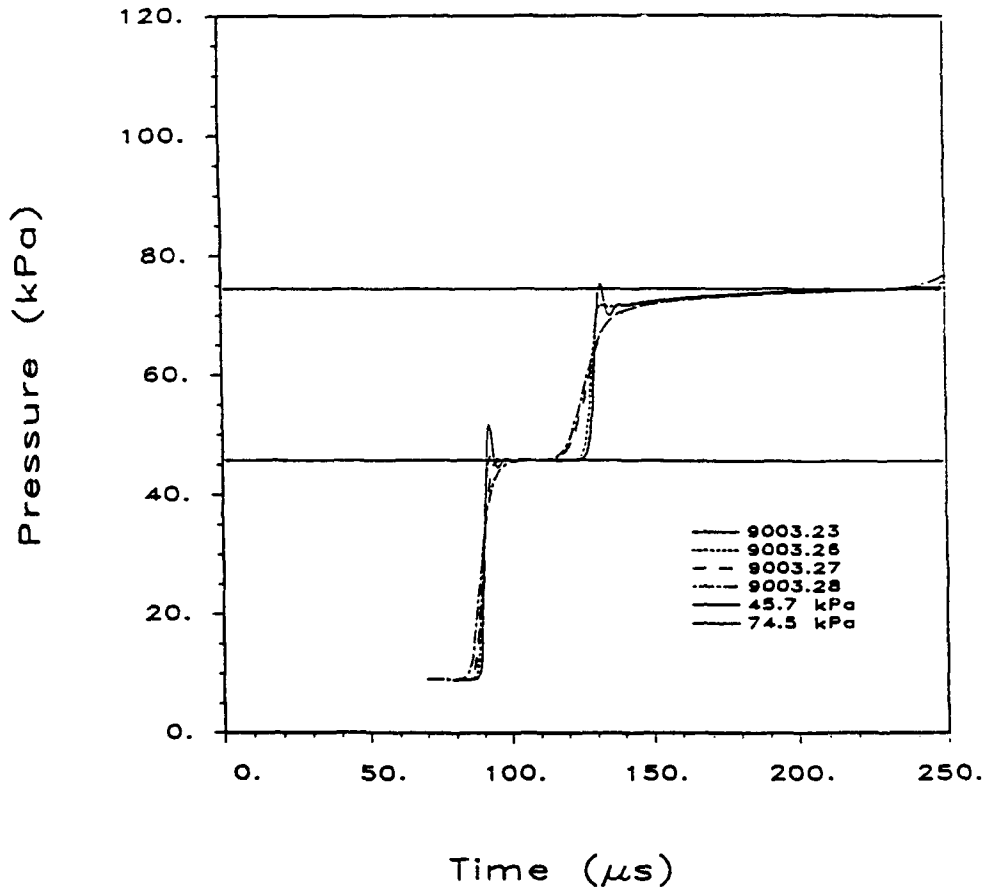


Figure 30. SHARC Problems 9003.23, 9003.26, 9003.27, and 9003.28, Absolute Pressure at Point E_w^{30} .

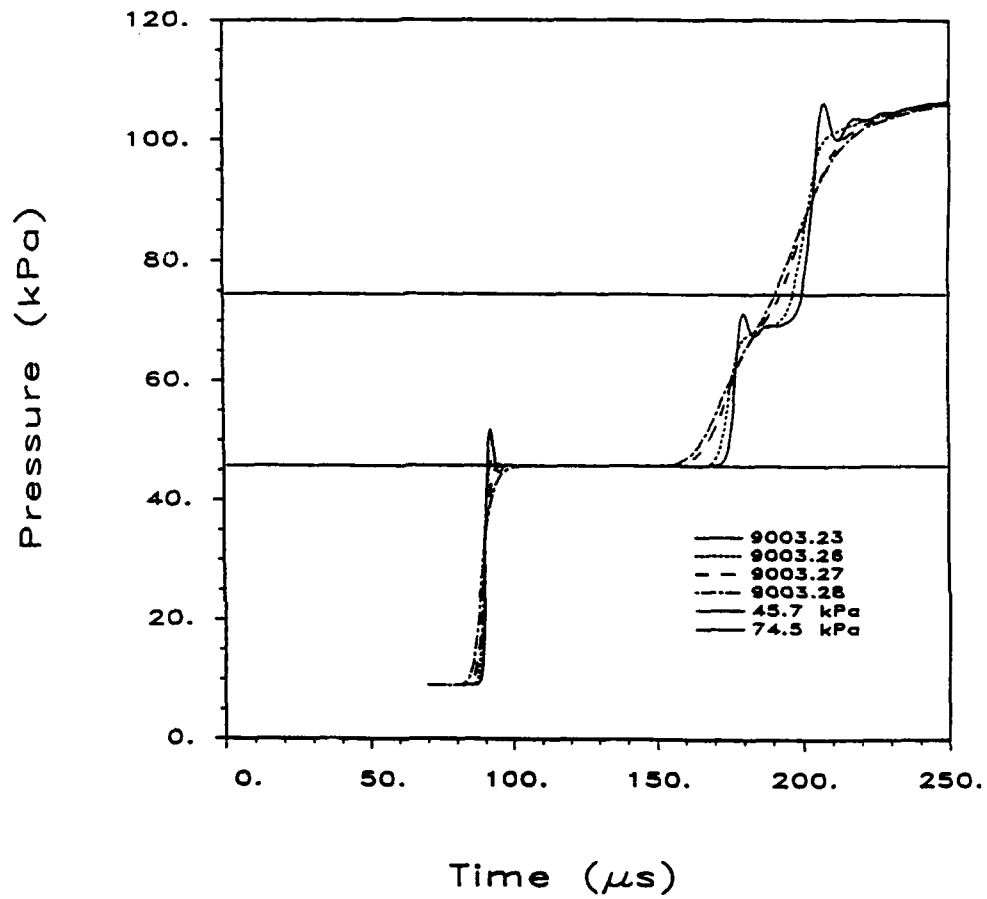


Figure 31. SHARC Problems 9003.23, 9003.26, 9003.27, and 9003.28, Absolute Pressure at Point F_w^{30} .

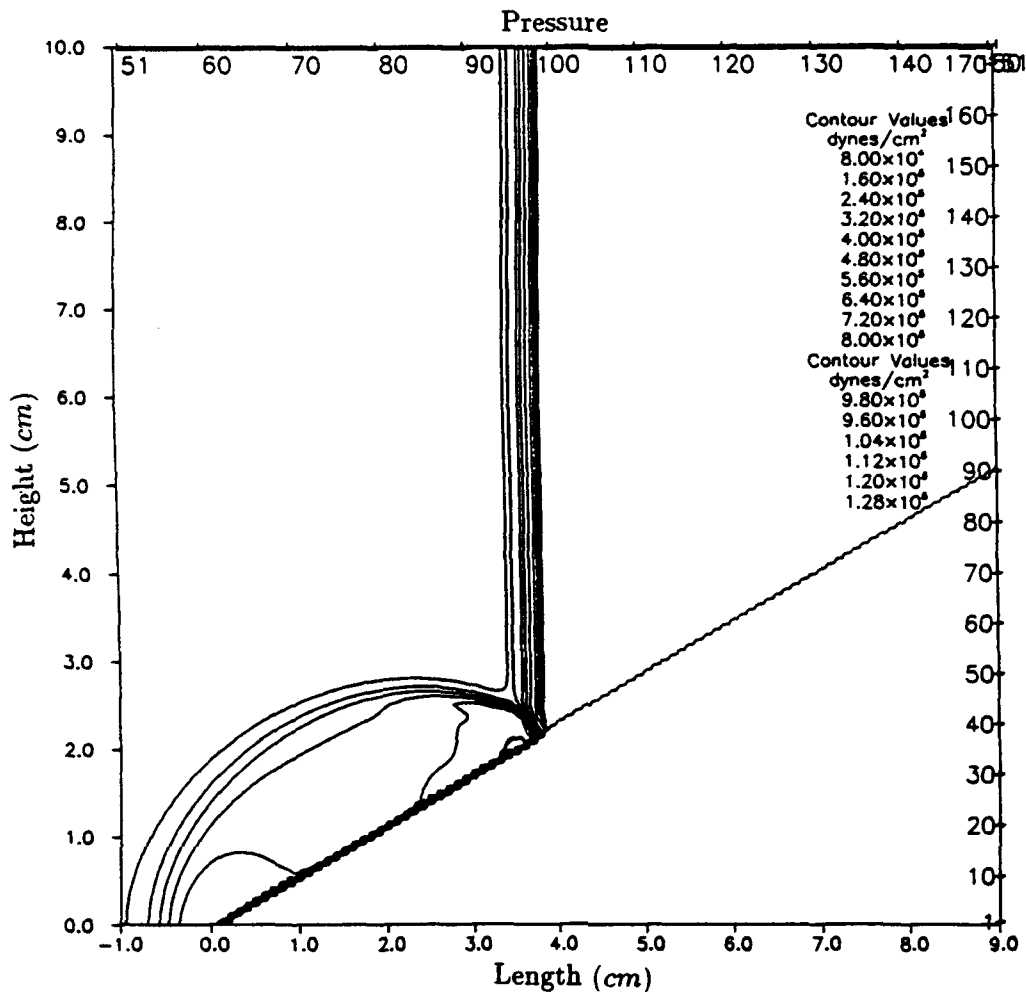


Figure 32. HULL122 Problem 8912.071, 30 Degree Stair Step Wedge, Absolute Pressure Contours at $50 \mu\text{s}$.

undisturbed reflected shock can physically arrive at that point prior to being overtaken by the corner expansion wave.

d. HULL122 Computations 8912.071 and 9001.181

As indicated earlier, computations were also performed using version 122 of the HULL hydrocode, hereinafter referred to as "HULL122." Computation number 8912.071 simulated the 30 degree wedge with a stair step ramp of island cells on the bottom reflecting plane, in a computational grid design similar to that depicted in Figure 12 and also used for SHARC computation 9002.12. Figure 32 shows the absolute pressure contours for the shock interaction for 8912.071 with the stair step wedge at $t = 50 \mu\text{s}$. Figure 33 shows the density contours for 8912.071, also at $t = 50 \mu\text{s}$. Computation number 9001.181 simulated both the

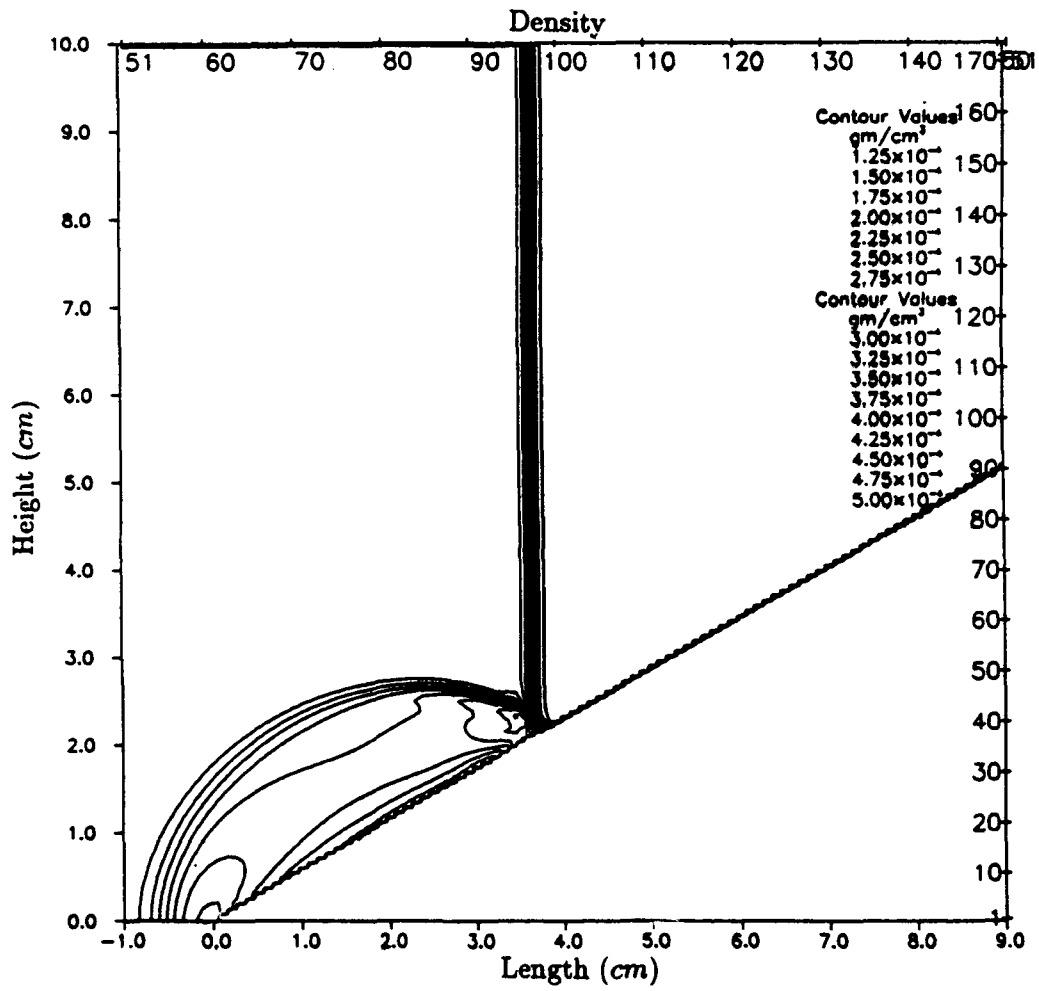


Figure 33. HULL122 Problem 8912.071, 30 Degree Stair Step Wedge, Density Contours at 50 μ s.

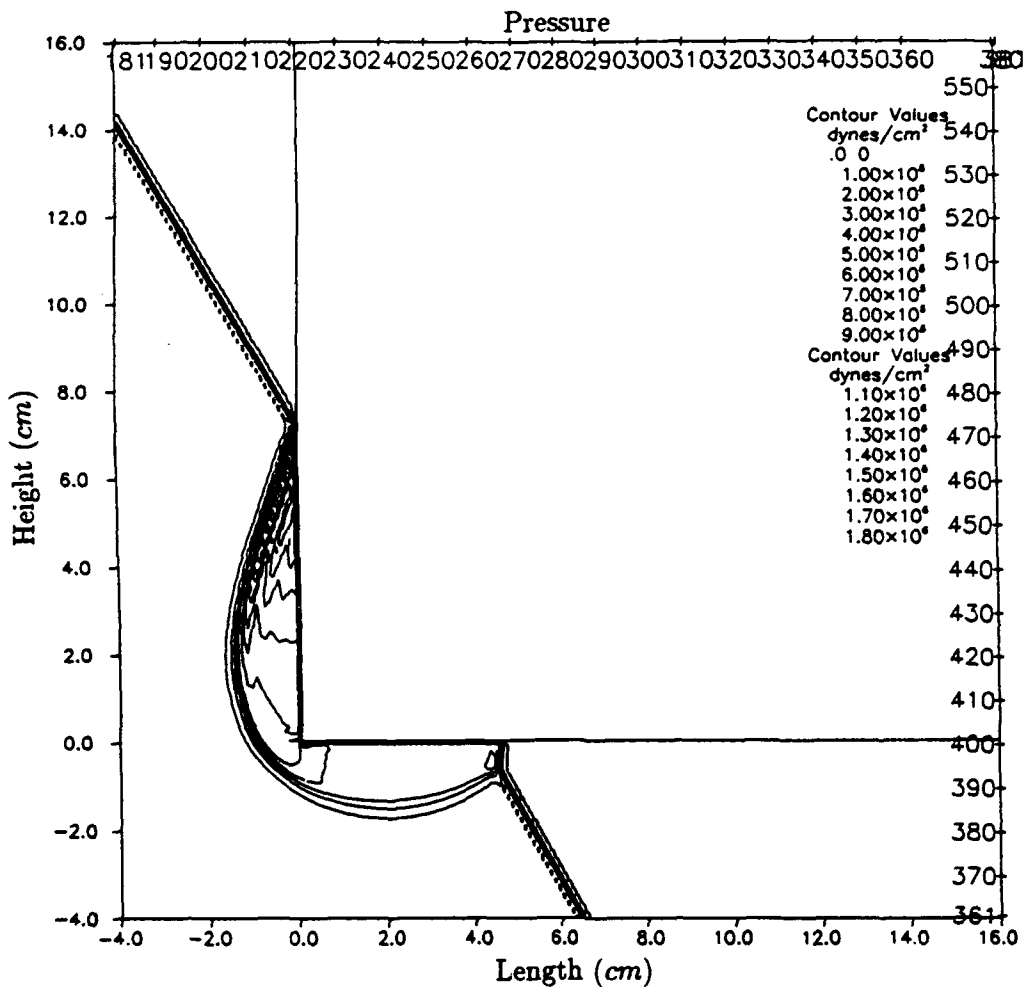


Figure 34. HULL122 Problem 9001.181, 30 Degree Smooth Wedge (Bottom) and 60 Degree Smooth Wedge (Left), Absolute Pressure Contours at 50 μ s.

30 degree and 60 degree wedge interactions within one computation using a rotated shock striking a rectangular block of island cells, in a manner similar to that depicted in Figure 14. This computation was run to a final time $t_f = 300 \mu$ s, primarily to generate a consistent set of pressure time histories for the 60 degree wedge computations to be discussed later. Figure 34 shows the absolute pressure contours for the shock interaction for 9001.181 with the wedge (rotated shock and block combination) at $t = 50 \mu$ s. The interaction of the $M_I = 2.12$ incident shock with a 30 degree wedge is shown in the lower right quadrant of the figure, and on the bottom horizontal boundary of the rectangular block. The top and right sides of the block are not simulated in this computation simply because it is not necessary to model that computational space. The interaction of the same shock with a 60 degree wedge is also shown in Figure 34 by the interaction on the left vertical boundary of the rectangular block. The 60 degree interaction will be discussed later. Figure 35 shows the corresponding

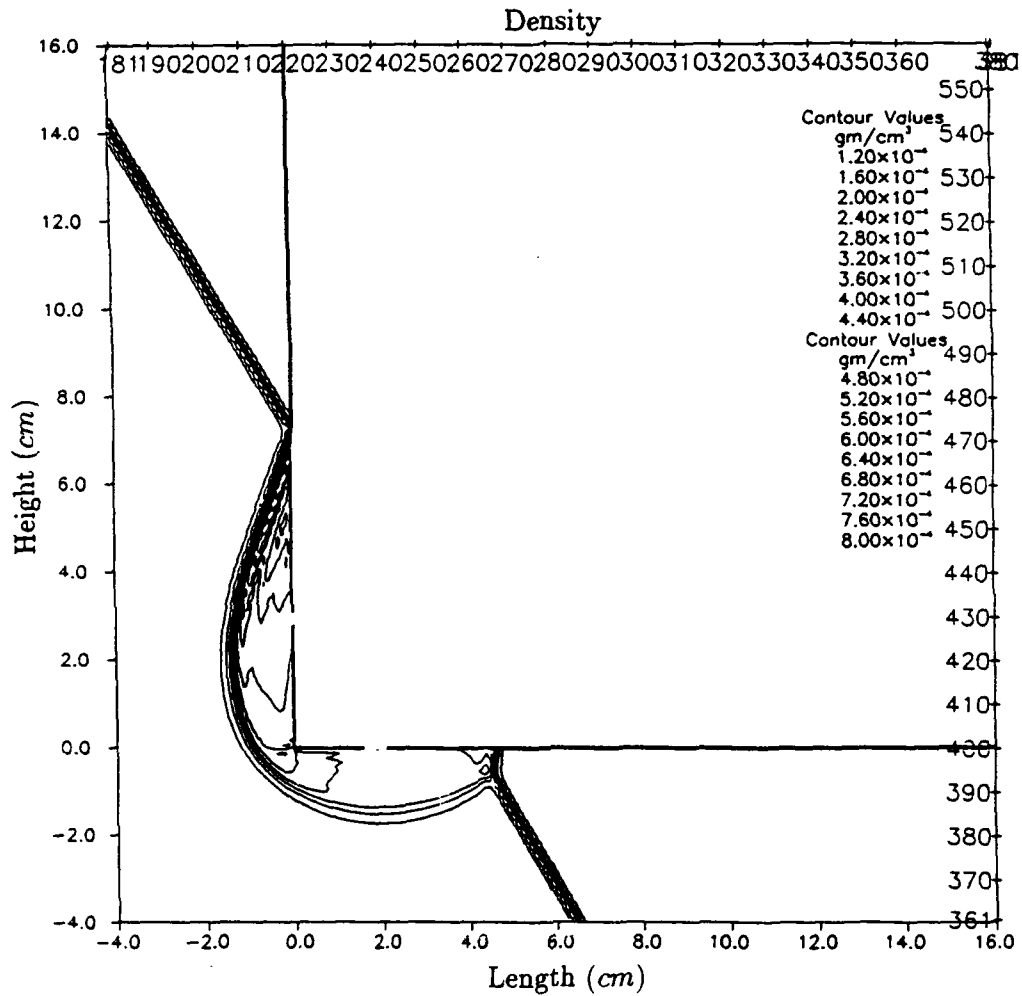


Figure 35. HULL122 Problem 9001.181, 30 Degree Smooth Wedge (Bottom) and 60 Degree Smooth Wedge (Left), Density Contours at 50 μ s.

density contours for both the 30 *degree* (bottom horizontal boundary of the block) and the 60 *degree* (left vertical boundary) wedge sides of the block for 9001.181, also at $t = 50 \mu s$.

The next set of figures shows the absolute pressure versus time for points A_w^{30} through F_w^{30} and A_{bb}^{30} through F_{bb}^{30} for these two computations. As a reminder, it was indicated earlier that the subscript "w" refers to points above a wedge on a reflecting plane struck by an orthogonally oriented shock, and the subscript "bb" to points below the bottom boundary of an orthogonally oriented block struck by a rotated shock. Both computations were run using the "standard" HULL differencing (method = 2), with no artificial viscosity. There are three basic reasons why the results for the two computations are different from one another. The first is that 8912.071 has a shock interacting with a stair step ramp, while 9001.181 has a shock interacting with a smooth surface. The second is that 8912.071 has a reflecting plane upstream from the leading edge of the wedge, while 9001.181 has a wedge leading edge simulated by a 90 *degree* corner in a rotated free stream. The earlier discussion concerning differences in the reflected shock structure, corner expansion wave, and communication around the corner is relevant here. The third difference is more subtle. Even though the two computational grids were set up using the same cell sizes ($\Delta x = 0.1 \text{ cm}$) in the areas of interest, the grid for the rotated shock appears to affect the computational shock as if it had a lower resolution, more on the order of $\Delta x' = \Delta x / \cos\Theta$. To be a valid comparison, the computations for an orthogonally located shock striking a 30 *degree* wedge on a reflecting plane and a rotated shock striking the bottom of a rectangular block must be compared at topologically equivalent points. A new set of points, A_{bb}^{30} through F_{bb}^{30} , off the bottom boundary of the rectangular block were defined. These points were positioned in such a way that they were located at the same *normal* distances to both the incident shock and the bottom surface of the rectangular block as were their A_w^{30} through F_w^{30} counterparts. Thus, all shock arrival times and growing rates are directly comparable, except for differences caused by the modeling techniques, which are the objects of this study. As with the true wedge computations, the incident shock was started at a position 1.0 *cm* upstream from the leading corner of the block, measured along the incident shock velocity vector. The leading corner of the block was defined in the grid as position (0.0, 0.0). Table 4 shows the rounded-off

Table 4. BRL Points A_{bb}^{30} - F_{bb}^{30} for the Rotated Shock and Rectangular Block Bottom Boundary, 30 Degree "Wedge" Computation

Position	x-Position (<i>cm</i>)	y-Position (<i>cm</i>)
A_{bb}^{30}	0.6829	-0.6828
B_{bb}^{30}	3.0483	-4.7797
C_{bb}^{30}	4.8223	-7.8524
D_{bb}^{30}	7.7555	-0.4329
E_{bb}^{30}	9.2548	-3.0297
F_{bb}^{30}	10.3793	-4.9774

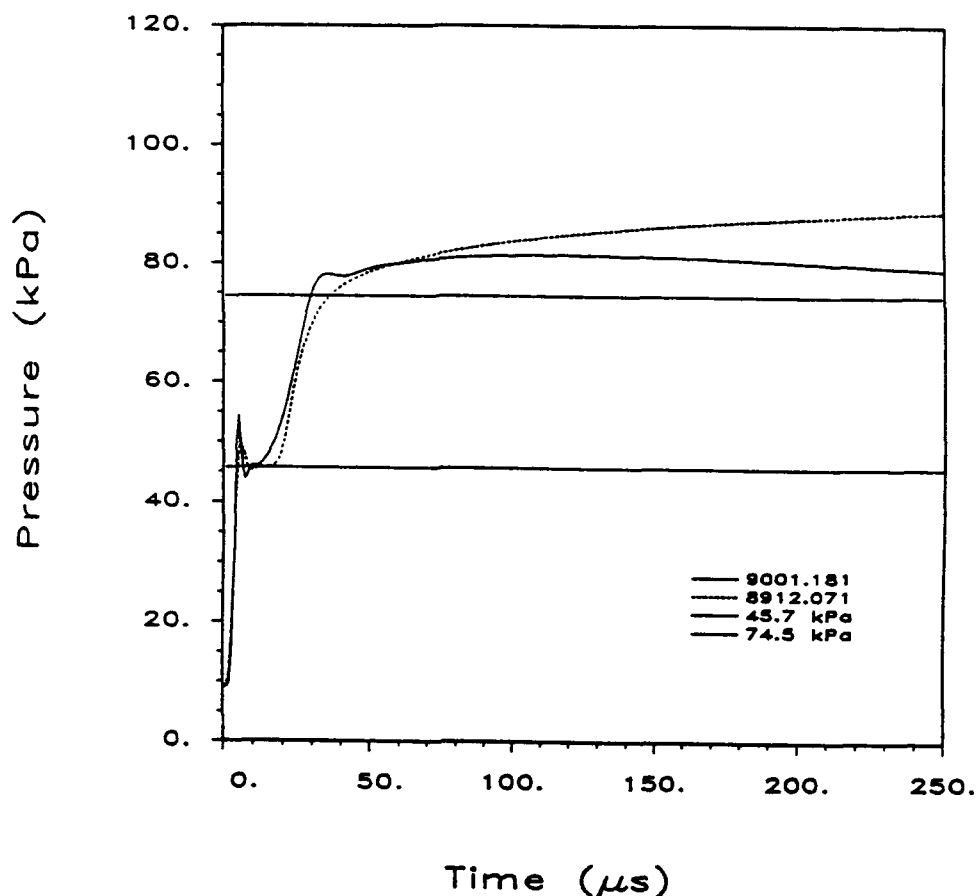


Figure 36. HULL122 Problems 8912.071 and 9001.181, Absolute Pressure at Points A_w^{30} and A_{bb}^{30} , Respectively.

coordinates for points A_{bb}^{30} through F_{bb}^{30} , which are kept the same for all of the computations for a rotated shock striking the bottom surface of a rectangular block to simulate a 30 degree wedge interaction.

Figure 36 shows the comparison between 8912.071 and 9001.181 for points A_w^{30} and A_{bb}^{30} , respectively. There is a clear difference in the reflected shock passage after the incident shock due mostly to the different curvatures of the computed reflected shocks, and a large late time drop in 9001.181 which is due to the different fluid dynamic activity around the leading corner. A careful study of the incident shock pressure rises will also illustrate the greater diffusion in computation 9001.181 because of the nonorthogonal passage of the shock through the grid. Figure 37 for points B_w^{30} and B_{bb}^{30} also shows a different reflected shock passage. Figure 38 shows, as before, only the incident shock passage at points C_w^{30} and C_{bb}^{30} . Except for the incident shock pressure rise time, both computations are identical. Figure 39 shows the passage of the Mach stem at points D_w^{30} and D_{bb}^{30} , with 8912.071 showing a delayed arrival and more elevated early pressure than 9001.181, in a manner very similar to SHARC computation 9002.12 in Figure 23. Figure 40 shows the pressure versus time for points E_w^{30}

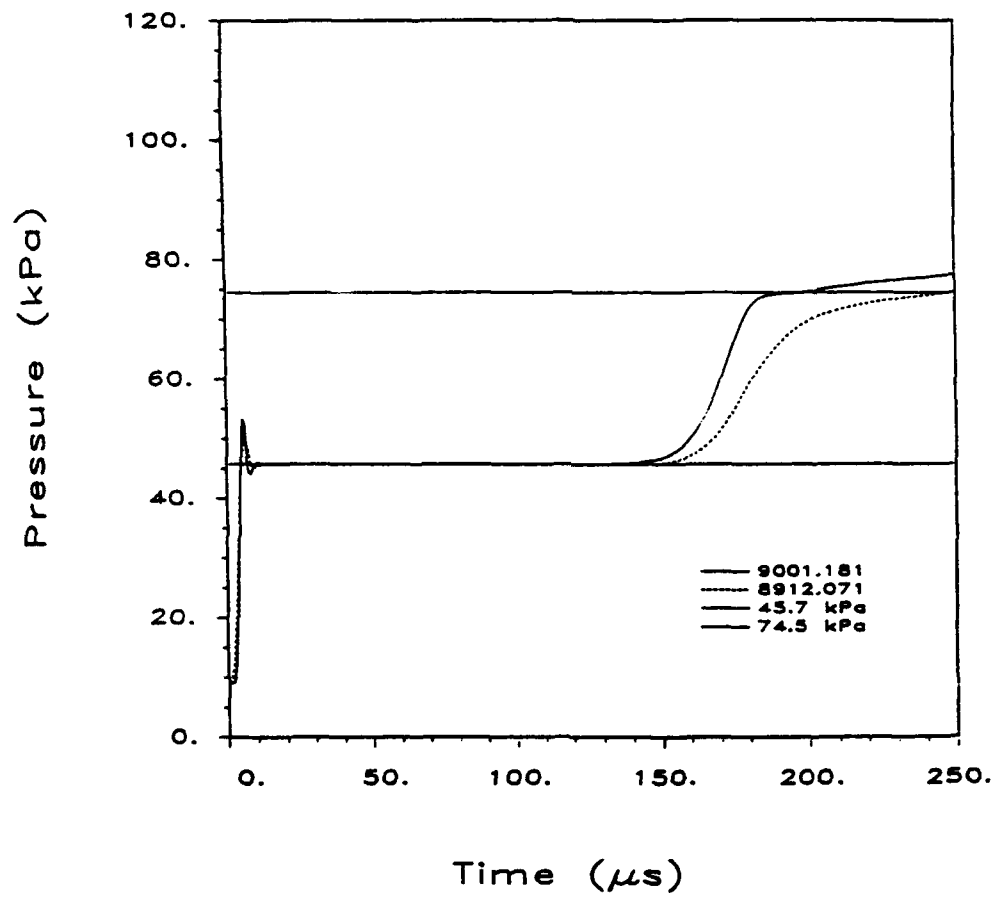


Figure 37. HULL122 Problems 8912.071 and 9001.181, Absolute Pressure at Points B_w^{30} and B_{bb}^{30} , Respectively.

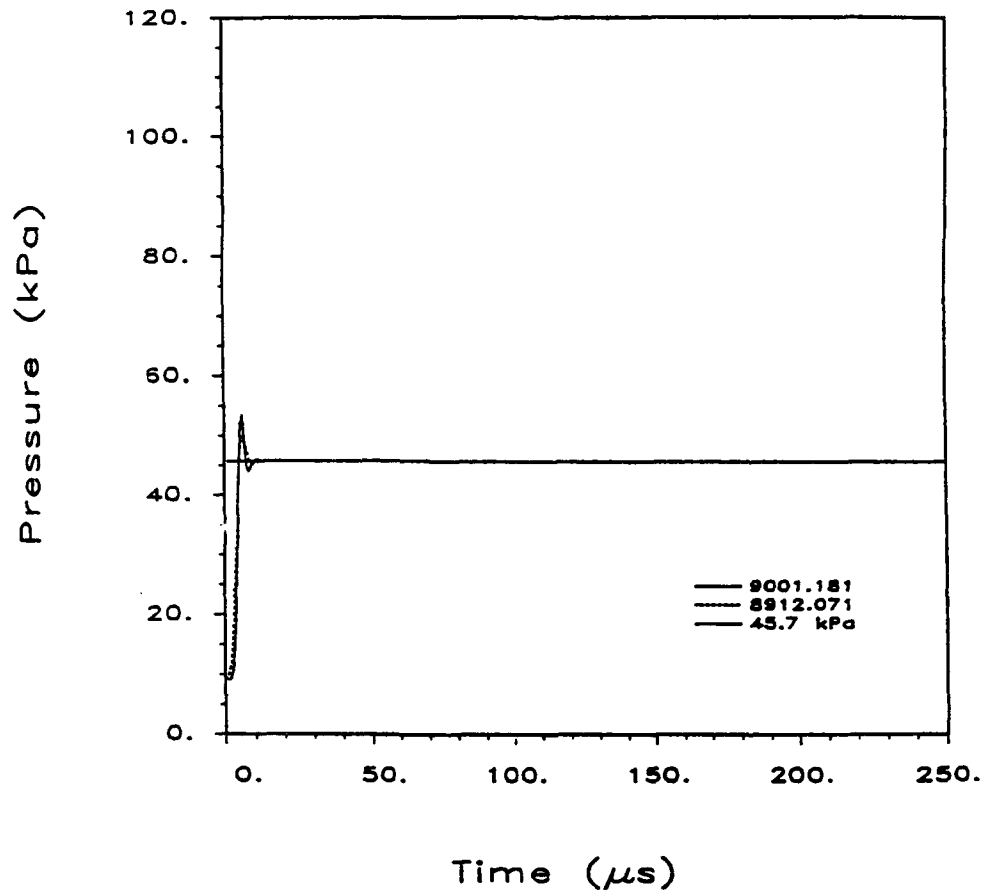


Figure 38. HULL122 Problems 8912.071 and 9001.181, Absolute Pressure at Points C_w^{30} and C_{bb}^{30} , Respectively.

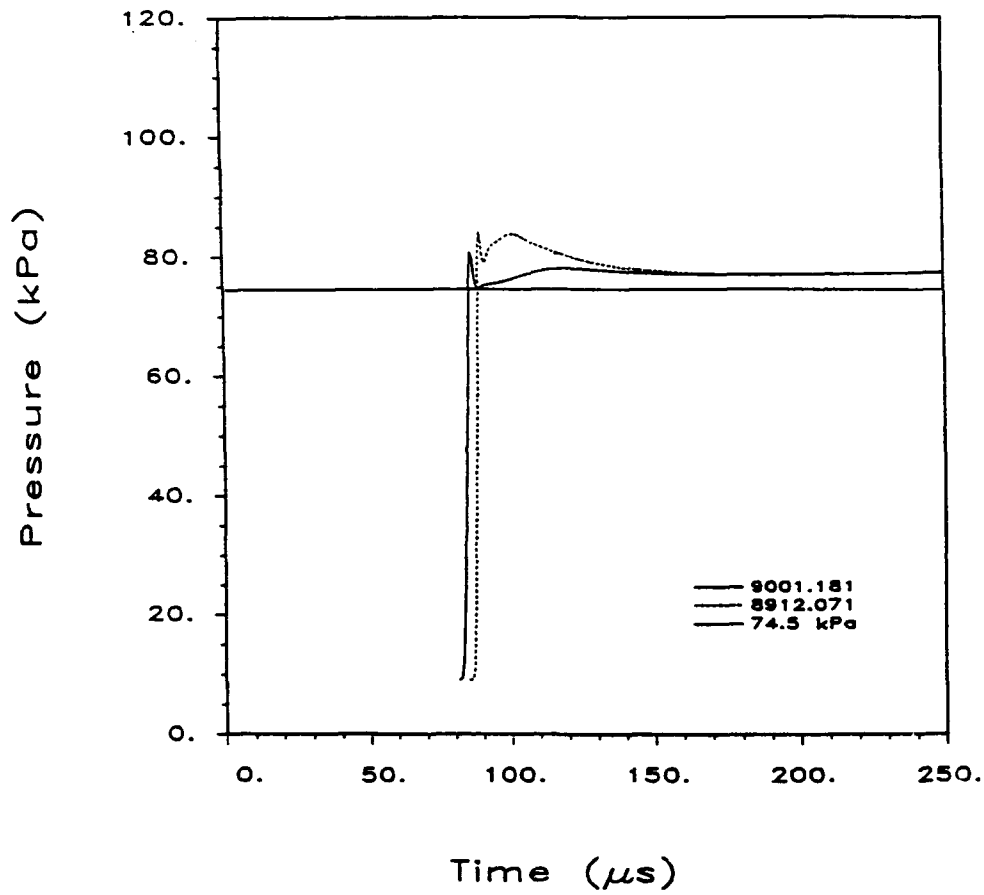


Figure 39. HULL122 Problems 8912.071 and 9001.181, Absolute Pressure at Points D_w^{30} and D_{bb}^{30} , Respectively.

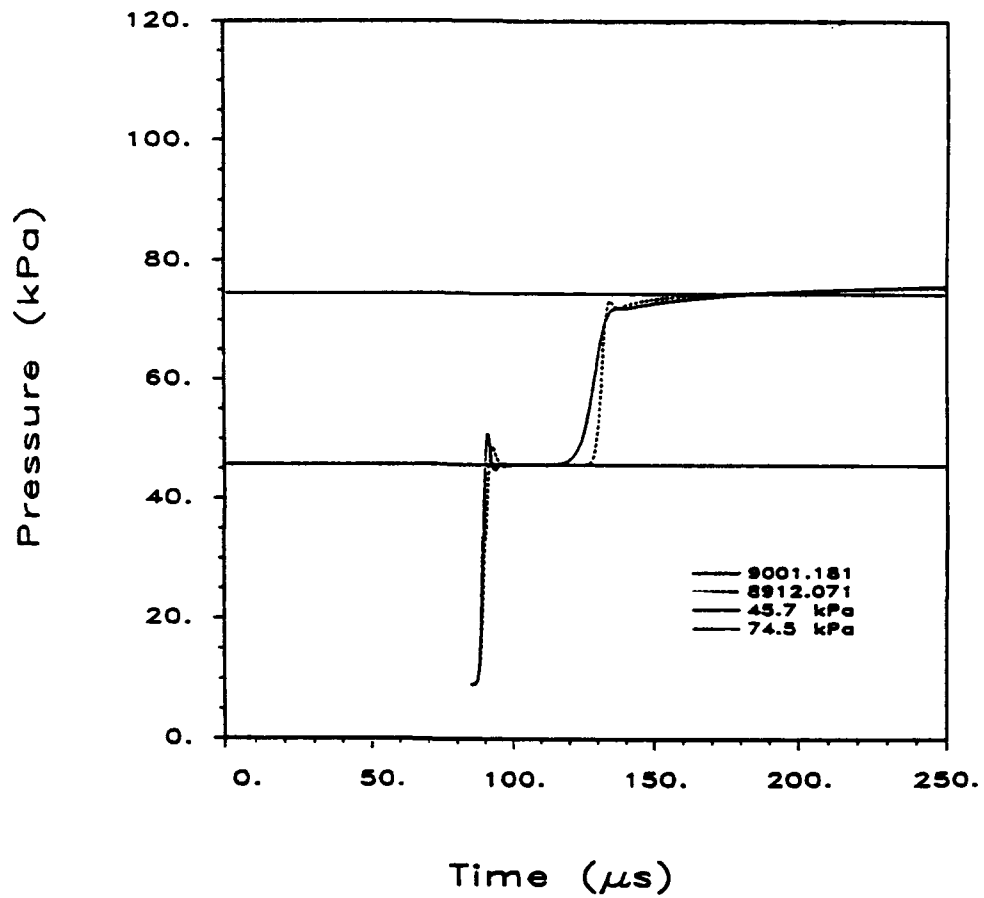


Figure 40. HULL122 Problems 8912.071 and 9001.181, Absolute Pressure at Points E_w^{30} and E_{bb}^{30} , Respectively.

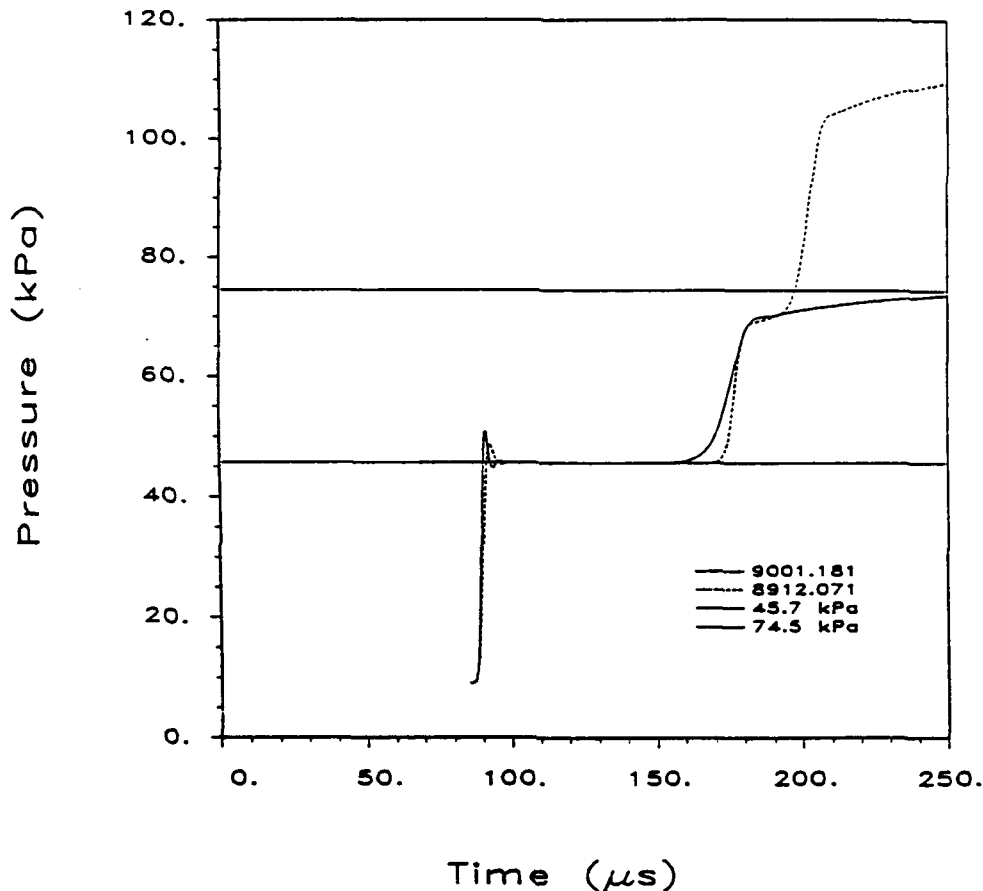


Figure 41. HULL122 Problems 8912.071 and 9001.181, Absolute Pressure at Points F_w^{30} and F_{bb}^{30} , Respectively.

and E_{bb}^{30} , with the same relative features as for points B_w^{30} and B_{bb}^{30} , but less pronounced differences in the reflected shocks. Finally, Figure 41 shows the pressure versus time for points F_w^{30} and F_{bb}^{30} , again with the type of variations in the plots, except that 9001.181 does not have the same reflected shock from a reflective top computational boundary as does 8912.071. Thus, the computation with the orthogonal shock on the stair step wedge and the rotated shock on the rectangular block not only have distinct differences because of the way the wedge surface and shock passage are modeled, they are also different because they are actually solving distinctly different fluid mechanic problems.

e. SHARC Computations 9003.23 and 9003.121, and HULL122 9001.181

The primary purpose of this section is to allow a direct comparison of the use the SHARC code in simulating a rotated shock striking a block, done in SHARC computation 9003.121, with the SHARC computation 9003.23 and the HULL122 computation 9001.181 as discussed above. The SHARC computation 9003.121 used the second order advection

(method = 4) and no artificial viscosity, just as was used for SHARC computation 9003.23. The leading corner (*i.e.*, the lower left corner) of the rigid, nonresponding block was located at point (0.0,0.0). The bottom and left boundaries were defined as continuous input boundaries, where the shocked air having values of density and internal energy, and velocity components corresponding to the incident shock at the desired rotation angle were input as fixed values throughout the simulated computation time. The left boundary was located at $x = -22.0 \text{ cm}$, and the bottom boundary was located at $y = -40.0 \text{ cm}$. The top transmissive (zero gradient) boundary was located at $y = 30.0 \text{ cm}$ and the right transmissive boundary was located at $x = 20.0 \text{ cm}$. For simplicity, all cells were fixed at $\Delta x = 0.1 \text{ cm}$ and $\Delta y = 0.1 \text{ cm}$. Estimates of numerical wave speeds in this computational grid indicated that the left and bottom boundaries were sufficiently far away from the block that no numerical disturbances generated by reflected wave arrivals at those boundaries could return to the points of interest during the desired computational time. Nonetheless, an additional computation, number 9003.29, of this same problem but with the left boundary moved farther out to $x = -24.0 \text{ cm}$ and the bottom boundary farther down to $y = -44.0 \text{ cm}$ was run as a test, with no change in results in the points of interest, thus verifying that 9003.121 was a clean, valid computation.

Figure 42 shows the absolute pressure contours for the shock interaction for SHARC computation 9003.121 with the wedge (rotated shock and block combination) at $t = 50 \mu\text{s}$. As with Figure 34, Figure 42 shows the interaction for a 30 degree wedge on the horizontal bottom boundary of the rectangular block, and the interaction for the 60 degree wedge on the left vertical boundary of the block which will be discussed later. shows the corresponding density contours for the 30 degree wedge side of the block for 9003.121, also at $t = 50 \mu\text{s}$.

The primary difference between HULL122 computation 9001.181 and SHARC computation 9003.121 is that 9001.181 uses the first order donor cell fluxing (method = 2), and 9003.121 uses the second order advection (method = 4) (see Table 3). Figure 44 shows the absolute pressure versus time to $t_f = 300.0 \mu\text{s}$ for point A_{bb}^{30} on the 30 degree wedge side of the block for the two computations, and the results for point A_w^{30} from the smooth wedge computation 9003.23 as a reference case that is the same geometrically as the EMI experiment and STEALTH computation. Computation 9001.181 has a somewhat greater pressure overshoot for the incident shock than does the comparable SHARC computation 9003.121, with both computations giving nearly the same results at later time. Computation 9003.121 does have more high order oscillations after the arrival of the reflected shock, with slightly lower pressure at late time. Both rotated shock computations show evidence of the different reflected shock curvature and possible communication around the leading corner. This can be seen clearly by comparing the results from the reference computation 9003.23, which was for a 30 degree wedge on a reflecting plane.

Figure 45 shows the pressure versus time for the same computations for points B^{30} . Here, the difference in the timing of the arrival of the reflected wave for the true wedge computation 9003.23 for point B_w^{30} is distinctly different (*i.e.*, much later, and with lower pressure) from that for the two rotated shock computations at point A_{bb}^{30} . The SHARC computation 9003.121 shows high order oscillations, but gives a solution that is similar to that for the HULL122 computation 9001.181. Figure 46 shows the pressure versus time for

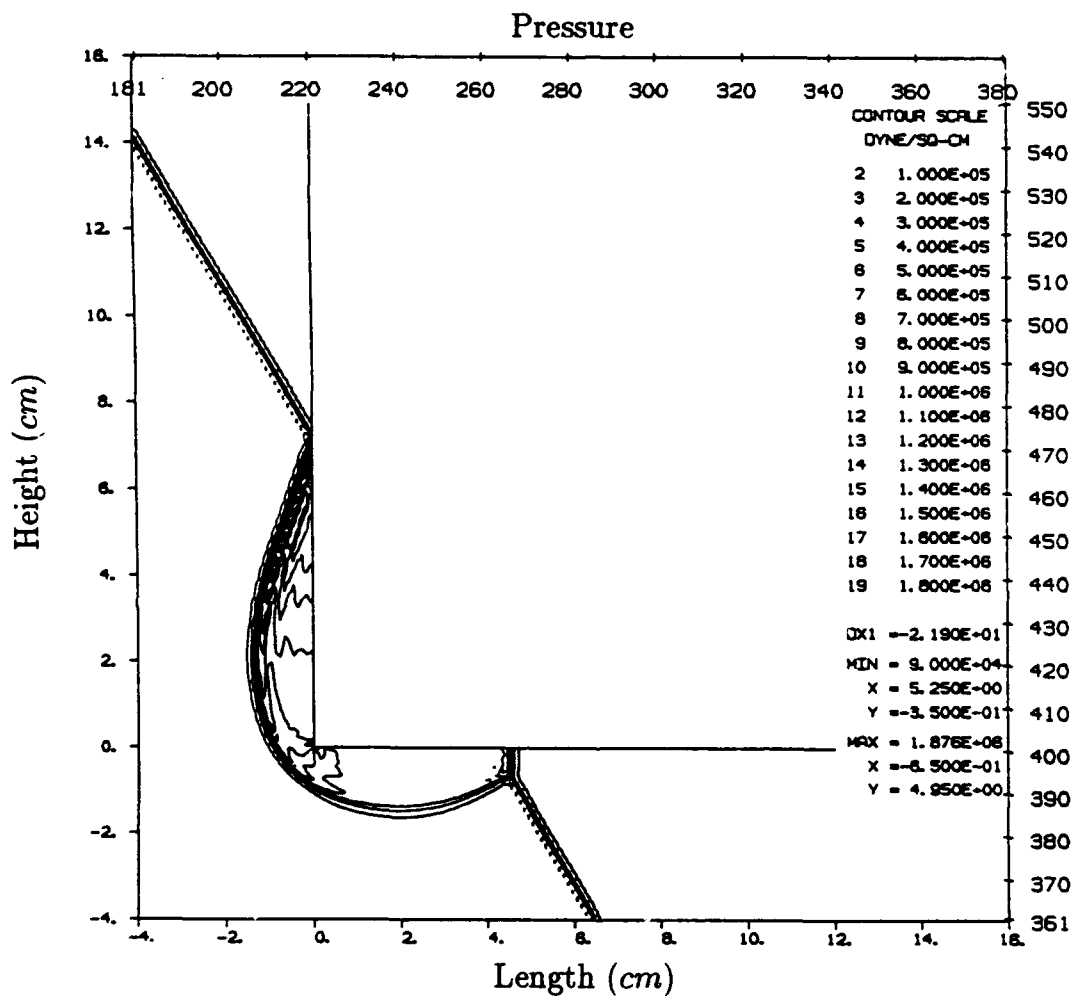


Figure 42. SHARC Problem 9003.121, 30 Degree Smooth Wedge (Bottom) and 60 Degree Smooth Wedge (Left), Absolute Pressure Contours at 50 μ s.

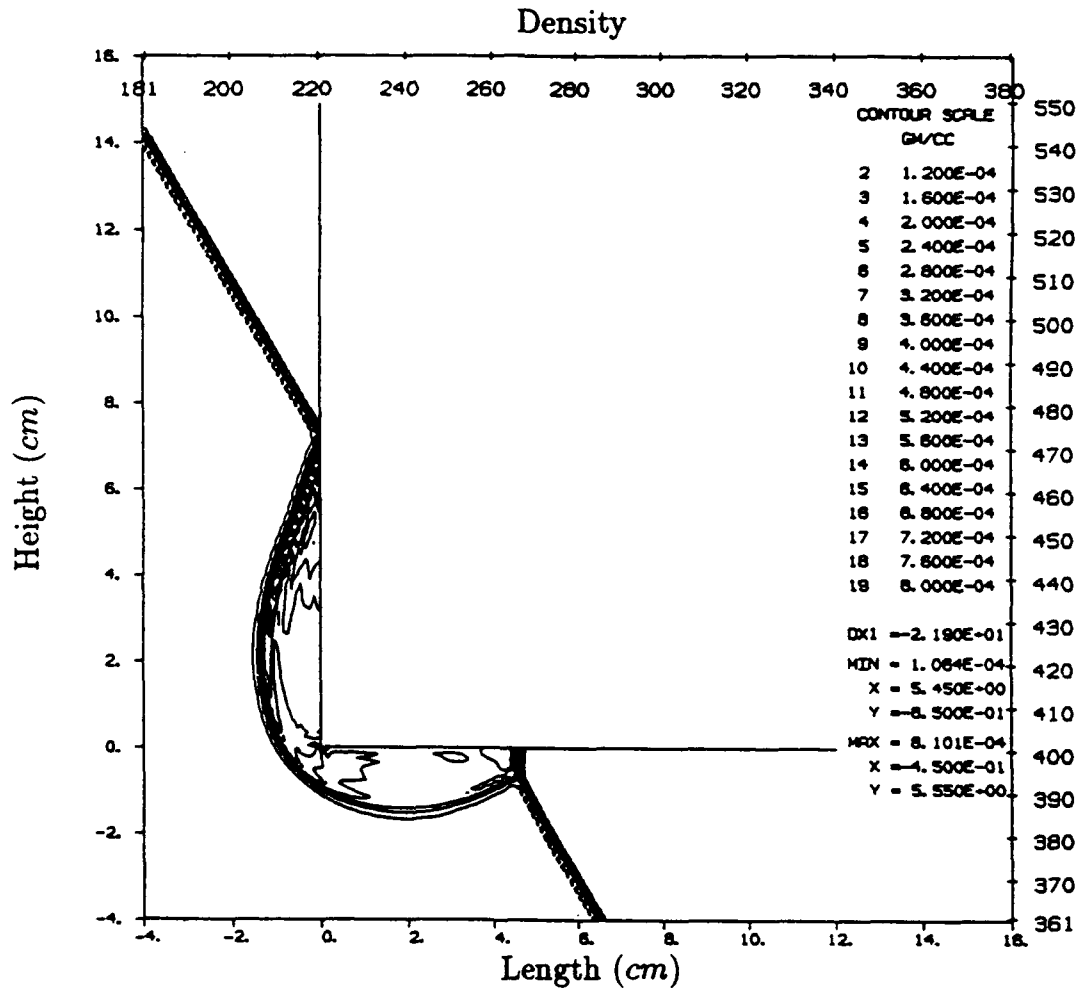


Figure 43. SHARC Problem 9003.121, 30 Degree Smooth Wedge (Bottom) and 60 Degree Smooth Wedge (Left), Density Contours at $50 \mu\text{s}$.

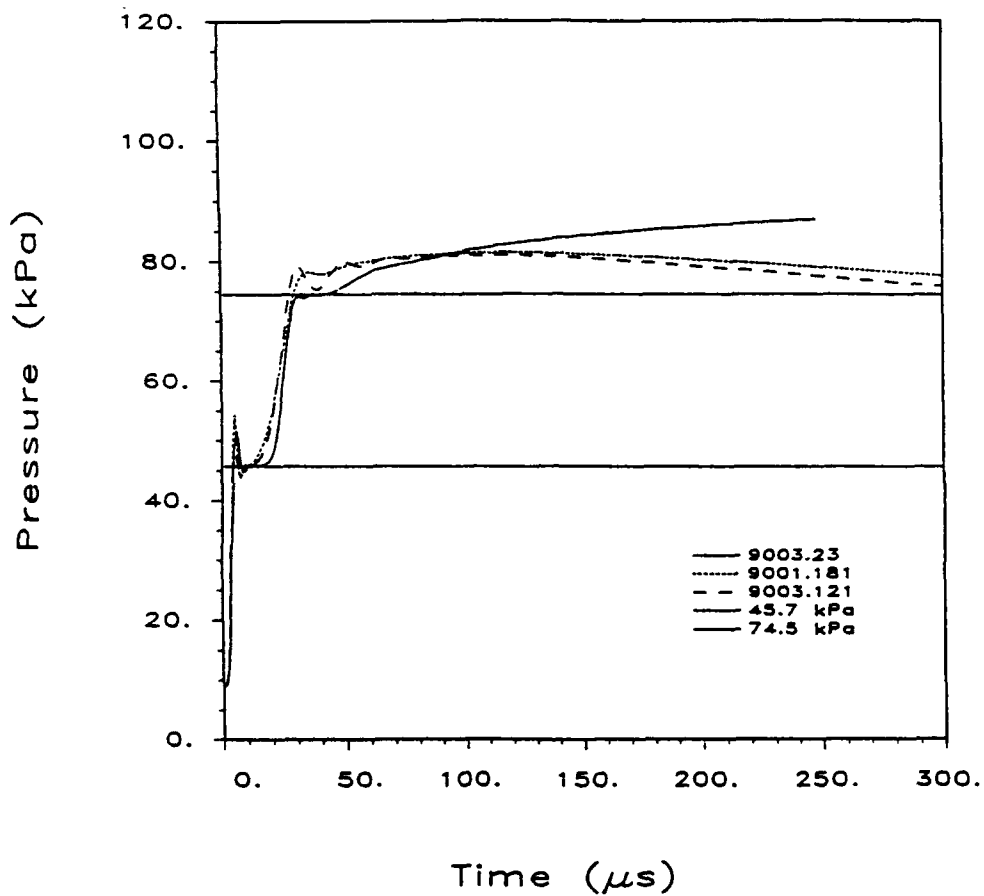


Figure 44. SHARC Problems 9003.23 and 9003.121, and HULL122 Problem 9001.181, Absolute Pressure at Points A_w^{30} and A_{bb}^{30} .

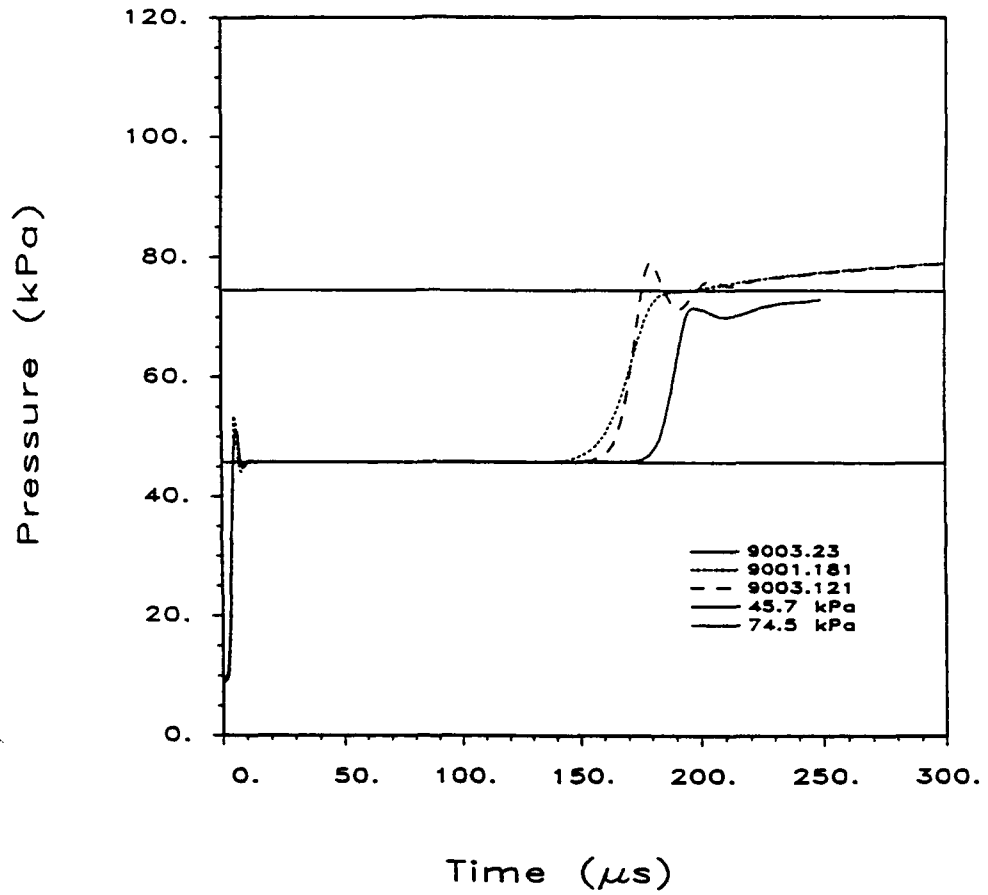


Figure 45. SHARC Problems 9003.23 and 9003.121, and HULL122 Problem 9001.181, Absolute Pressure at Points B_w^{30} and B_{bb}^{30} .

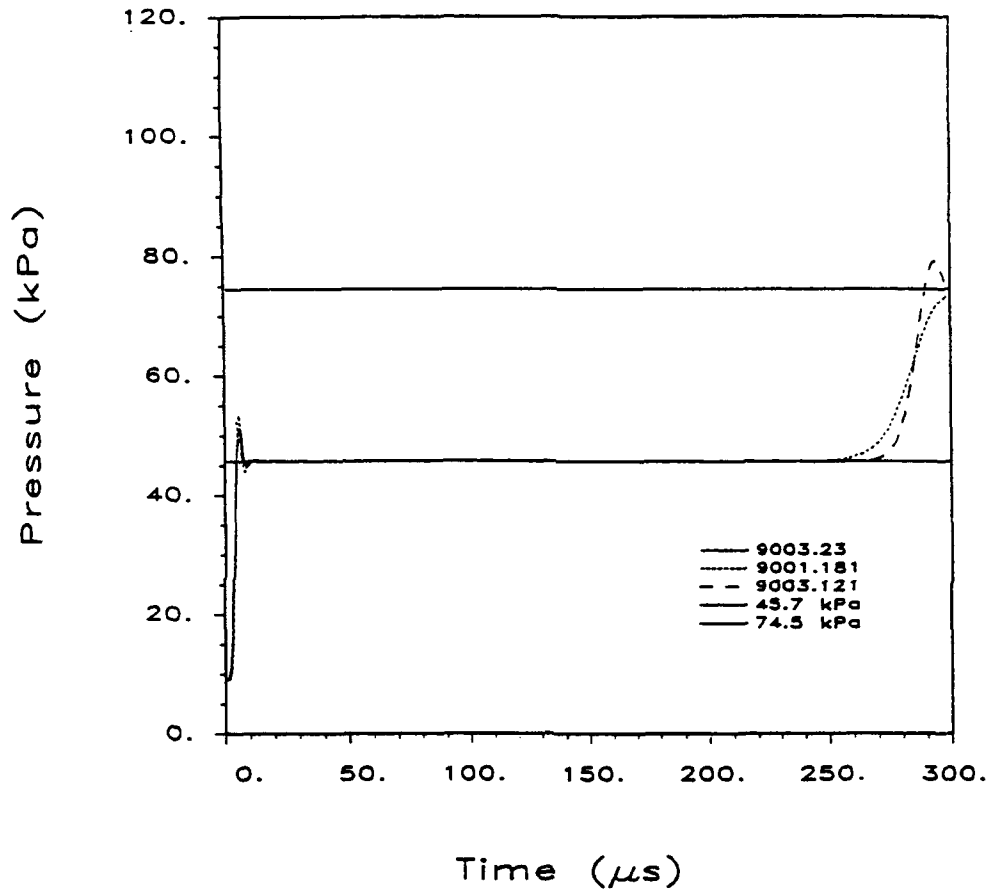


Figure 46. SHARC Problems 9003.23 and 9003.121, and HULL122 Problem 9001.181, Absolute Pressure at Points C_w^{30} and C_{bb}^{30} .

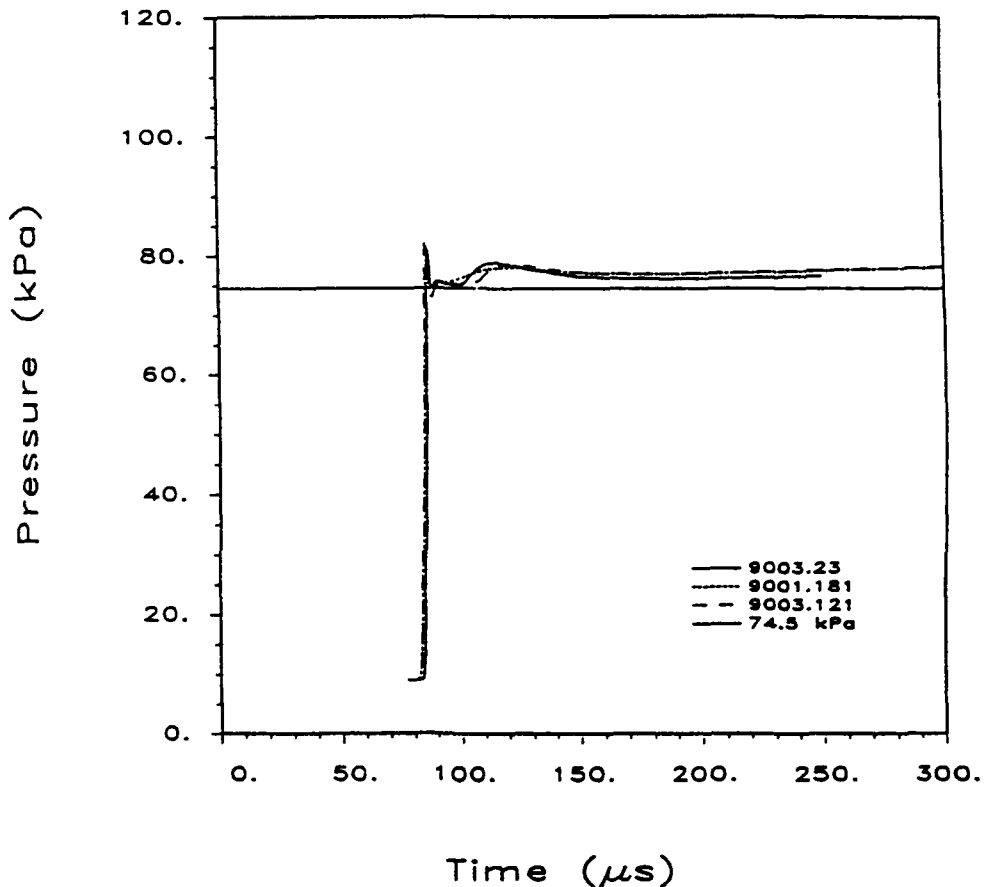


Figure 47. SHARC Problems 9003.23 and 9003.121, and HULL122 Problem 9001.181, Absolute Pressure at Points D_w^{30} and D_{bb}^{30} .

the same computations for points C_w^{30} and C_{bb}^{30} . Except for the incident shock rise, there is essentially no difference in the computations. Point C_w^{30} does not show the reflected shock arrival simply because it is only plotted to 250.0 μ s. Figure 47 shows the pressure versus time for points D_w^{30} and D_{bb}^{30} . As noted before, point D_w^{30} experiences only the passage of the Mach stem. Figure 47 shows a slightly later arrival of the Mach stem for computation 9003.23, the reference wedge computation, than for either computation for a rotated shock and block. This is additional evidence of different rarefaction wave generation at the leading edge. Computation 9003.23 also shows the lowest late time pressure, but by a relatively small amount. Figure 48 shows the pressure versus time for points E_w^{30} and E_{bb}^{30} . Except for a slight delay in the incident and reflected shock arrivals for 9003.23, the computations are essentially identical. The same is true for Figure 49, which shows the pressure versus time for points F_w^{30} and F_{bb}^{30} . Here, neither computation for the rotated shock and island block combination has a third pressure rise. That pressure rise in 9003.23 was caused by the reflected shock from its reflective top boundary.

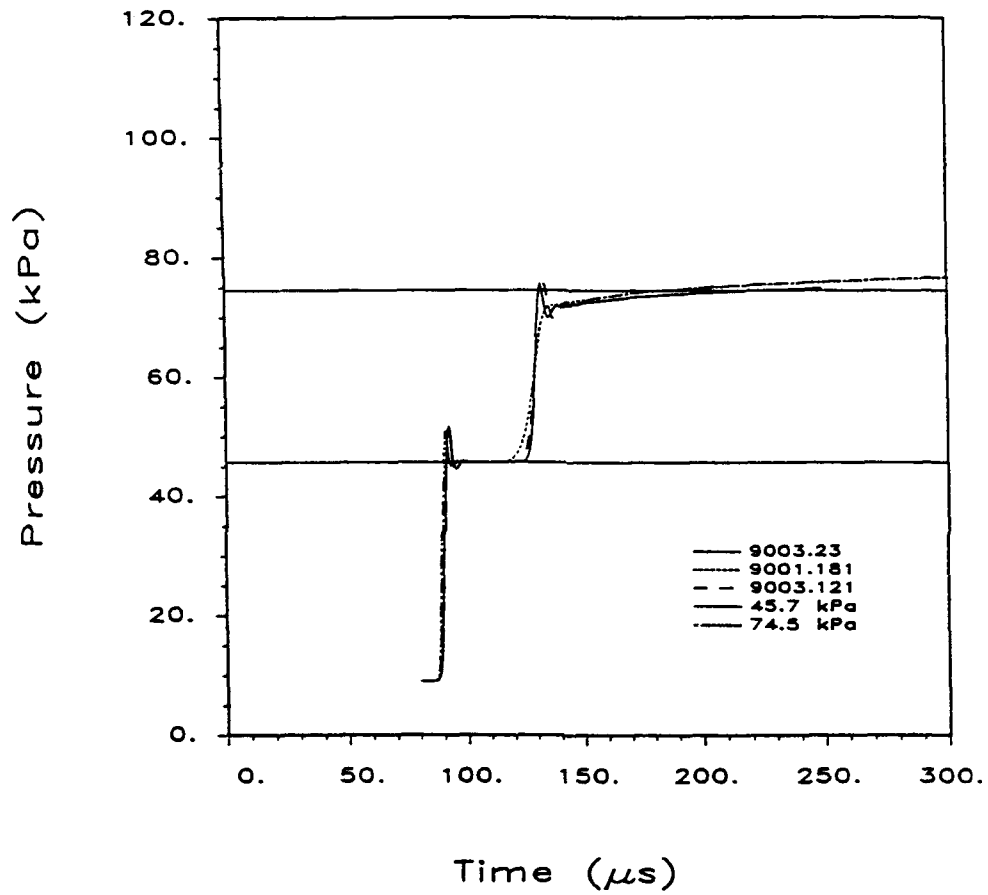


Figure 48. SHARC Problems 9003.23 and 9003.121, and HULL122 Problem 9001.181, Absolute Pressure at Points E_w^{30} and E_{bb}^{30} .

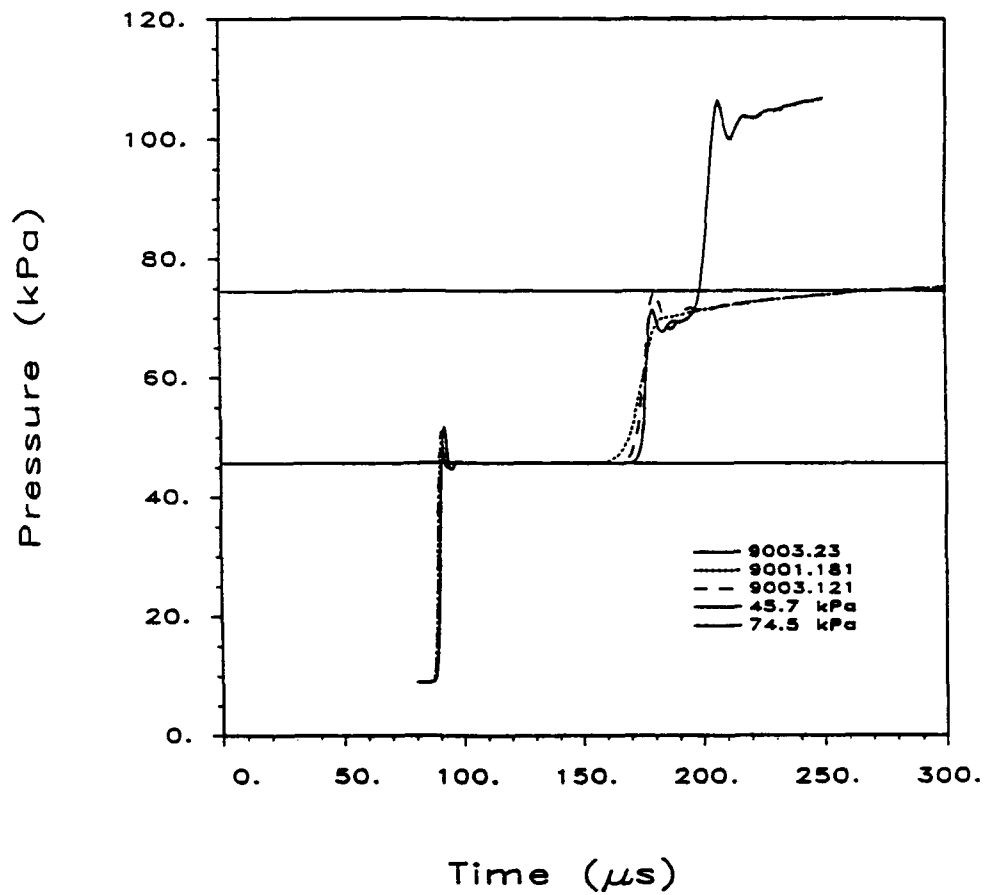


Figure 49. SHARC Problems 9003.23 and 9003.121, and HULL122 Problem 9001.181, Absolute Pressure at Points F_w^{30} and F_{bb}^{30} .

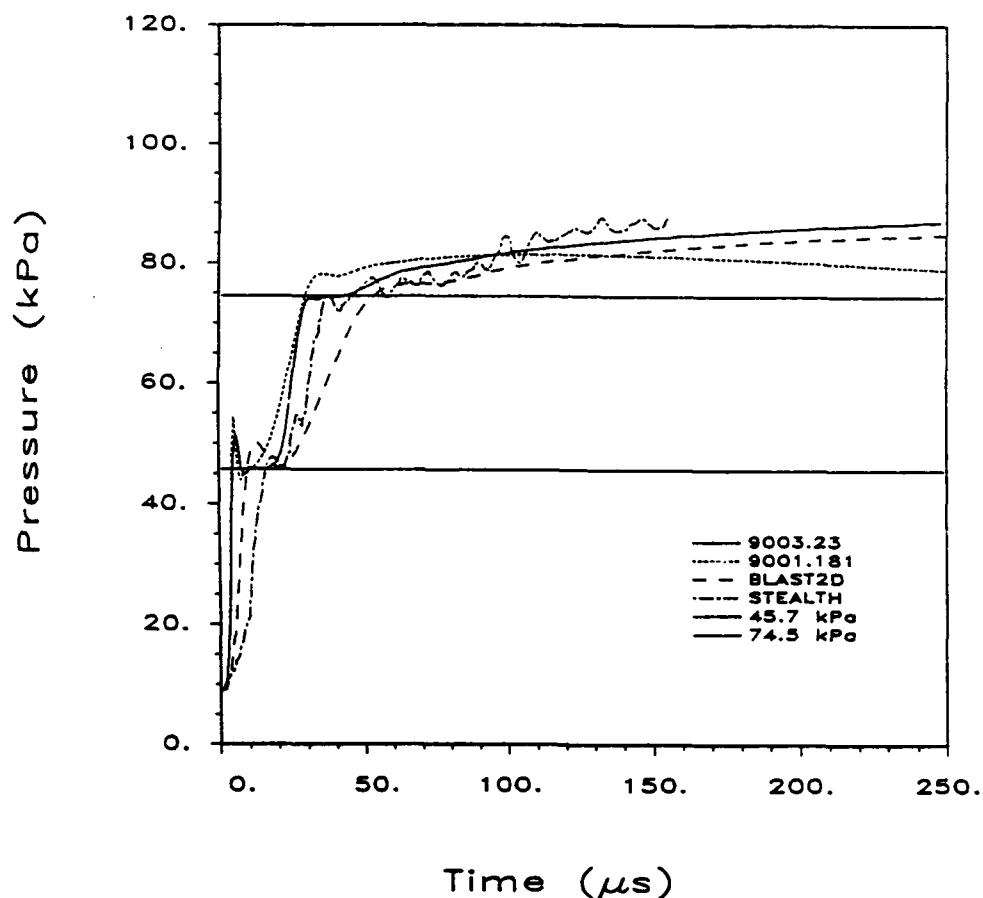


Figure 50. SHARC 9003.23, HULL122 9001.181, EMI STEALTH, and the BLAST2D Computations, Absolute Pressure at Points A_w^{30} , A_{bb}^{30} , and A.

f. SHARC 9003.23, HULL122 9001.181, BLAST2D, and EMI STEALTH Computations

This section compares the pressure versus time for points A_w^{30} through F_w^{30} and A_{bb}^{30} through F_{bb}^{30} for the high resolution computations SHARC 9003.23 and HULL122 9001.181, which were discussed above, with points A through F for the low resolution EMI STEALTH computation,^{2,4} and a matching low resolution BLAST2D computation.¹⁰ Additional computations, including comparable high resolution computations, were performed by Ms. Hisley, and will be formally reported.¹¹ The BLAST2D computation uses Roe's approximate Riemann solver¹³ with a technique called Total Variation Diminishing¹⁴ (TVD) to control the generation of artificial new minima and maxima. Figure 50 shows the pressure versus time for points A_w^{30} , A_{bb}^{30} , and A for the four computations. Because computations 9003.23 and 9001.181 have already been discussed, the discussion here will be focused on the STEALTH and BLAST2D computations, with the caution that in addition to the fundamental differences in the codes themselves, the x direction grid resolution for 9003.23 and 9001.181 was

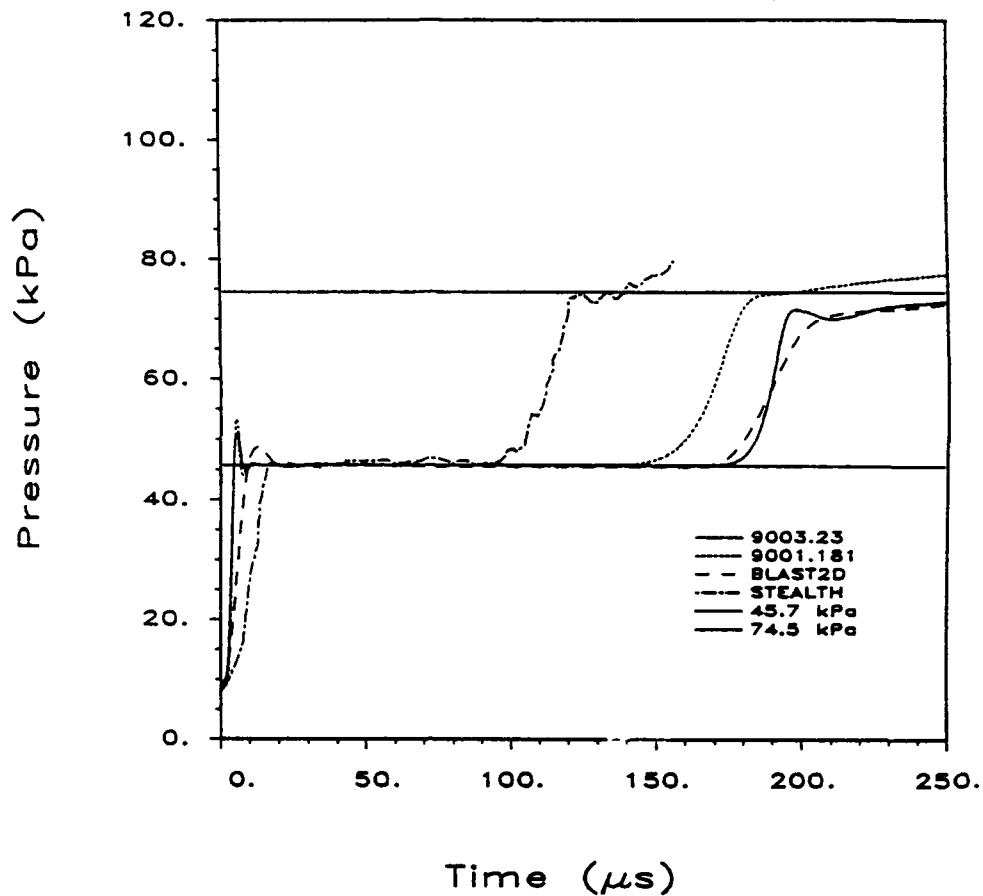


Figure 51. SHARC 9003.23, HULL122 9001.181, EMI STEALTH, and the BLAST2D Computations, Absolute Pressure at Points B_w^{30} , B_{bb}^{30} , and B .

$\Delta x = 0.10 \text{ cm}$, while the STEALTH and BLAST2D computations used $\Delta x = 0.25 \text{ cm}$. Both the STEALTH and BLAST2D computations have relatively smeared incident and reflected shocks, primarily due to the lower resolution. The overshoot in the computation of the incident shock for SHARC computation 9003.23 is to 51.3 kPa , 12.3 percent above the correct experimental value of 45.7 kPa ; to 54.1 kPa or 18.4 percent for HULL122 computation 9001.181; to 49.8 kPa or 9.0 percent for BLAST2D; and to 47.7 kPa or 4.4 percent for the STEALTH computation. The STEALTH, BLAST2D, and SHARC 9003.23 computations all show similar late time trends in pressure, because all three simulated a 30 degree wedge on a reflecting plane, while the late time drop for the HULL122 computation 9001.181 is due to the different fluid dynamic effects initiated at the corner of the rectangular block as it is struck by the rotated shock. The STEALTH computation was ended at approximately $153 \mu\text{s}$.

Figure 51 shows the pressure versus time for the four computations at points B_w^{30} , B_{bb}^{30} , and B . This also illustrates an unresolved discrepancy in the reported position of point B for the EMI STEALTH computation, which shows a much earlier reflected shock arrival

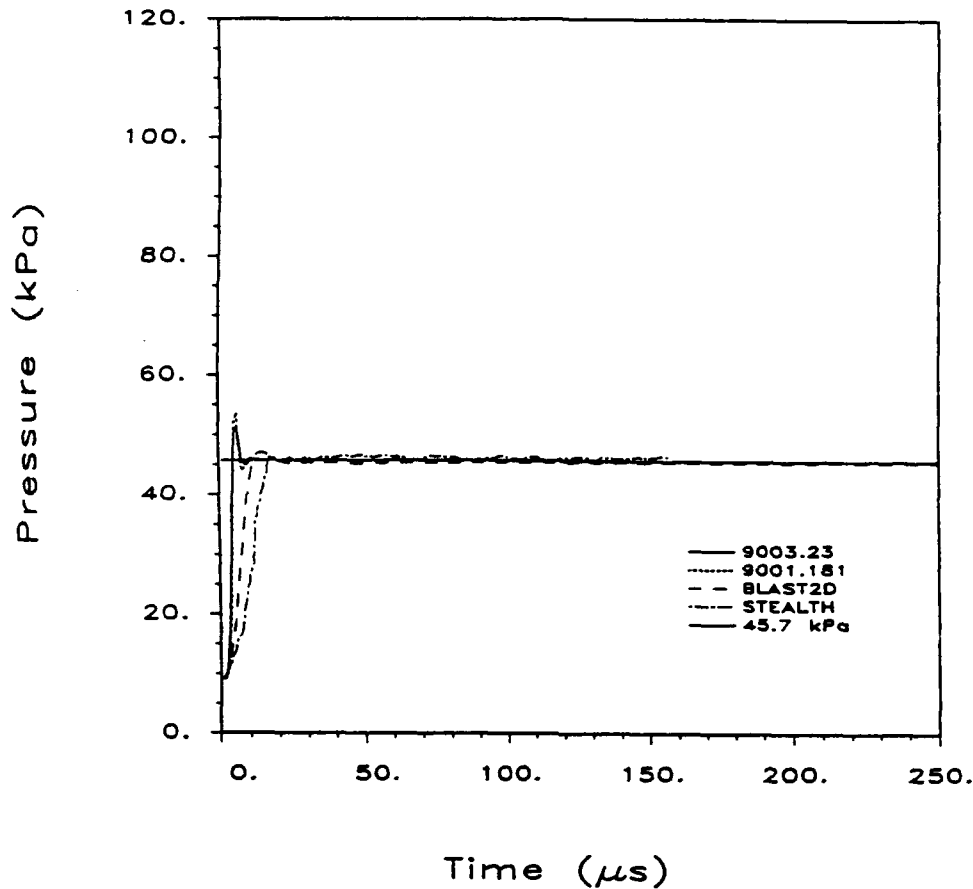


Figure 52. SHARC 9003.23, HULL122 9001.181, EMI STEALTH, and the BLAST2D Computations, Absolute Pressure at Points C_w^{30} , C_{bb}^{30} , and C .

than the other computations. Apparently, position B was either lower in the STEALTH computation than reported, or some unintended time shift was incorporated in the EMI plot for position B . Except for the additional diffusion in the BLAST2D results, the agreement with the higher resolution computation 9003.23 is good. The reflected shock for 9001.181 arrives early because of the corner effects noted before. Figure 52 shows the pressures for the four computations at points C_w^{30} , C_{bb}^{30} , and C with little to note as unusual except that both the BLAST2D and STEALTH computations show considerably less overshoot than for point A_w^{30} . This may be related to the relative proximities to the computational bottom boundaries, but that issue has not been rigorously explored as of this time. All computations show excellent late time agreement with the experimentally measured incident shock strength represented by the straight line.

Figure 53 shows the absolute pressure versus time for the computations at points D_w^{30} , D_{bb}^{30} , and D , which experience only the passage of the Mach stem, and later the expansion wave from the leading edge. Computations 9003.23 and 9001.181 show nearly identical overshoots to 81.3 kPa, 9.1 percent above the reference value of 74.5 kPa; BLAST2D shows

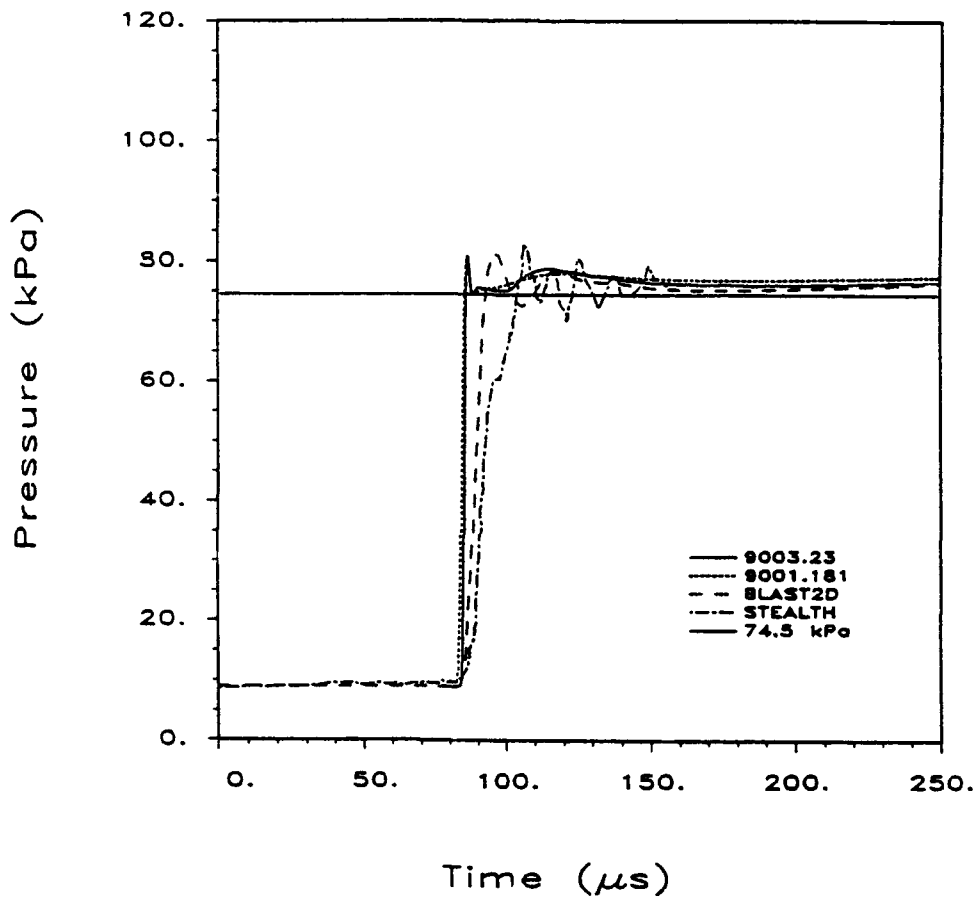


Figure 53. SHARC 9003.23, HULL122 9001.181, EMI STEALTH, and the BLAST2D Computations, Absolute Pressure at Points D_w^{30} , D_{bb}^{30} , and D .

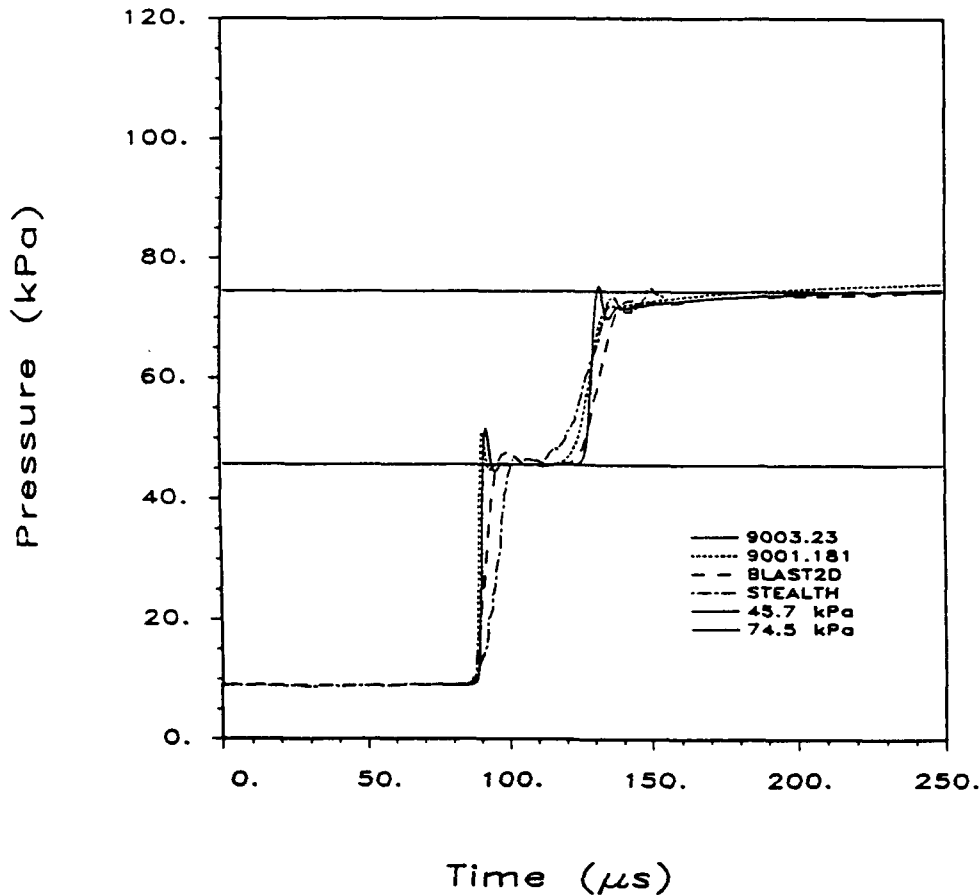


Figure 54. SHARC 9003.23, HULL122 9001.181, EMI STEALTH, and the BLAST2D Computations, Absolute Pressure at Points E_w^{30} , E_{bb}^{30} , and E .

an overshoot of 9.0 percent to 81.2 *kPa*; and the STEALTH computation an overshoot of 11.5 percent to 83.1 *kPa*, much delayed in time. The computations are similar at late time, with 9001.181 having the highest pressure by a small margin.

Figure 54 shows the pressure versus time for the computations at points E_w^{30} , E_{bb}^{30} , and E , which first experience the passage of the incident shock, and then the reflected shock. The computations are all similar, except for the diffusion in the low resolution BLAST2D and STEALTH computations. The computations all show some level of overshoot in the simulation of the incident shock absolute pressure of 45.7 *kPa*. Computation 9003.23 shows the greatest overshoot at approximately 13.8 percent, followed by 9001.181 at 11.2 percent, BLAST2D at 3.9 percent, and STEALTH at 2.8 percent. Figure 55 shows the pressure versus time for the computations at points F_w^{30} , F_{bb}^{30} , and F , which, like points E^{30} in Figure 54, first experience the incident shock, and then the reflected shock. The trends seen for points F^{30} are similar to those already discussed for points E^{30} , except for the final reflected wave from the top boundary.

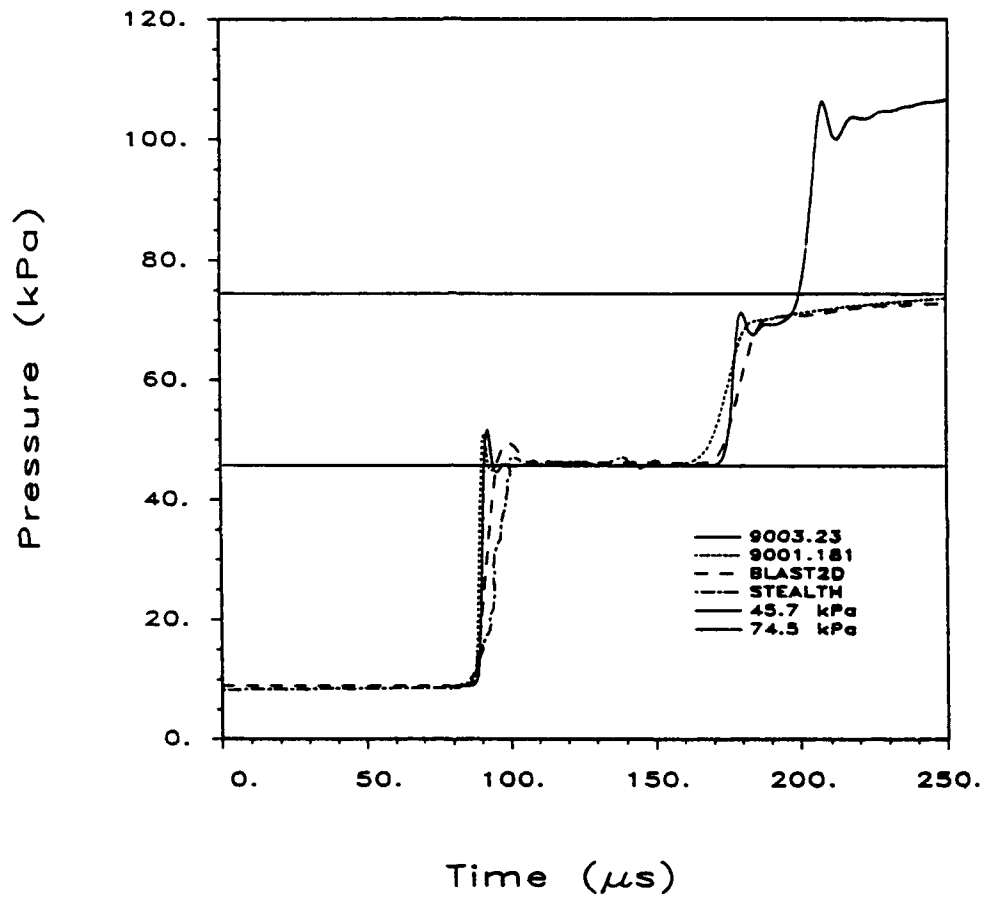


Figure 55. SHARC 9003.23, HULL122 9001.181, EMI STEALTH, and the BLAST2D Computations, Absolute Pressure at Points F_w^{30} , F_{bb}^{30} , and F .

g. SHARC 9003.23, 9003.30, and 9003.121 Computations

Another method that has been used to computationally simulate Mach reflection is to strike a reflecting ground plane with a rotated shock, as shown in Figure 15. SHARC computation 9003.30 was run with a continuous strip of island cells along the top boundary, simulating an inverted reflecting ground plane. The air processed by the $M_I = 2.12$ incident shock, angled at 60 degrees to the horizontal, is continuously fed into the computational grid through transmissive bottom and left boundaries. The thin strip of island cells was placed along the top boundary to more clearly delineate the location of the reflecting surface. The bottom surface of the strip of island cells is defined as $y = 0.0$, with a somewhat arbitrarily located point near the center of that bottom surface defined as $x = 0.0$. The computation was started with the shock intersecting the island strip at point $(-1.1547, 0.0)$, so that the same initial normal standoff from a $(0.0, 0.0)$ point was used for 9003.30 as was used for all other computations. This meant that a continuous oblique interaction of the shocked air with the surface at $x \leq -1.1547$ occurred immediately at the start of the computation. The grid resolution at the top boundary is $\Delta x = \Delta y = 0.10$ cm. Figure 56 shows pressure contours for 9003.30 at 50 μ s. The incident shock **I** is the leading set of contours moving upward and to the right, the Mach stem **M** is the shock moving to the right and perpendicular to the top boundary, and the reflected shock **R** is the curved shock moving downward and to the right. Note that the reflected shock becomes nearly planar at increasing distance from the triple point. Figure 57 shows density contours for 9003.30 at 50 μ s. The locations of points A_{pt}^{30} through F_{pt}^{30} are shown in Table 5. The subscript "pt" stands for "planar top" to indicate

Table 5. BRL Points A_{pt}^{30} - F_{pt}^{30} for the Rotated Shock and Infinite Top Reflective Boundary, 30 Degree "Wedge" Computation

Position	x-Position (cm)	y-Position (cm)
A_{pt}^{30}	0.6829	-0.6828
B_{pt}^{30}	3.0483	-4.7797
C_{pt}^{30}	4.8223	-7.8524
D_{pt}^{30}	7.7563	-0.4324
E_{pt}^{30}	9.2556	-3.0292
F_{pt}^{30}	10.3801	-4.9769

that the perfectly reflective strip of island cells along the top boundary is used to simulate the wedge surface.

As indicated earlier, while this type of interaction also produces the various types of Mach reflection configurations if the shock strengths and angles are within their respective bounds, analysis of flow parameters at comparable points in other configurations is required to make definitive judgments on the fidelity of the simulation. The discussion below compares the pressure versus time for points A_w^{30} through F_w^{30} (orthogonal shock and 30 degree wedge on

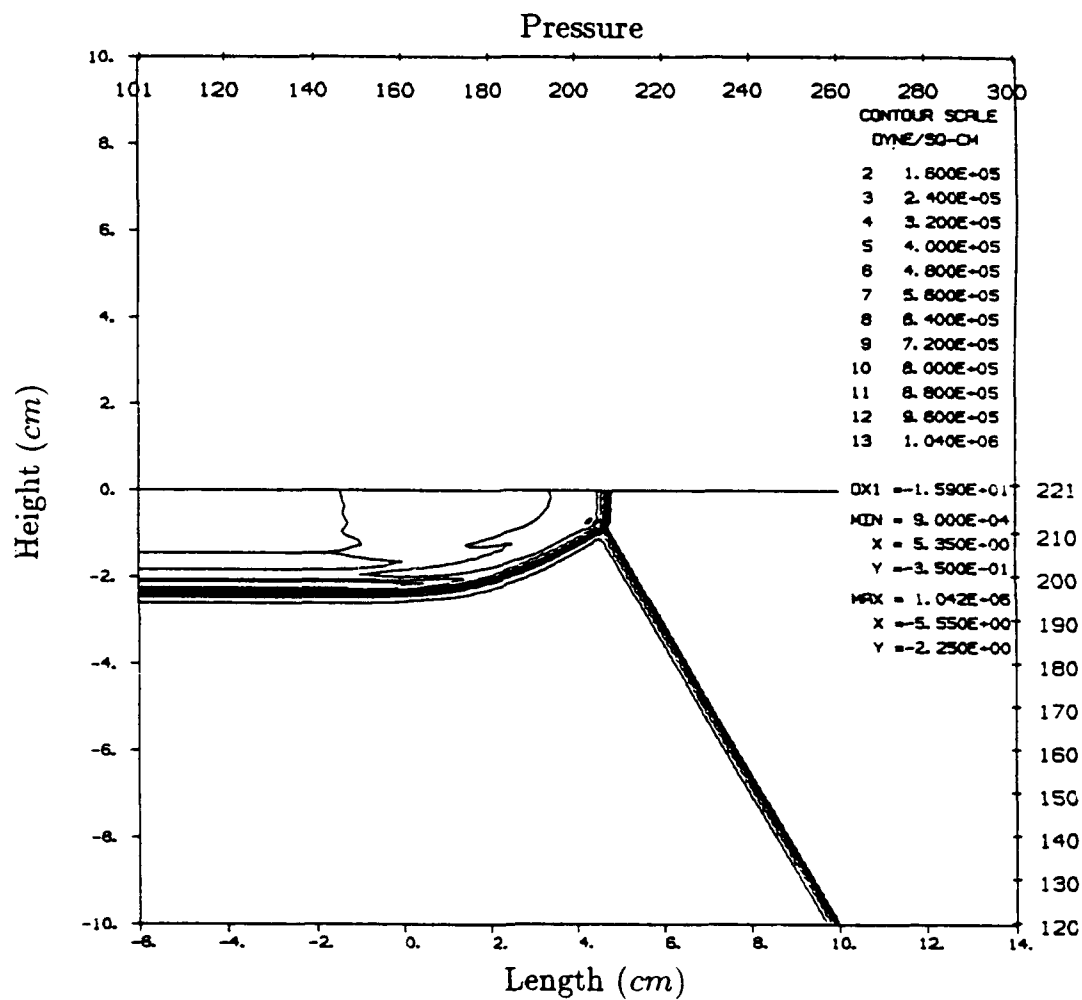


Figure 56. SHARC Problem 9003.30, 30 Degree Smooth "Wedge," (Rotated Shock and Infinite Plane), Pressure Contours at 50 μ s.

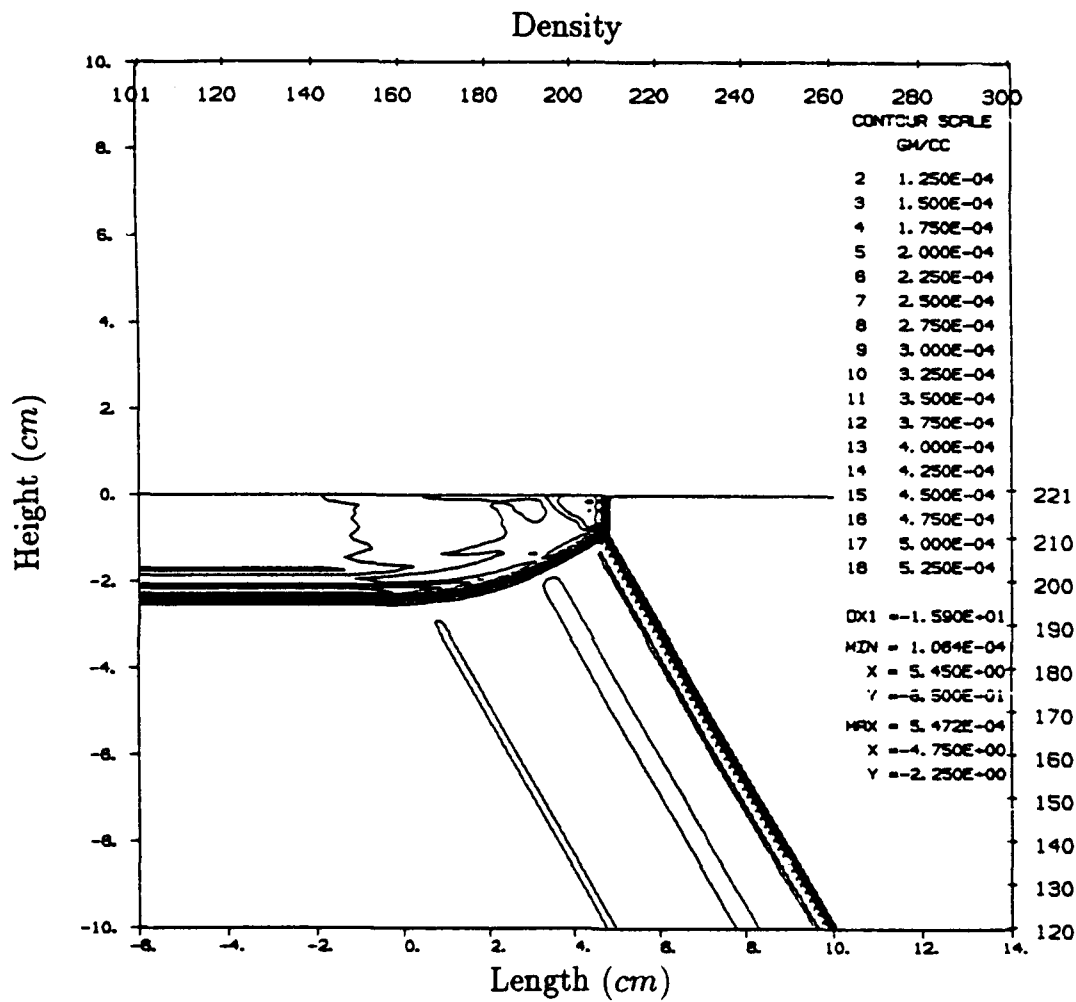


Figure 57. SHARC Problem 9003.30, 30 Degree Smooth "Wedge," (Rotated Shock and Infinite Plane), Density Contours at 50 μ s.

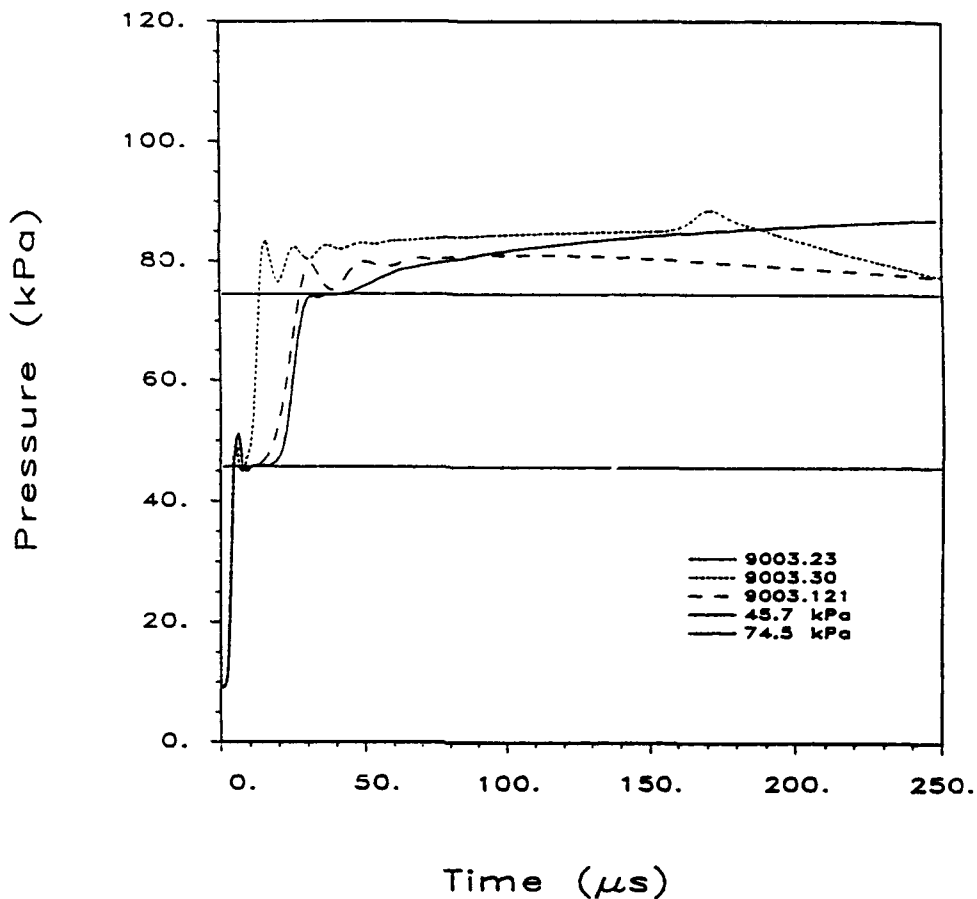


Figure 58. SHARC Computations 9003.23, 9003.30, and 9003.121, Absolute Pressure at Points A_w^{30} , A_{pt}^{30} , and A_{bb}^{30} , Respectively.

a reflecting plane), A_{bb}^{30} through F_{bb}^{30} (rotated shock on a rectangular block), and A_{pt}^{30} through F_{pt}^{30} (rotated shock on an infinite reflecting plane). As before, the points A_{pt}^{30} through F_{pt}^{30} were located at the same normal distances from both the incident shock wave and the "wedge" surface as were their A_w^{30} through F_w^{30} counterparts. Figure 58 shows the pressure versus time for points A_w^{30} , A_{pt}^{30} , and A_{bb}^{30} for the three computations. Because computations 9003.23 and 9003.121 have already been discussed in some detail, only the variations of 9003.30 with respect to those computations will be discussed here. The incident shock arrival and rise times are essentially the same for all three points, but 9003.30 clearly shows a much stronger reflected shock arriving at a distinctly earlier time. This is due to the simultaneous, infinitely long oblique interaction of the air behind the incident shock air with the top reflecting plane at $x \leq -1.1547$, which sends a strong compression wave in the positive x direction. The late time drop in the curve for 9003.30 is most likely a boundary effect of some sort that is not of interest here.

Figure 59 shows the pressure versus time for points B_w^{30} , B_{pt}^{30} , and B_{bb}^{30} . The nearly identical incident shock histories are again evident. Computation 9003.30 shows a very

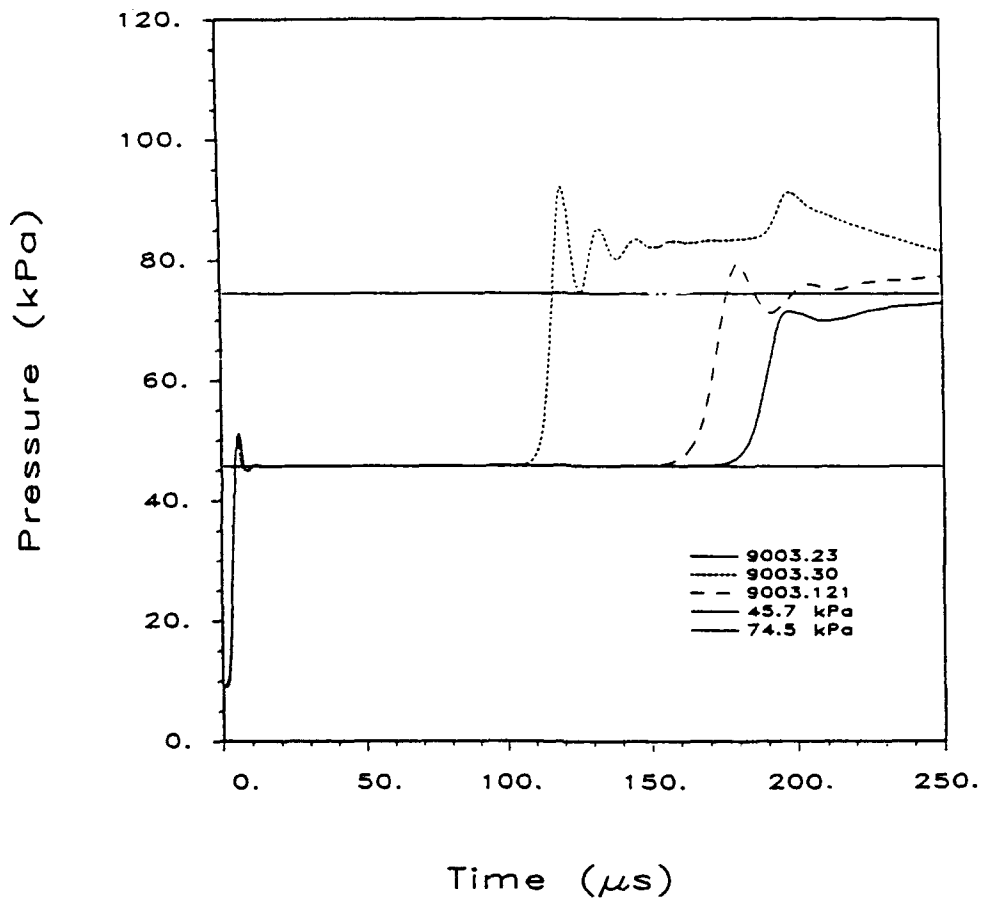


Figure 59. SHARC Computations 9003.23, 9003.30, and 9003.121, Absolute Pressure at Points B_w^{30} , B_{pt}^{30} , and B_{bb}^{30} , Respectively.

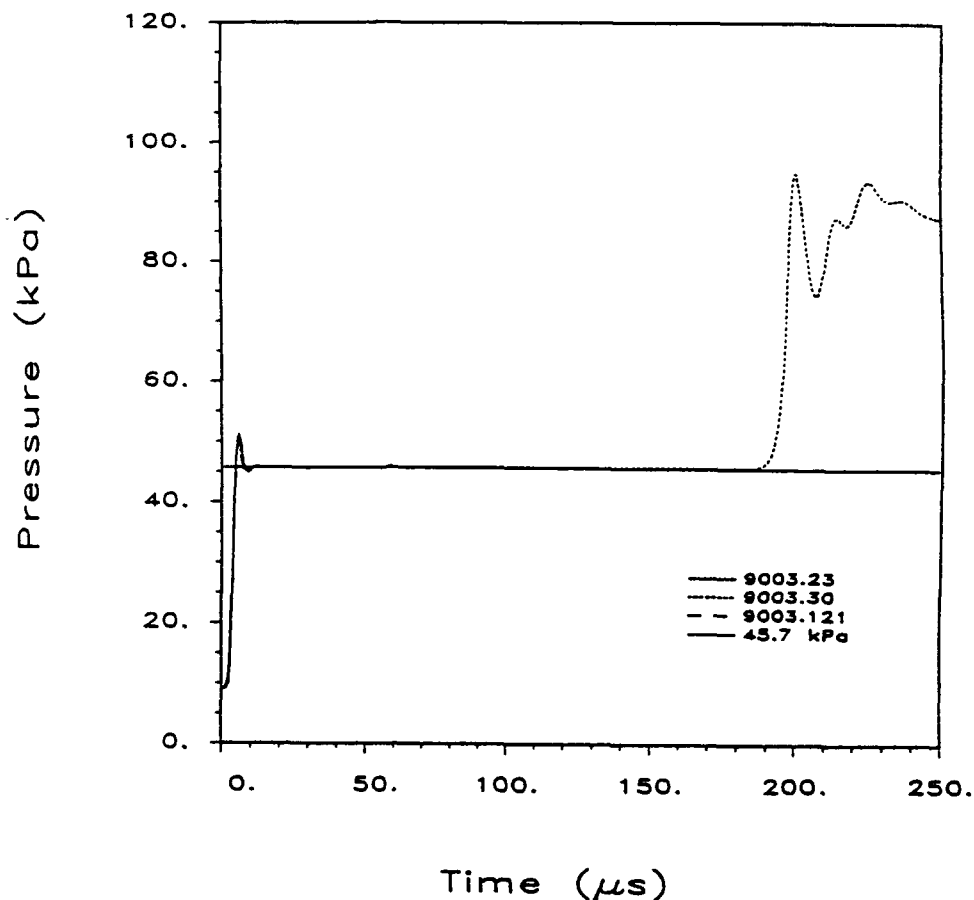


Figure 60. SHARC Computations 9003.23, 9003.30, and 9003.121, Absolute Pressure at Points C_w^{30} , C_{pt}^{30} , and C_{bb}^{30} , Respectively.

strong, early arrival of the reflected shock. In fact, the three computations are showing unequivocally distinct solutions at points B^{30} , dependent directly upon the way in which the interaction of the shock and wedge was approximated geometrically.

Figure 60 shows the pressure versus time for points C_w^{30} , C_{pt}^{30} , and C_{bb}^{30} . Computation 9003.30 shows a strong reflected shock arrival at approximately $194 \mu s$, while neither of the other two computations show a reflected shock arrival during the $250 \mu s$ time shown.

Figure 61 shows the pressure versus time for points D_w^{30} , D_{pt}^{30} , and D_{bb}^{30} . Points D^{30} experience only the passage of the Mach stem. The Mach stem for 9003.30 arrives first, followed by that for 9003.121 (the rotated shock and rectangular block computation), and then 9003.23 (the 30 degree wedge on a reflecting plane. The pressures directly behind the Mach stem are all similar, with 9003.30 slightly greater, which is consistent with its earlier arrival. The pressure at late time for 9003.30 is again the highest.

Figure 62 shows the pressure versus time for points E_w^{30} , E_{pt}^{30} , and E_{bb}^{30} . Some small differences in the arrival time of the incident shock are evident. Computation 9003.30 again

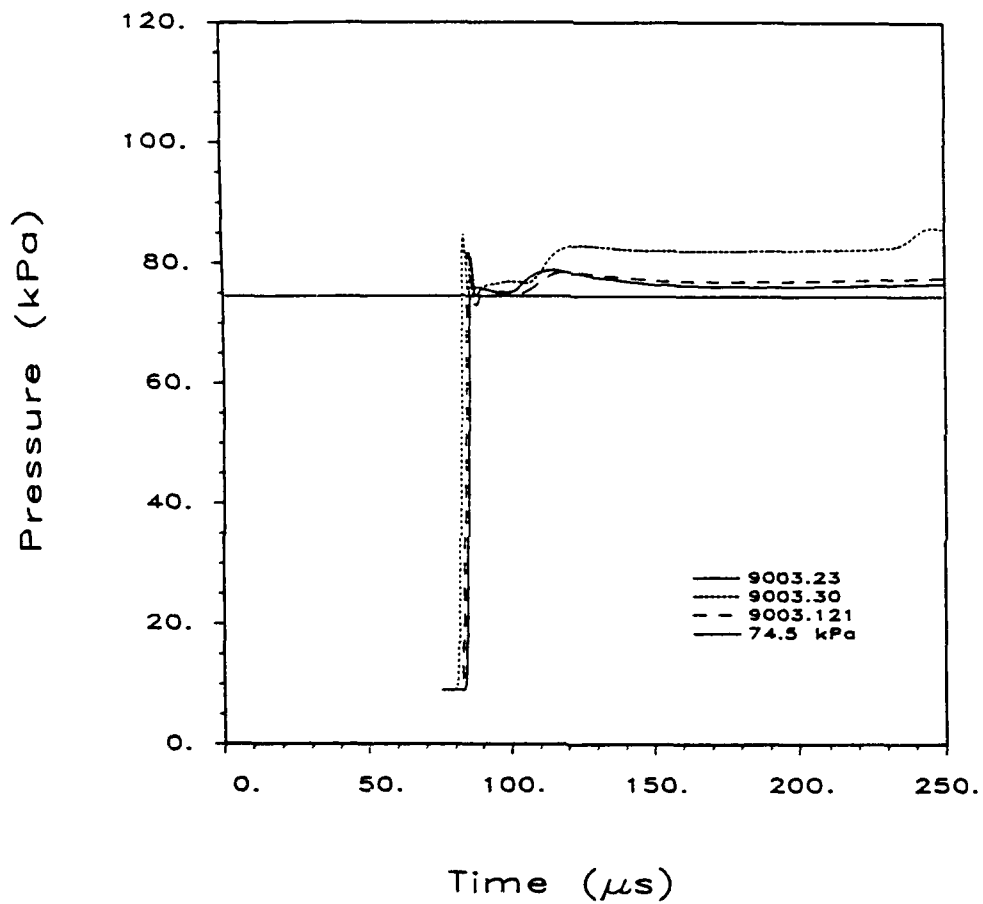


Figure 61. SHARC Computations 9003.23, 9003.30, and 9003.121, Absolute Pressure at Points D_w^{30} , D_{pt}^{30} , and D_{bb}^{30} , Respectively.

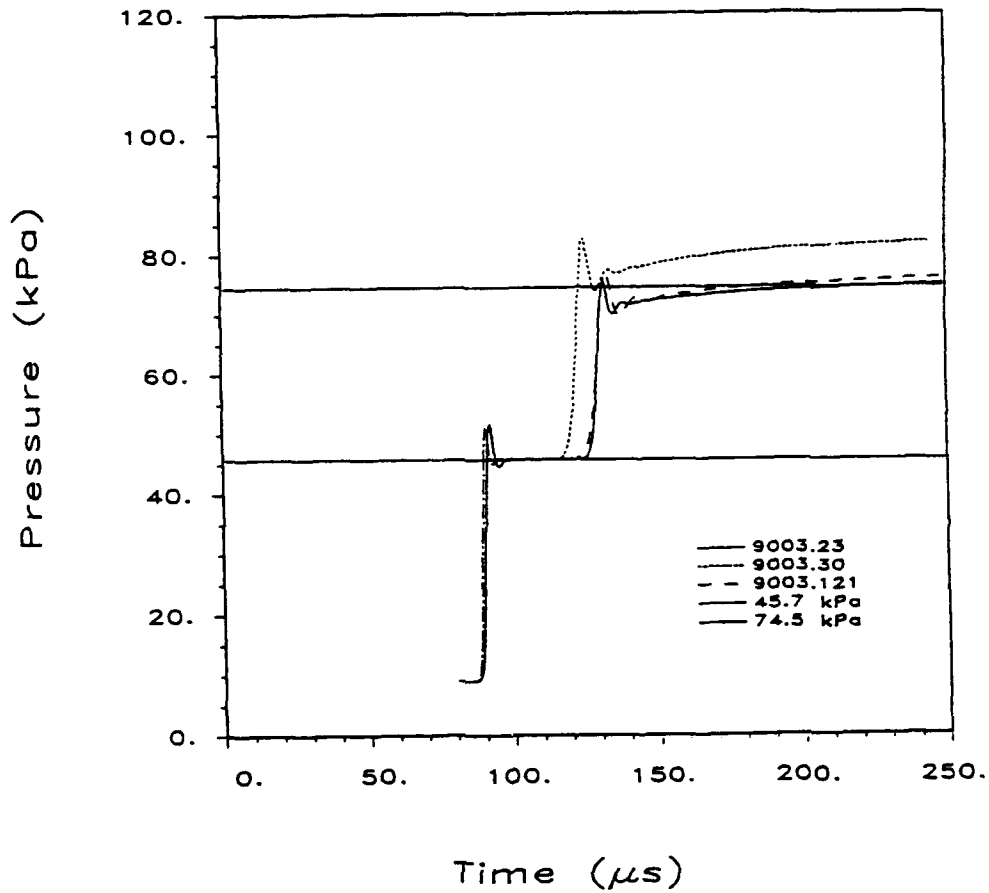


Figure 62. SHARC Computations 9003.23, 9003.30, and 9003.121, Absolute Pressure at Points E_w^{30} , E_{pt}^{30} , and E_{bb}^{30} , Respectively.

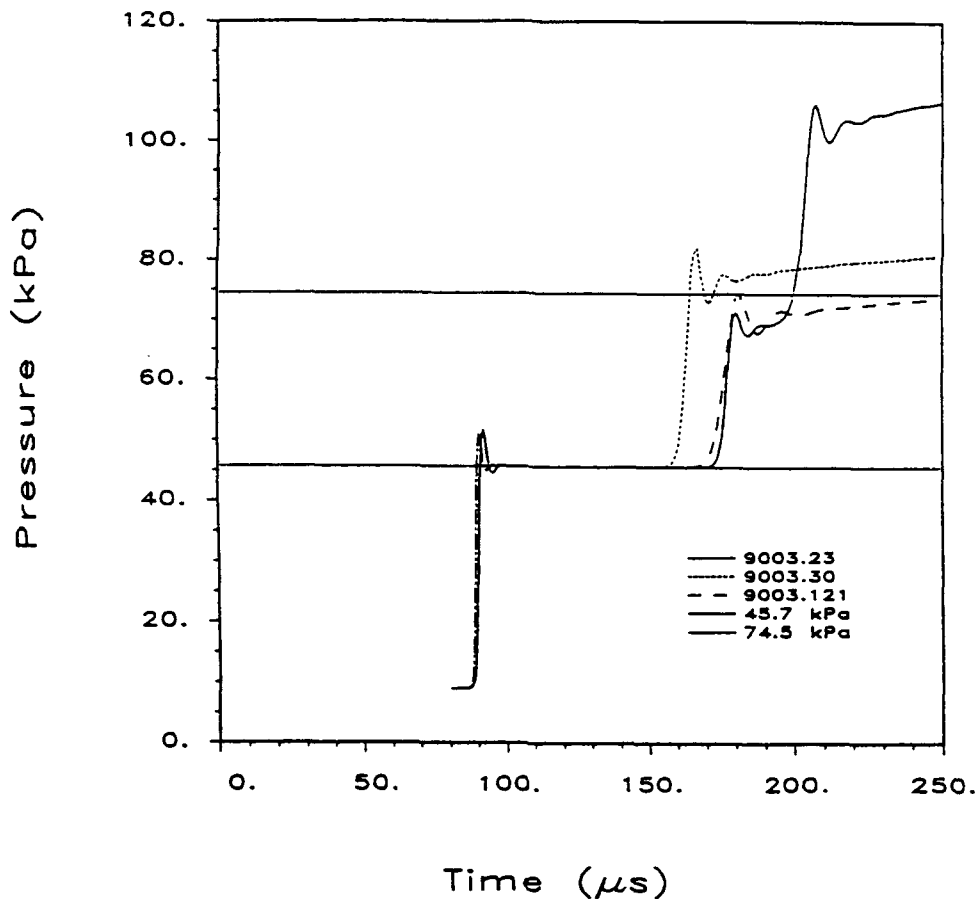


Figure 63. SHARC Computations 9003.23, 9003.30, and 9003.121, Absolute Pressure at Points F_w^{30} , F_{pt}^{30} , and F_{bb}^{30} , Respectively.

shows an earlier arrival of a reflected shock that is stronger than in the other computations.

Finally, Figure 63 shows the pressure versus time for points F_w^{30} , F_{pt}^{30} , and F_{bb}^{30} , which show similar behavior to that for points E^{30} shown in Figure 62. Figures 58 through 63 illustrate clearly that while these geometric configurations all will produce Mach reflections, they produce very distinct variations in the accompanying compression and rarefaction waves because of the different fluid dynamics involved in each geometry. These different wave interactions then drive the Mach stem and reflected shock in ways that are unique enough that the choice of geometry must be made with caution. It is useful to emphasize again that none of these geometries truly represent the Mach reflection of an idealized nuclear burst above a ground plane, even in the absence of thermal effects. Such an idealized nuclear burst above ground starts its interaction with the ground plane with a normal shock reflection at ground zero, followed by a transition to increasingly oblique shock interaction with increasing ground range.

2. The 60 Degree Wedge

The theoretical absolute reflected pressure for the simple oblique reflection¹⁵ of an incident shock I with an ambient pressure p_1 ahead of the shock, a pressure p_2 behind the shock, and a wedge angle Θ is shown in Equation 4.

$$p_r = p_2 \left[\frac{(3\gamma - 1)K - (\gamma - 1)}{(\gamma - 1)K + (\gamma + 1)} \right], \quad (4)$$

where the constant K is defined for convenience in Equation 5 as

$$K = \frac{p_1 + (p_2 - p_1) \sin\Theta}{p_1}. \quad (5)$$

As may be seen in Figure 1, regular reflection is expected for this combination of incident shock Mach number and wedge angle. The peak reflected absolute pressure for the interaction of the $M_I = 2.12$ shock listed in Table 1 with a wedge of angle $\Theta = 60$ degrees is $p_r = 150.3$ kPa, excluding any effects from the interaction from a corner rarefaction wave. For normal reflection, the "wedge angle" becomes $\Theta = 90$ degrees, so Equation 5 simplifies to $K = p_2/p_1$, and thus $p_r = 163.5$ kPa, which is the expected value.

a. SHARC Computations 9003.121 and 9003.251, and HULL122 Computation 9001.181

Two of the computations for the interaction of the $M_I = 2.12$ shock with the 60 degree wedge have already been shown in earlier figures, but not discussed in detail. Figure 34 shows the absolute pressure contours for this 60 degree interaction on the left vertical side of the rectangular block for HULL122 computation 9001.181. The contrast between the two interactions shown in Figure 34 is immediately obvious. The 30 degree interaction shows a clear Mach stem, as it should, but the 60 degree interaction does not, because this geometry does not support Mach reflection and so is within the simple oblique regular reflection region. Figure 35 shows the corresponding density contours for the 60 degree wedge interaction on the left vertical boundary of the rectangular block for 9001.181. Similarly, Figure 42 shows the absolute pressure contours for the interaction for the 60 degree wedge on the left vertical boundary of the rectangular block for SHARC computation 9003.121. This also correctly shows no Mach reflection. Figure 43, also discussed previously for the 30 degree wedge results, shows the density contours for the 60 degree wedge interaction of the left vertical boundary of the block for 9003.121.

Just as a new set of points, A_{bb}^{30} through F_{bb}^{30} , were defined off the bottom boundary of the rectangular block for a simulated shock interaction with a 30 degree wedge, so also was another new set of points, A_{bl}^{60} through F_{bl}^{60} . Here, the subscript "bl" indicates the rectangular block left boundary. These points were positioned in such a way that they were located at the same normal distances to both the incident shock and the left surface of the rectangular block as were their A_w^{30} through F_w^{30} counterparts. Thus, all shock arrival times

and growth rates are directly comparable within the 60 degree wedge computations, again except for differences caused by the modeling techniques. Table 6 shows the rounded-off

Table 6. BRL Points $A_{bl}^{60} - F_{bl}^{60}$ for the Rotated Shock and Rectangular Block Left Boundary, 60 Degree "Wedge" Computation

Position	x-Position (cm)	y-Position (cm)
A_{bl}^{60}	-0.6828	1.6827
B_{bl}^{60}	-4.7797	8.7787
C_{bl}^{60}	-7.8524	14.1008
D_{bl}^{60}	-0.4329	13.7497
E_{bl}^{60}	-3.0297	18.2476
F_{bl}^{60}	-4.9774	21.6212

coordinates for points A_{bl}^{60} through F_{bl}^{60} . These are kept the same for all of the computations for a rotated shock striking the left surface of a rectangular block to simulate a 60 degree wedge interaction.

To complete the set of computations for the 60 degree wedge interaction, SHARC computation 9003.251 was run with the $M_I = 2.12$ incident shock traveling orthogonally through a high resolution grid with $\Delta x = 0.10$ cm in the area of interest. The wedge was simulated by a combination of island and shore cells to form a smooth wedge surface resting on a bottom reflecting plane, just as was done for SHARC computation 9003.23. Computation 9003.251 was run with the artificial viscosity option turned off (visc=0), and second order advection differencing (method=4). A set of points, A_w^{60} through F_w^{60} , were defined with the same normal distances to both the incident shock at the start of the computation and the wedge surface as for A_w^{30} through F_w^{30} . As before, the leading edge of the wedge was defined as point (0.0, 0.0), with shock arrival at that point defined as $t = 0.0$. Table 7 shows the

Table 7. BRL Points $A_w^{60} - F_w^{60}$ for the 60 Degree Wedge Computation

Position	x-Position (cm)	y-Position (cm)
A_w^{60}	0.25	1.7987
B_w^{60}	0.25	9.9925
C_w^{60}	0.25	16.1379
D_w^{60}	6.501	12.1241
E_w^{60}	6.501	17.3178
F_w^{60}	6.501	21.2132

rounded-off coordinates for points A_w^{60} through F_w^{60} . The slight positive offset of 0.001 cm in x for points D_w^{60} through F_w^{60} was introduced to keep the hydrocode data station from being

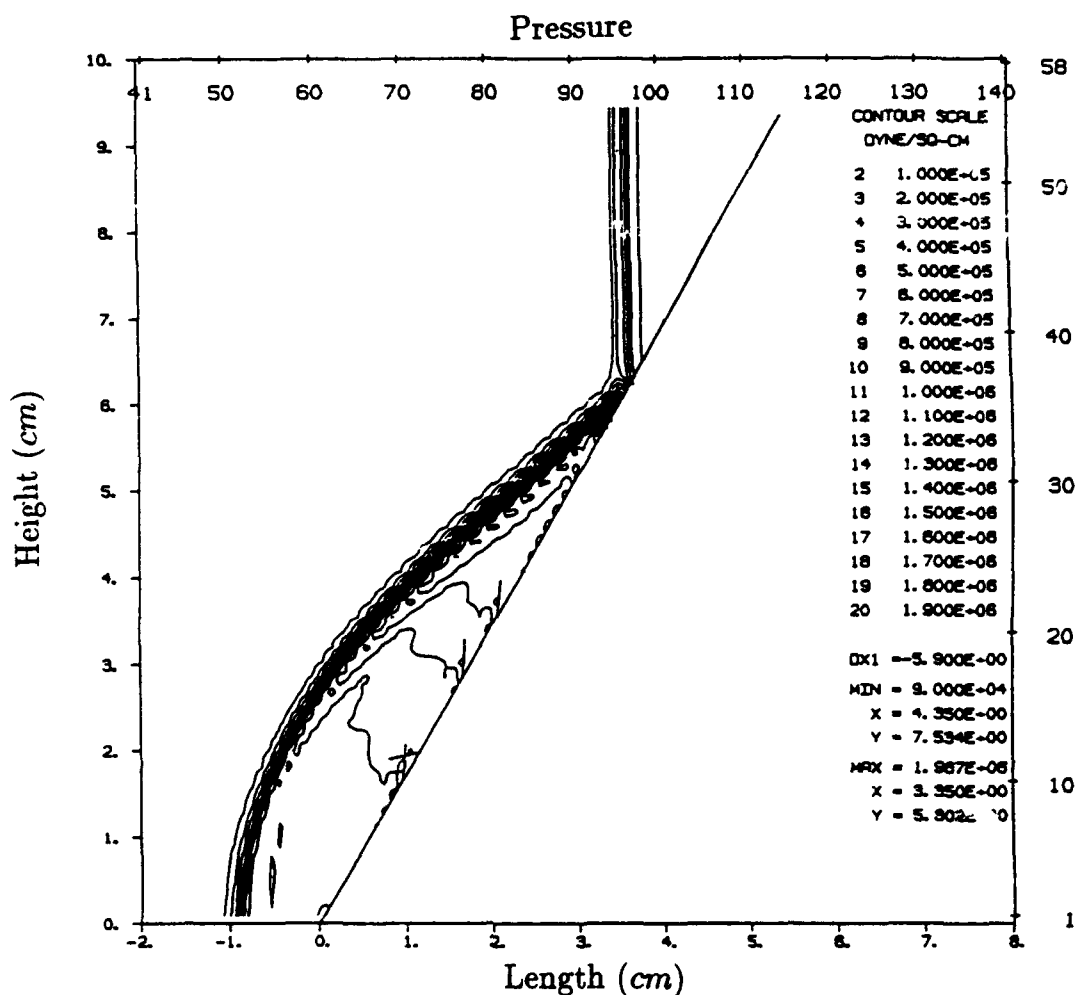


Figure 64. SHARC Problem 9003.251, 60 Degree Smooth Wedge, Absolute Pressure Contours at 50 μ s.

ambiguously placed directly on a computational cell boundary.

Figure 64 shows the absolute pressure contours for 9003.251, and Figure 65 shows the density contours for 9003.251. Note that in contrast to the incorrect results shown in Figure 11, there is no apparent numerical "shock" attached to the leading edge of the wedge in any of the SHARC and HULL122 60 degree wedge computations during the early interaction time of interest here. For completeness, it is important to note that at very late time after all of the initial shock reflection effects have dissipated, probably several milliseconds, a weak detached shock in the vicinity of the leading edge is theoretically possible. Table 1 shows that the steady state flow behind the incident shock is just barely supersonic.

Although the computations look essentially the same if just the pressure and density contours are studied, it is again instructive to examine the pressure versus time for a consistent set of points in the flow field. Figure 66 shows the pressure versus time for points A_{bl}^{60}

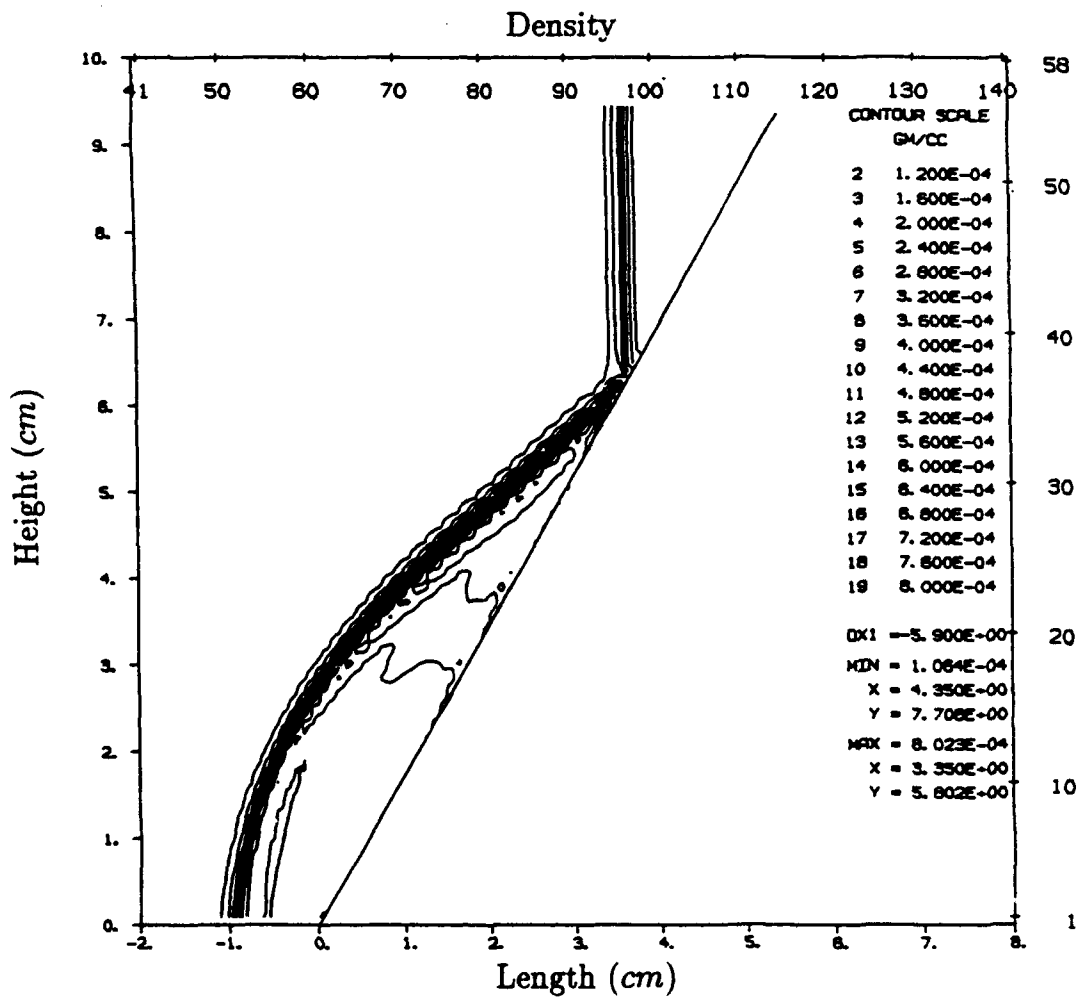


Figure 65. SHARC Problem 9003.251, 60 Degree Smooth Wedge, Density Contours at 50 μ s.

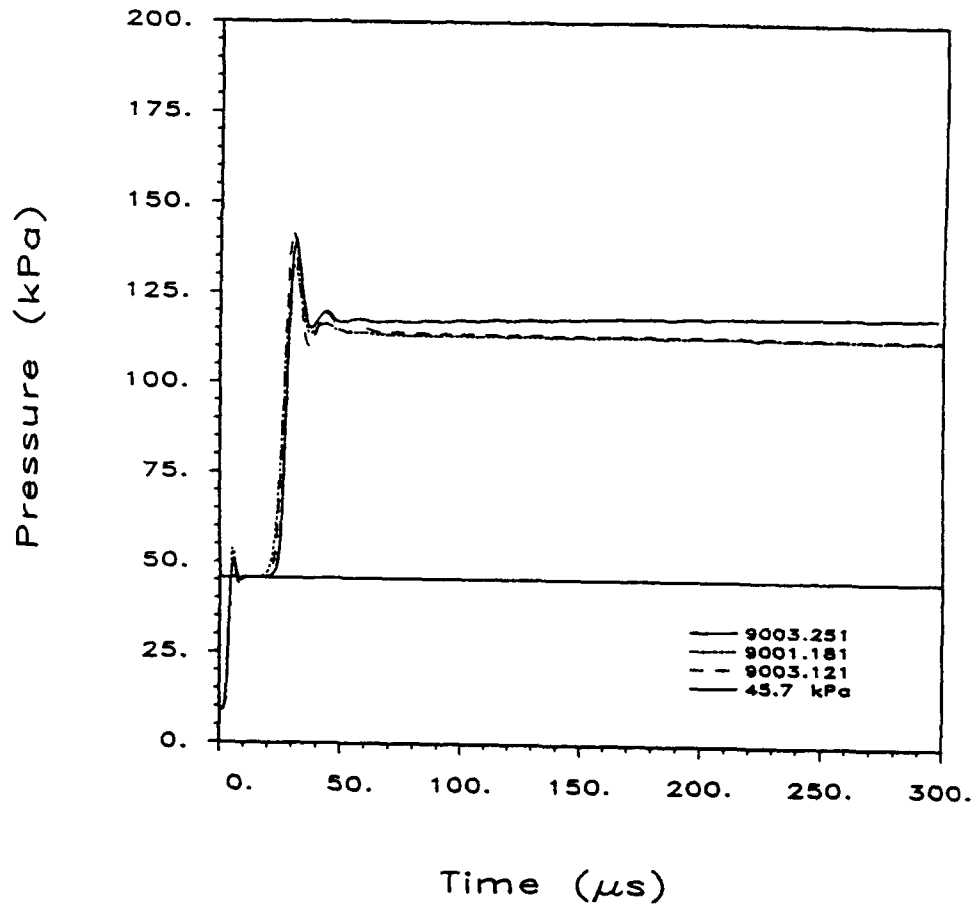


Figure 66. SHARC 9003.121 and 9003.251, and HULL122 9001.181 Computations, Absolute Pressure at Points A_{bl}^{60} and A_w^{60} .

and A_w^{60} for the three computations for a 60 degree wedge interaction. The computations all have essentially the same incident shock rise time (and initial overshoot) to the 45.7 kPa level. This serves as a good check that the computations were indeed all started with the same shock standoff and shock conditions, and all have the same definition of the location of their respective A^{60} points. There is, however, a noticeable difference in the arrival time and rise time of the reflected shock. Computation 9003.251, which is for a smooth wedge placed on a bottom reflecting boundary, shows a later arrival of the reflected shock and a higher absolute pressure at late time than do either of the other two computations which were for a rotated shock striking the leading corner of a rectangular block. This difference is due to the geometric configuration of the curvature of the reflected shock from this leading corner, and the potential for fluid dynamic communication around it. This is best illustrated by a comparison to Figure 44, which shows the absolute pressure versus time for the 30 degree wedge sides of 9003.121 and 9001.181 with computation 9003.23 for a 30 degree wedge on a reflecting plane. Both Figure 44 and Figure 66 show a later arrival of the reflected shock, and a higher pressure at late time, although to different levels because of the different reflection processes. None of the three computations in Figure 66 show the theoretical reflected plateau pressure of 150.3 kPa expected for this oblique shock reflection. This is because of the very close proximity of points A^{60} to the leading edge of the wedge. The nearly immediate arrival of the corner rarefaction wave provides rapid relief of the reflected pressure.

Figure 67 shows the pressure versus time for points B_{bl}^{60} and B_w^{60} for the three computations for a 60 degree wedge interaction. Here, there is relatively little difference between the computations, except that 9003.251 has a higher pressure at late time, and 9003.121 shows the greatest amount of higher order oscillation in the reflected shock. Points B^{60} experience only the incident shock and the oblique reflected shock, while points B^{30} for the 30 degree wedge see both the incident shock and the reflected shock that is part of the single Mach reflection system. Points B^{60} show late time pressure plateaus in the range of 113 kPa at 300 μ s for all computations, below the theoretical value of 150.3 kPa because of the leading edge rarefaction wave.

Figure 68 shows the pressure versus time for points C_{bl}^{60} and C_w^{60} for the three computations for a 60 degree wedge interaction. All three computations show nearly the same incident shock interaction at early time. Points C^{30} show only the passage of the incident shock from the single Mach reflection system during the 250 μ s computation time, but the reflected shock should also pass at a later time. The computations for the 60 degree wedge points C^{60} , computed to 300 μ s, all show the passage of both the incident shock and then the simple obliquely reflected shock at about 280 μ s. Arrival times of the reflected shocks are nearly identical.

Figure 69 shows the pressure versus time for points D_{bl}^{60} and D_w^{60} . The timing of the incident shock arrivals is the same for all computations. Computation 9003.251 for the wedge on the reflecting surface shows an earlier reflected shock arrival, and less of a reflected shock pressure peak which may be due simply to a less severe overshoot and the different leading edge effects. All three computations show a brief but clear pressure plateau of approximately 147 kPa, close to the theoretical value of 150.3 kPa, at around 136 μ s. Computation 9003.251 shows a slightly greater pressure at late time.

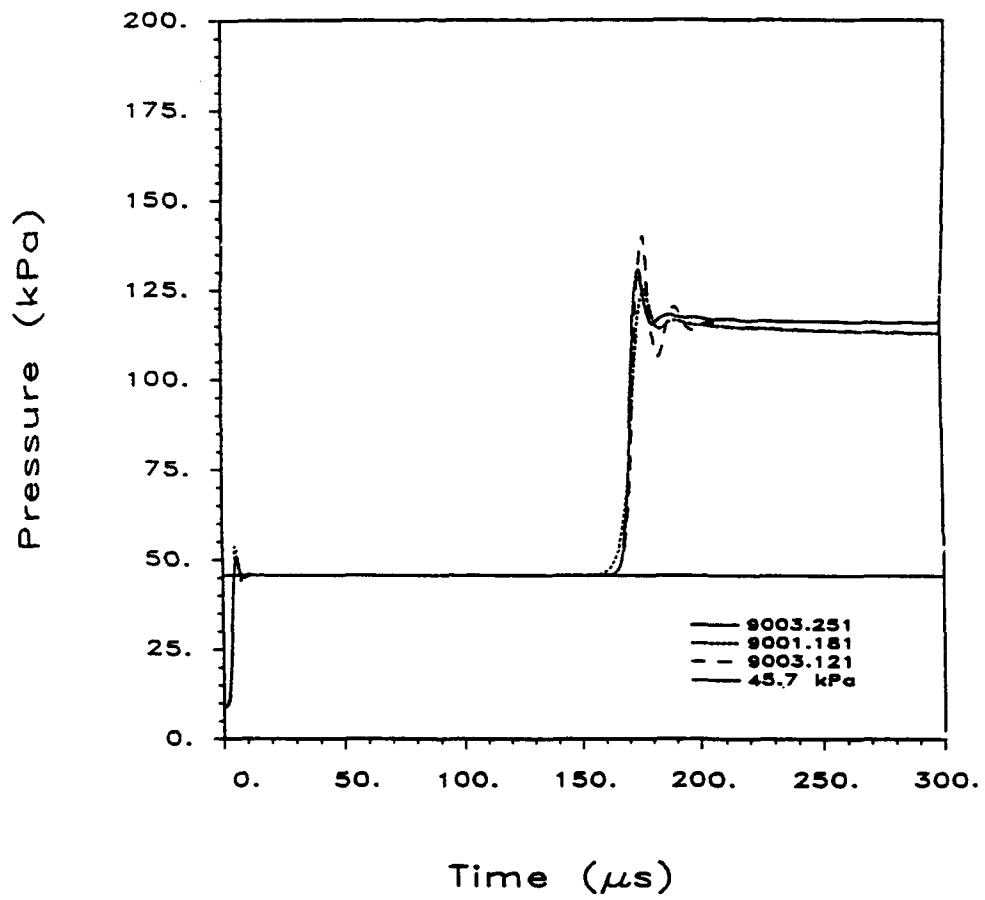


Figure 67. SHARC 9003.121 and 9003.251, and HULL122 9001.181 Computations, Absolute Pressure at Points B_{bl}^{60} and B_w^{60} .

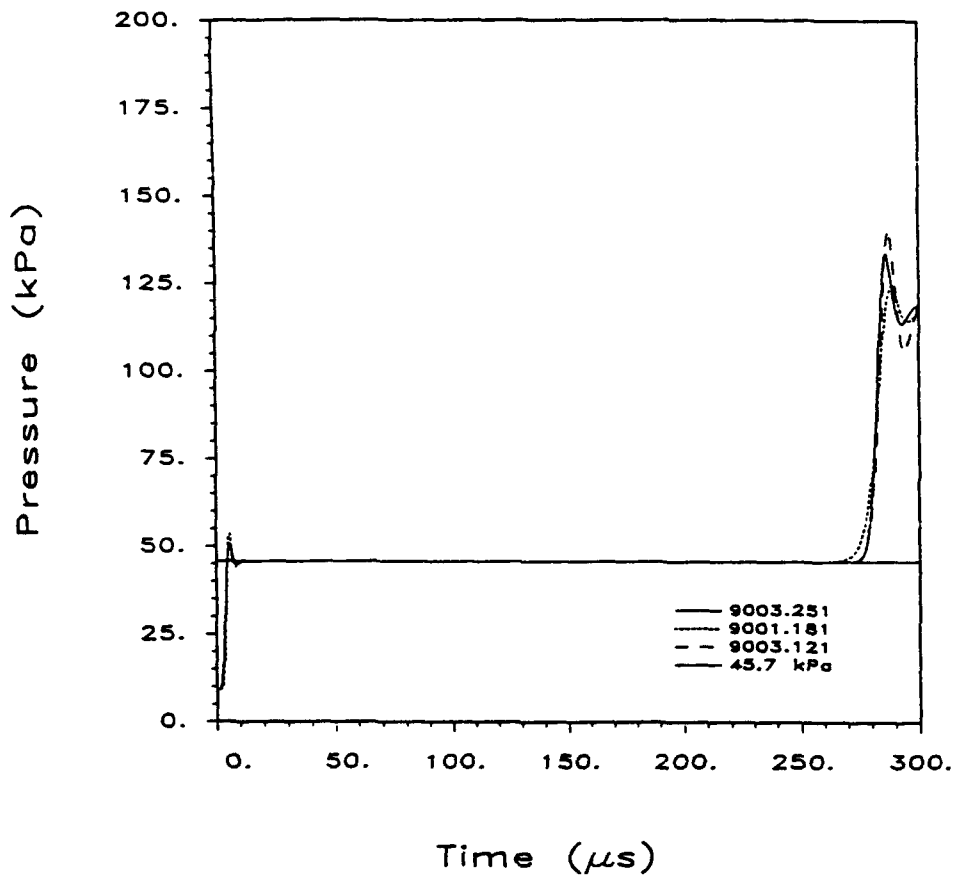


Figure 68. SHARC 9003.121 and 9003.251, and HULL122 9001.181 Computations, Absolute Pressure at Points C_{bl}^{60} and C_w^{60} .

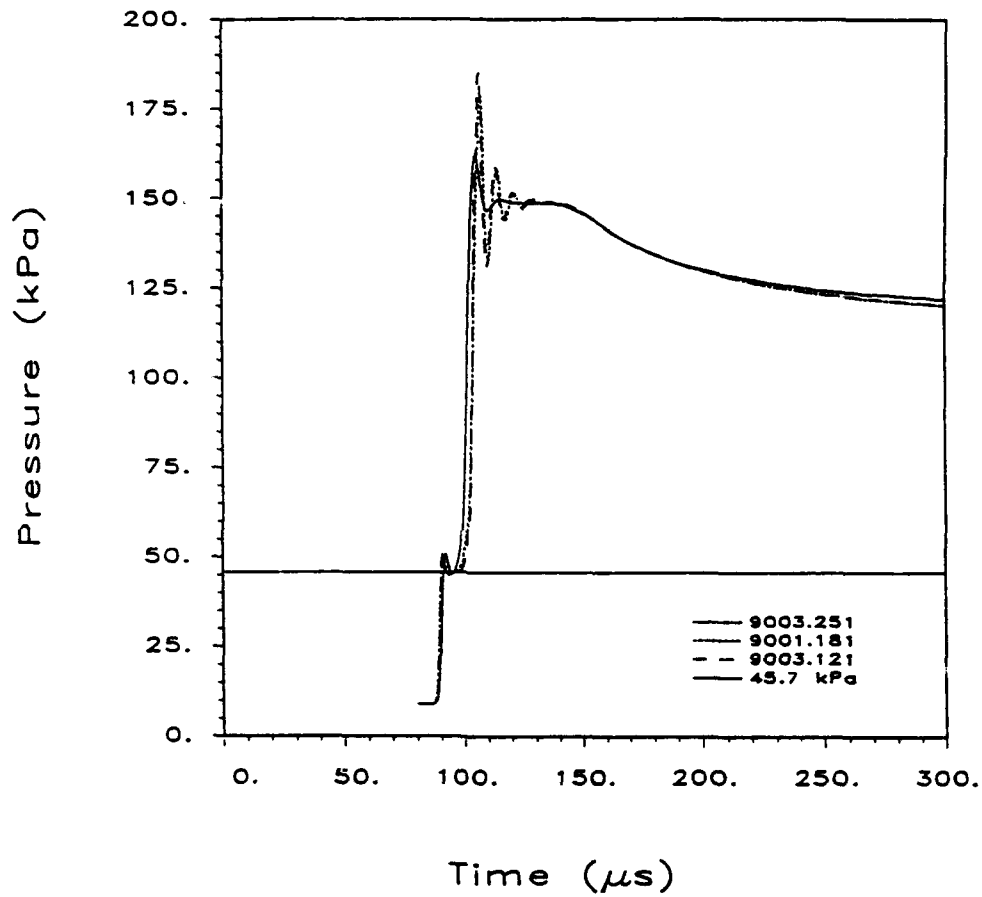


Figure 69. SHARC 9003.121 and 9003.251, and HULL122 9001.181 Computations, Absolute Pressure at Points D_{bl}^{60} and D_w^{60} .

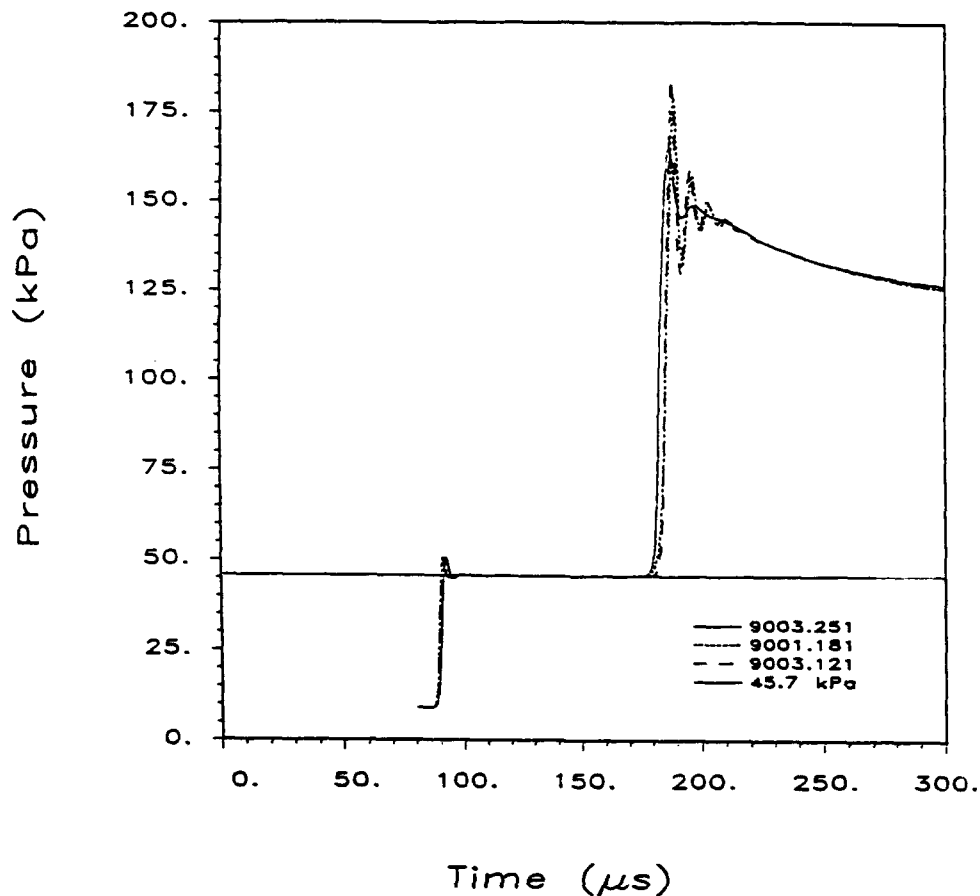


Figure 70. SHARC 9003.121 and 9003.251, and HULL122 9001.181 Computations, Absolute Pressure at Points E_{bl}^{60} and E_w^{60} .

Figure 70 shows the pressure versus time for points E_{bl}^{60} and E_w^{60} . As expected, the timing of the incident shock is essentially the same. The reflected shock for 9003.251 arrives ahead of the reflected shocks for point E_{bl}^{60} . The final pressures are nearly the same for all computations.

Figure 71 shows the pressure versus time for points F_{bl}^{60} and F_w^{60} . The trends for points F^{60} are similar to those for points E^{60} , except that the arrival of the reflected shock is essentially the same for all computations. After some differing amounts of oscillations, all computations show the same pressure decay.

3. The 45 Degree Wedge

As may be seen in Figure 1, this combination of incident shock Mach number, $M_I = 2.12$, and wedge angle $\Theta = 45$ degrees should be expected to produce complex Mach reflection (CMR). Thus, the simple oblique reflection theory in Equation 4 does not apply. Here,

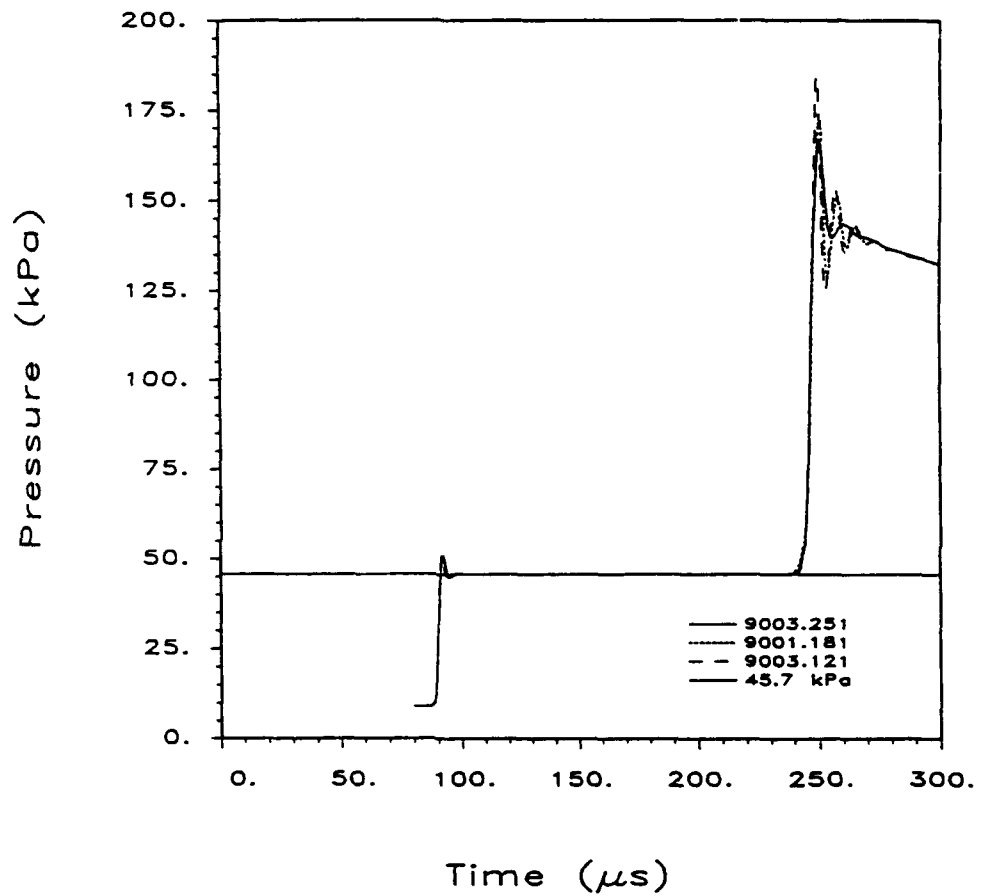


Figure 71. SHARC 9003.121 and 9003.251, and HULL122 9001.181 Computations, Absolute Pressure at Points F_{bl}^{60} and F_w^{60} .

the simple theory predicts a peak reflected pressure of 139.0 *kPa*, which is a useful piece of information only in that it indicates that the actual reflection process, in the absence on leading edge rarefaction wave effects, should be expected to produce a higher pressure.

a. SHARC Computation 9003.241 and HULL122 Computation 9001.031

Two main computations were run for the interaction of the $M_I = 2.12$ incident shock on a 45 *degree* wedge. SHARC computation 9003.241 was run with the incident shock traveling orthogonally through a high resolution grid with $\Delta x = 0.10$ *cm* in the area of interest. The wedge was simulated by a combination of island and shore cells to form a smooth wedge surface resting on a bottom reflecting plane, just as was done for other SHARC computations such as 9003.23. Computation 9003.241 was run with the artificial viscosity option turned off ($\text{visc}=0$), and second order advection differencing ($\text{method}=4$). Figure 72 shows the absolute pressure contours for 9003.241, and Figure 73 shows the density contours for 9003.241. Both Figure 72 and Figure 73 show the development of a Mach stem, but no clear evidence of CMR development.

HULL122 computation 9001.031 was run with a rotated incident shock traveling through a similar high resolution grid with $\Delta x = 0.10$ *cm* in the area of interest. The 45 *degree* wedge was simulated by having the incident shock strike the corner of a rectangular block with its major axes collocated with those of the grid. Computation 9001.031 was run with the artificial viscosity option turned off ($\text{visc}=0$), and the default HULL differencing ($\text{method}=2$). Figure 74 shows the absolute pressure contours for 9001.031, and Figure 75 shows the density contours for 9001.031. Both Figure 74 and Figure 75 show the development of a Mach stem, but no clear evidence of CMR development, just as for the SHARC computation. The two figures also give a qualitative indication that the HULL122 computation is showing proper symmetry.

Although the computations look essentially the same if just the pressure and density contours are studied, it is again instructive to examine the pressure versus time for a consistent set of points in the flow field. For this purpose, a new set of reference points A_w^{45} through F_w^{45} are defined for SHARC computation 9003.241, and shown in Table 8. These point positions are for a 45 *degree* wedge on a reflecting plane. The points were positioned to satisfy the criterion that all computations for all configurations be started with the incident shock 1.0 *cm* upstream from either the leading edge of the wedge or the leading corner in the block and rotated shock computations. The points A_w^{45} through F_w^{45} were also positioned so that they were simultaneously at exactly the same normal distances from the incident shock front and the wedge surface as were their A_w^{30} through F_w^{30} counterparts for the 30 *degree* wedge computations. Thus, incident shock arrival times can be directly compared, and any Mach stem growth or lack of growth can be measured against the same relative position for this wedge angle.

The same procedure was followed to define point positions A_{bb}^{45} through F_{bb}^{45} for the rotated shock and rectangular block computation simulating the 45 *degree* wedge interaction, shown in Table 9. These point positions are for the block bottom boundary, but could also

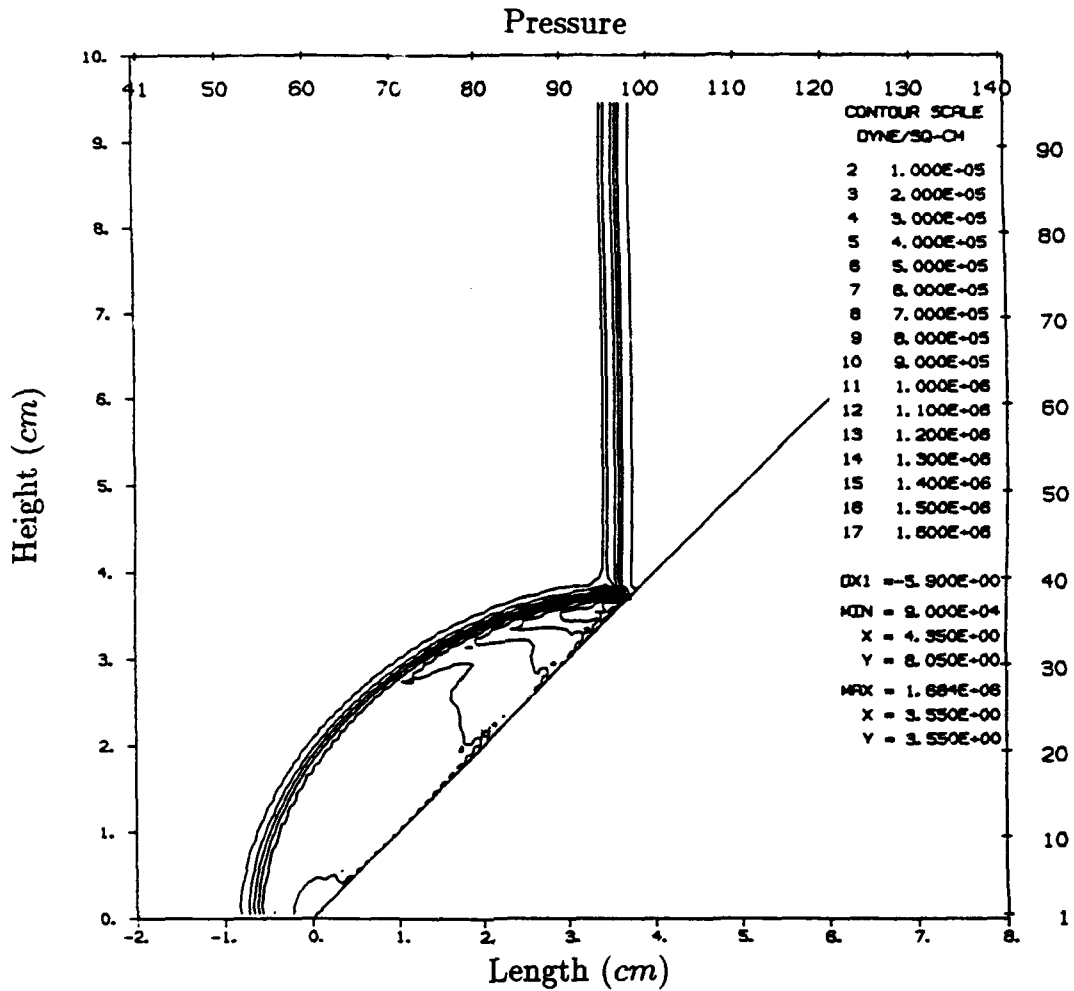


Figure 72. SHARC Problem 9003.241, 45 Degree Smooth Wedge, Absolute Pressure Contours at 50 μ s.

Table 8. BRL Points A_w^{45} - F_w^{45} for the 45 Degree Wedge SHARC Computation 9003.241

Position	x-Position (cm)	y-Position (cm)
A_w^{45}	0.250	1.2153
B_w^{45}	0.250	7.0096
C_w^{45}	0.250	11.3550
D_w^{45}	6.501	7.1122
E_w^{45}	6.501	10.7847
F_w^{45}	6.501	13.5392

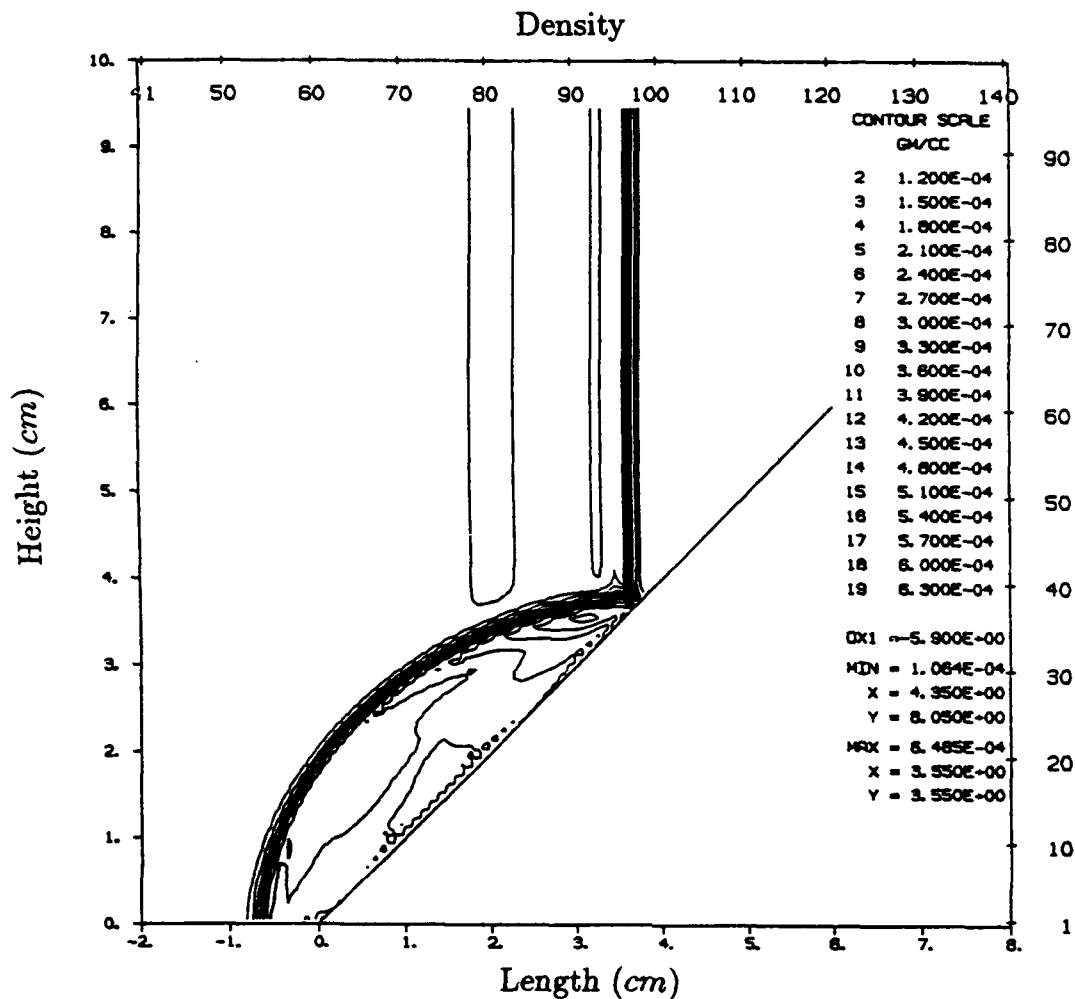


Figure 73. SHARC Problem 9003.241, 45 Degree Smooth Wedge, Density Contours at 50 μ s.

Table 9. BRL Points A_{bb}^{45} - F_{bb}^{45} for the Rotated Shock and Rectangular Block Bottom Boundary, 45 Degree "Wedge" Computation

Position	x-Position (cm)	y-Position (cm)
A_{bb}^{45}	1.0364	-0.6828
B_{bb}^{45}	5.1333	-4.7797
C_{bb}^{45}	8.2060	-7.8524
D_{bb}^{45}	9.6252	-0.4329
E_{bb}^{45}	12.2221	-3.0297
F_{bb}^{45}	14.1698	-4.9774

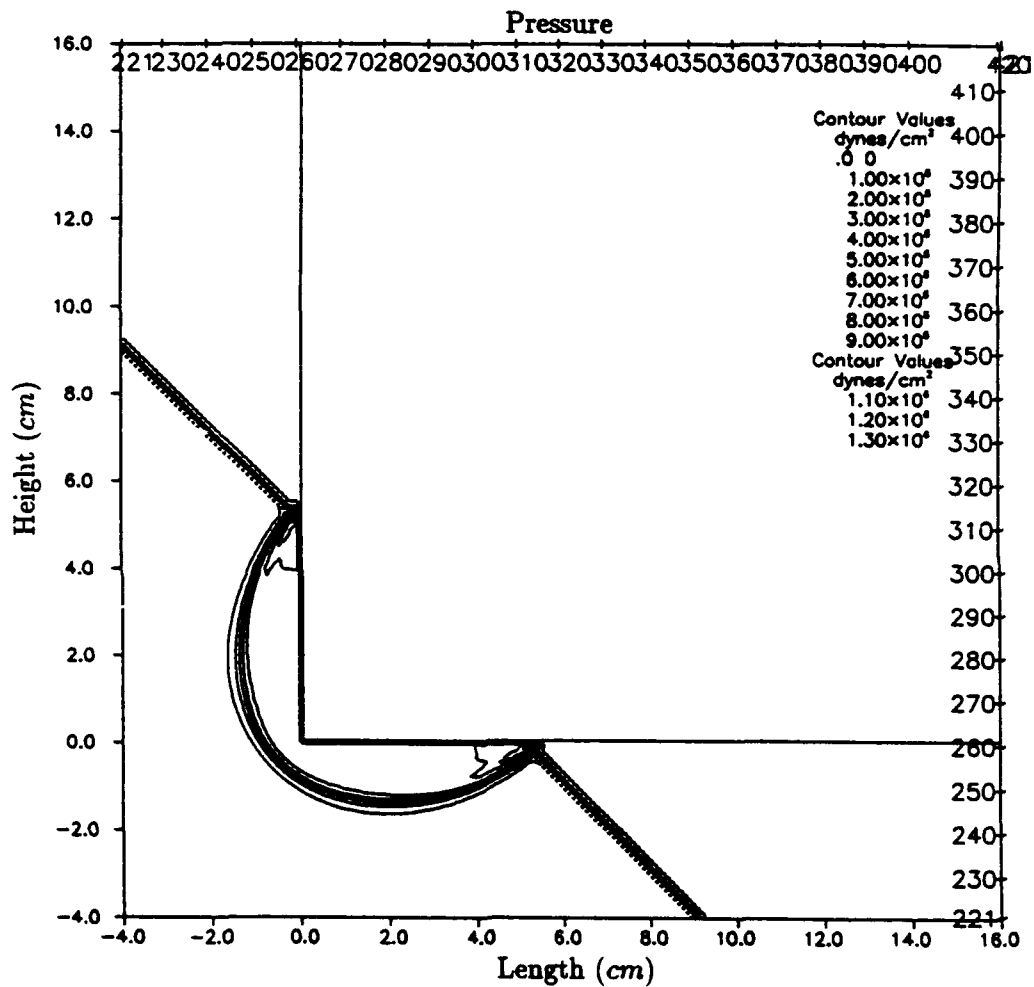


Figure 74. HULL122 Problem 9001.031, 45 Degree Smooth Wedge (Left and Bottom), Absolute Pressure Contours at 50 μ s.

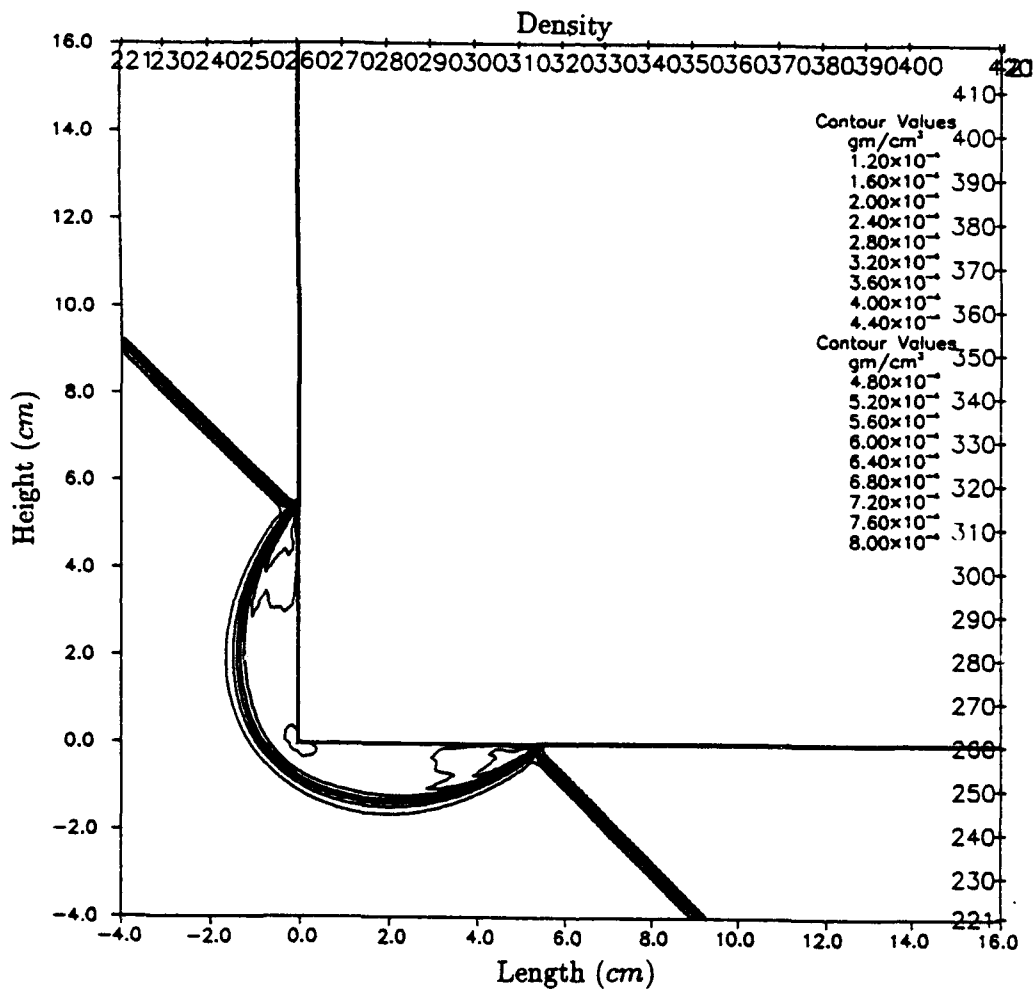


Figure 75. HULL122 Problem 9001.031, 45 Degree Smooth Wedge (Left and Bottom), Density Contours at 50 μ s.

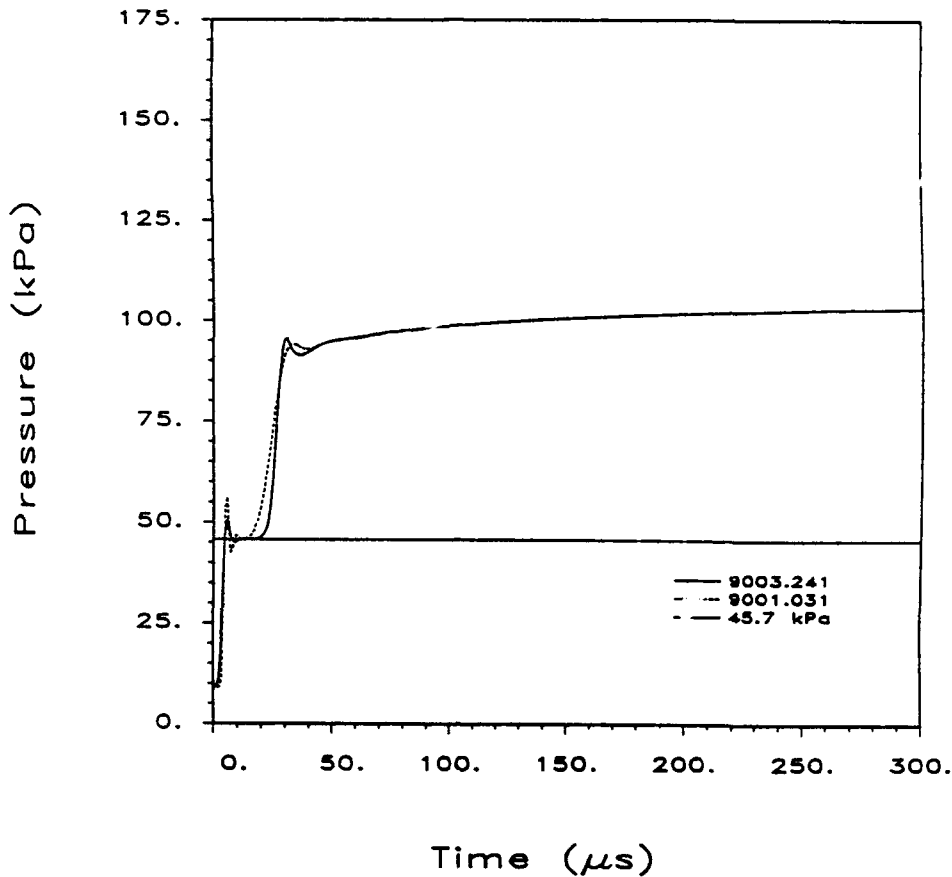


Figure 76. SHARC 9003.241 and HULL122 9001.031 Computations, Absolute Pressure at Points A_w^{45} and A_{bb}^{45} .

be for the block left boundary if the values for the x and y positions were reversed, one for one.

Figure 76 shows the pressure versus time for points A_w^{45} and A_{bb}^{45} for the two computations for a 45 degree wedge interaction. The computations have essentially the same pressure versus time for the incident shock, except for the greater diffusion in 9001.031 for the reflected shock, and the greater incident shock overshoot, also in 9001.031. The reflected shock for 9001.031 arrives slightly earlier than that for 9003.241. As noted above, the simple oblique reflection theory in the absence of corner rarefaction wave effects predicts a peak reflected pressure of 139.0 kPa, which for this configuration should be below the actual peak value. The computed peak, excluding the estimated amount of overshoot, is approximately 92 kPa before the start of the general drift upward in value. This lower than desired value is due to a combination of numerical diffusion and the nearly immediate arrival of the rarefaction wave from the leading edge (or corner) of the simulated wedge. The late time pressures are nearly identical, reaching 103.1 kPa by 300.0 μ s.

Figure 77 shows the pressure versus time for points B_w^{45} and B_{bb}^{45} for the two compu-

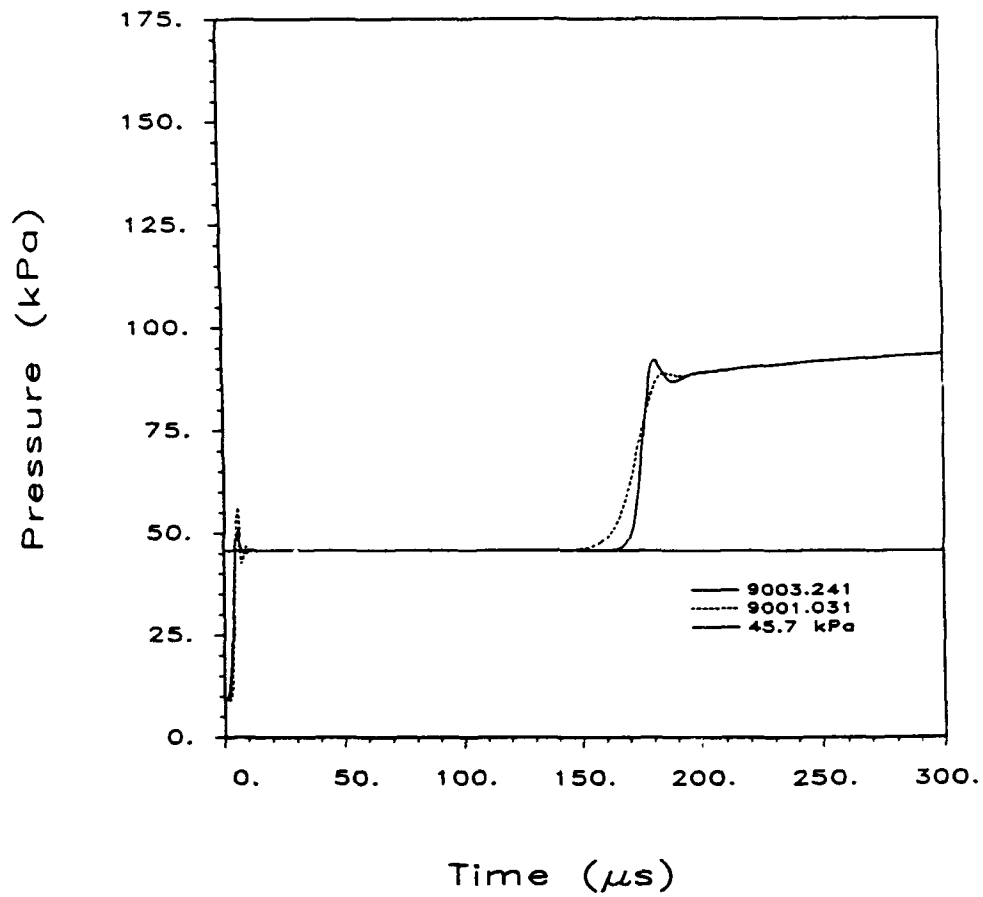


Figure 77. SHARC 9003.241 and HULL122 9001.031 Computations, Absolute Pressure at Points B_w^{45} and B_{bb}^{45} .

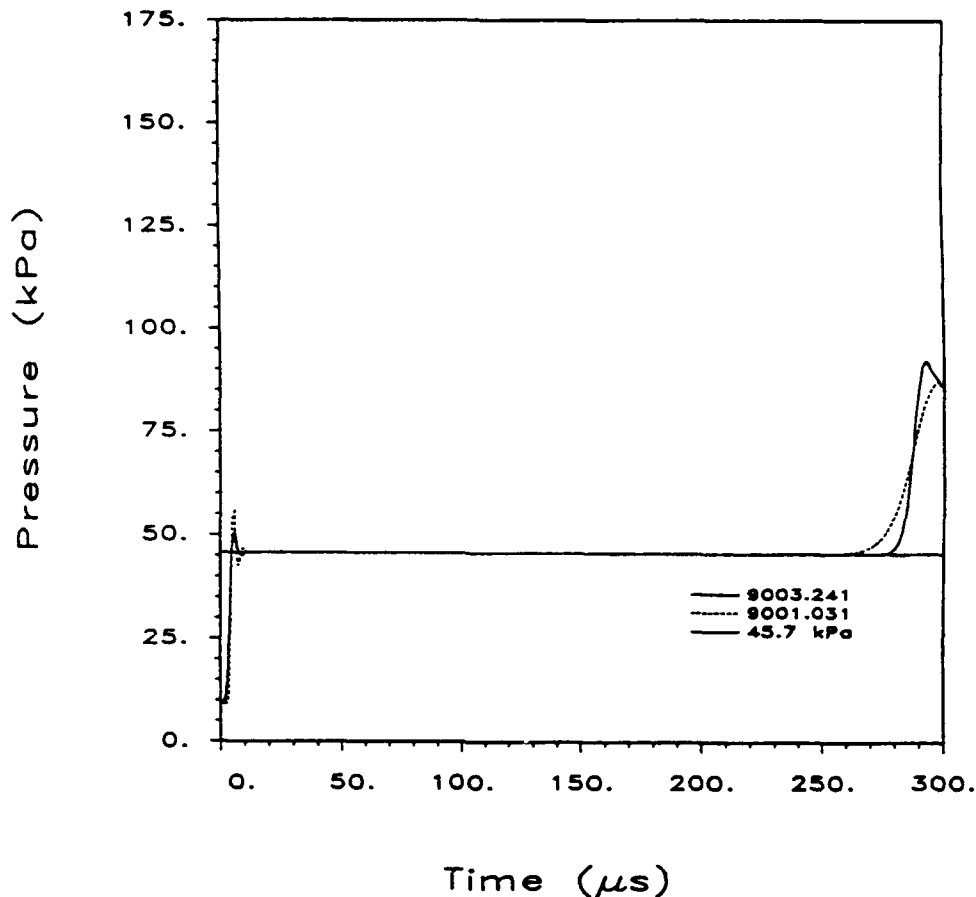


Figure 78. SHARC 9003.241 and HULL122 9001.031 Computations, Absolute Pressure at Points C_w^{45} and C_{bb}^{45} .

tations for a 45 degree wedge interaction. The computations show similar behavior for the incident shock to that for points A^{45} . The reflected shock for 9001.031 shows more diffusion and a somewhat earlier arrival time. The pressures at late time are nearly identical, reaching 93.3 kPa at 300.0 μ s. Figure 78 shows the pressure versus time for points C_w^{45} and C_{bb}^{45} . It shows similar behavior to that for points B^{45} .

Figure 79 shows the pressure versus time for points D_w^{45} and D_{bb}^{45} , which should see a complex Mach reflection only, or at least the beginnings of it. It is particularly interesting because both computations do show a double peak in pressure which is characteristic of complex Mach reflection at around 100 μ s. The Mach stem for 9001.031 arrives just before that for 9003.241.

Figure 80 shows the pressure versus time for points E_w^{45} and E_{bb}^{45} , which should experience first the incident shock passage, and then the reflected shock passage. Note that the incident shock for 9001.031 arrives earlier than for 9003.241, but that 9003.241 has the earlier arrival for the reflected shock. Finally, Figure 81 shows the pressure versus time for points F_w^{45} and F_{bb}^{45} , which, like points E^{45} , show the incident shock passage and

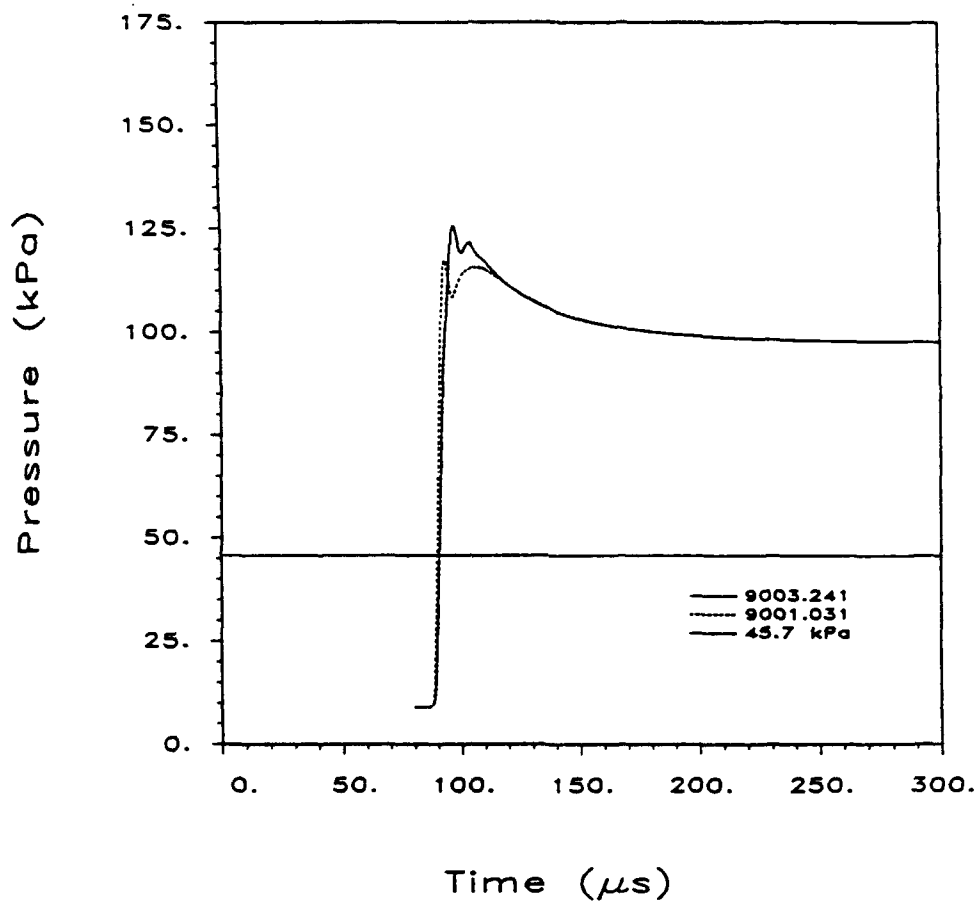


Figure 79. SHARC 9003.241 and HULL122 9001.031 Computations, Absolute Pressure at Points D_w^{45} and D_{bb}^{45} .

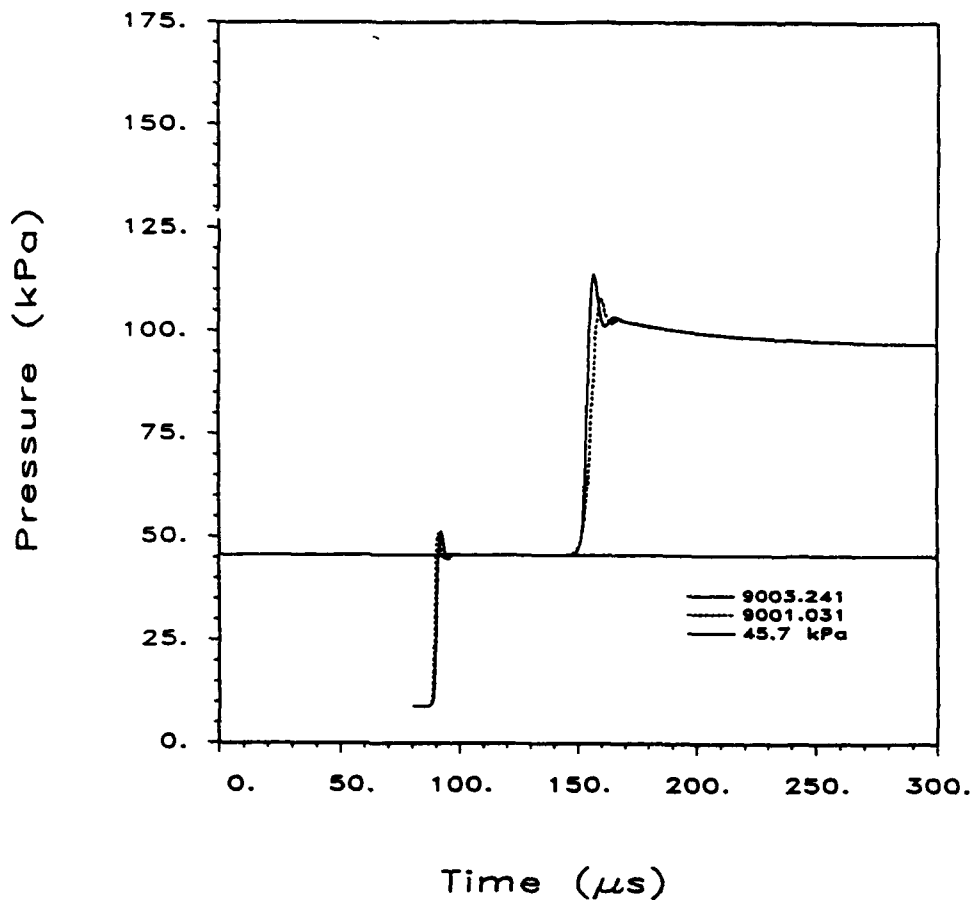


Figure 80. SHARC 9003.241 and HULL122 9001.031 Computations, Absolute Pressure at Points E_w^{45} and E_{bb}^{45} .

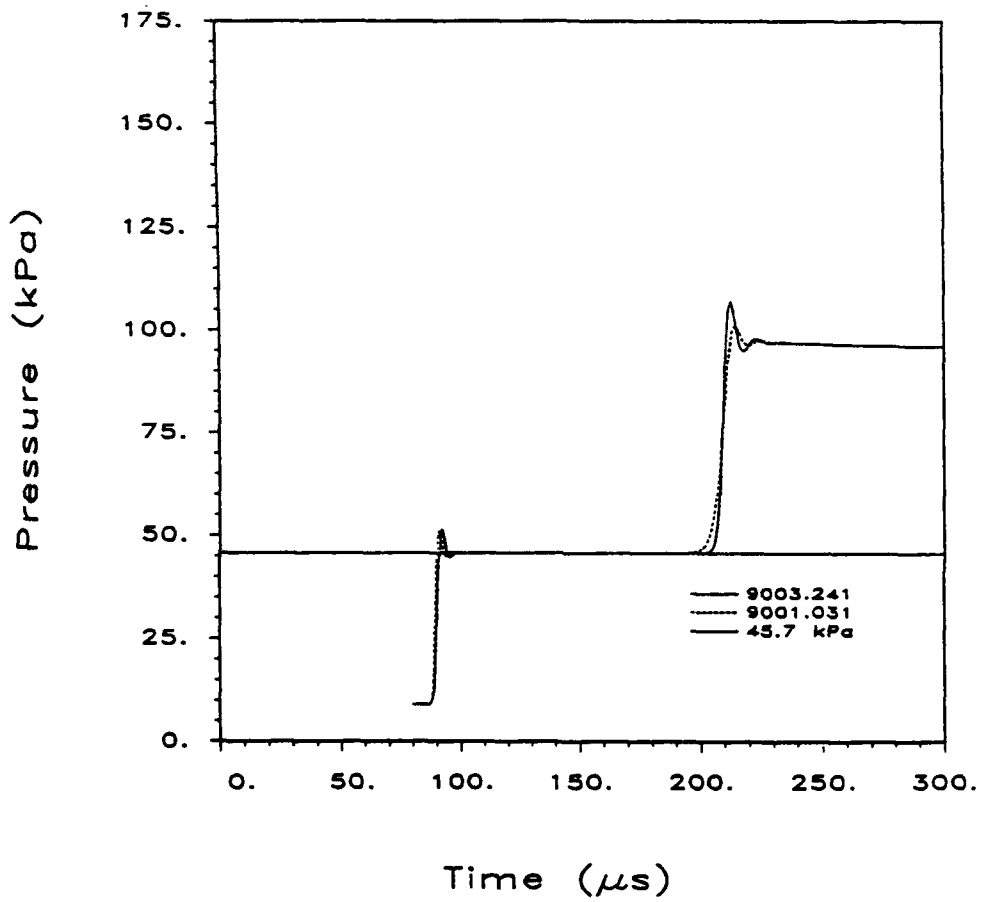


Figure 81. SHARC 9003.241 and HULL122 9001.031 Computations, Absolute Pressure at Points F_w^{45} and F_{bb}^{45} .

then the passage of the reflected shock. The respective shock arrivals are nearly the same for both computations.

II. Conclusion

The amount of data presented in this report is of such volume that a detailed summary of all results here is impractical. Nonetheless, at least some feeling for what has been demonstrated here may be obtained by summarizing the results for points *E*, which show virtually all of the various phenomena within the set of variations explored here. Although the direct passage of the Mach stem, if it exists, typically does not occur for points *E*, the passage of the reflected shock occurs relatively soon after the Mach stem has passed underneath the point. These results are summarized in Table 10 for the 30 degree wedge for which a Mach stem occurs, Table 11 for the 45 degree wedge which also generates a Mach stem, and Table 12 for the 60 degree wedge which does not generate a Mach stem, each with variations noted relative to a specified reference computation for that simulated angle. As before, there is no implication that the choice here of a computation as a reference is necessarily an endorsement that it represents a recommended best way of solving this fluid dynamic problem.

The apparent attached "shock" at the leading edge of the 60 degree wedge in the EMI STEALTH computation is an unexplained anomaly in either the STEALTH computation itself, or, less likely, in the associated contour plotting utility. Neither the HULL122 nor SHARC computations indicated a similar phenomena. Theory clearly indicates that an attached shock should not develop during this interaction at this early time, and would have only a marginal chance of existing at later time because of the very weak supersonic nature (local Mach number $M = 1.0275$) of the flow behind the $M_I = 2.12$ incident shock. It is possible that the problem in the STEALTH computation was simply a boundary definition problem. STEALTH is a Lagrangian code, with parameters defined at computational cell vertices. It may be that the vertex at the wedge leading edge was mathematically overdefined in an unsuccessful attempt to satisfy both the flow boundary conditions for the inclined wedge plane and the horizontal plane upstream from the wedge. Both the SHARC and HULL122 codes were capable of doing the problems presented to them, with an advantage to SHARC because of the added versatility made available by the shore cells. The new SHARC differencing (method=4) seemed to have as many negative aspects as positive aspects. It generally shows too much high order noise unless artificial viscosity is invoked, making its advantage over the older differencing (method=2) without using artificial viscosity almost a matter of preference rather than substance.

The use of pressure or density contour plots alone, or variations on them, in comparison to shadowgraphs to determine the validity of a given hydrocode solution constitutes a necessary but not sufficient conditional test. It has been demonstrated here that computations which produce pressure and density contour plots that superficially appear to be nearly identical can have distinctly different pressure histories at comparable points. It is

Table 10. Summary of Results for Points E for the 30 Degree Wedge

PROBLEM, WEDGE, SHOCK	REF. COMP.	WEDGE ANGLE	INCIDENT SHOCK	REFLECTED SHOCK
9003.23, SHORE, ORTHOGONAL	Ref. Comp.	30	- - -	- - -
9001.071, STEP, ORTHOGONAL	9003.23	30	Arrival: Early Early Pressure: Low Late Pressure: Same	Arrival: Same Early pressure: Low Late pressure: High
9001.181, BLOCK, ROTATED	9003.23	30	Arrival: Early Early Pressure: Low Late Pressure: High	Arrival: Early Early pressure: Low Late pressure: High
9002.12, STEP, ORTHOGONAL	9003.23	30	Arrival: Same Early Pressure: Same Late Pressure: Same	Arrival: Early Early pressure: High Late pressure: Same
9003.121, BLOCK, ROTATED	9003.23	30	Arrival: Early Early Pressure: Low Late Pressure: Same	Arrival: Same Early pressure: Same Late pressure: High
9003.26, SHORE, ORTHOGONAL	9003.23	30	Arrival: Same Early Pressure: Low Late Pressure: Same	Arrival: Early Early pressure: Low Late pressure: Same
9003.27, SHORE, ORTHOGONAL	9003.23	30	Arrival: Early Early Pressure: Low Late Pressure: High	Arrival: Early Early pressure: Low Late pressure: Same
9003.28, SHORE, ORTHOGONAL	9003.23	30	Arrival: Early Early Pressure: Low Late Pressure: High	Arrival: Early Early pressure: Low Late pressure: Same
9003.30, PLANE/TOP, ROTATED	9003.23	30	Arrival: Early Early Pressure: Same Late Pressure: Same	Arrival: Early Early pressure: High Late pressure: High
BLAST2D, WEDGE, MAPPED	9003.23	30	Arrival: Late Early Pressure: Low Late Pressure: Same	Arrival: Late Early pressure: Low Late pressure: Same
STEALTH, WEDGE, LAGRANGE	9003.23	30	Arrival: Late Early Pressure: Low Late Pressure: High	Arrival: Early Early pressure: Low Late pressure: Same

Table 11. Summary of Results for Points E for the 45 Degree Wedge

PROBLEM, WEDGE, SHOCK	REF. COMP.	WEDGE ANGLE	INCIDENT SHOCK	REFLECTED SHOCK
9003.241, SHORE, ORTHOGONAL	Ref. Comp.	45	- - -	- - -
9001.031, BLOCK, ROTATED	9003.241	45	Arrival: Early Early Pressure: Same Late Pressure: Same	Arrival: Late Early pressure: Low Late pressure: Same

Table 12. Summary of Results for Points E for the 60 Degree Wedge

PROBLEM, WEDGE, SHOCK	REF. COMP.	WEDGE ANGLE	INCIDENT SHOCK	REFLECTED SHOCK
9003.251, SHORE, ORTHOGONAL	Ref. Comp.	60	- - -	- - -
9003.121, BLOCK, ROTATED	9003.251	60	Arrival: Early Early Pressure: Same Late Pressure: Same	Arrival: Late Early pressure: High Late pressure: Low
9001.181, BLOCK, ROTATED	9003.251	60	Arrival: Early Early Pressure: Same Late Pressure: Same	Arrival: Late Early pressure: High Late pressure: Low

well known that shock wave arrivals, rise times, and strengths are functions of computational grid resolution, differencing techniques, and imposed artifices for the sake of stability such as artificial viscosity. This study has added some quantitative measure to their effects. This study has also quantified the different fluid dynamic phenomena associated with the various geometric configurations used to computationally simulate Mach reflection. Each geometric configuration studied here has its own unique set of secondary expansion and compression waves which respectively shape and drive the primary Mach and reflected shocks in ways that must be evaluated carefully. None of the geometries discussed here exactly match a complete Mach reflection fluid dynamic wave system from even a highly idealized burst of a nuclear device above ground.

References

1. H.M. Glaz, P. Collella, I.I. Glass, and R.L. Deschambault, "A Detailed Numerical, Graphical, and Experimental Study of Oblique Shock Wave Reflections," UTIAS Report No. 285, Institute for Aerospace Studies, University of Toronto, Downsview, Ontario, Canada, August 1986.
2. W. Heilig and W. Korner, "The Shock Loading on Various Steep Wedges Calculated by the STEALTH code and Compared with Experimental Data," Proceedings of the Tenth International Symposium on Military Applications of Blast Simulation, Volume I, Bad Reichenhall, Federal Republic of Germany, 21-25 September, 1987.
3. "A Lagrange Explicit Finite Difference Code for Solids, Structural, and Thermohydraulic Analysis," Science Applications International Corporation, Electric Power Research Institute, EPRI NP-2080, November, 1981.
4. W. Heilig and W. Korner, "Some Validation Examples of the STEALTH Code by Experimental Data of Mach Reflection of Shock Waves," Fraunhofer Institut Fur Kurzzeitdynamik, Ernst Mach Institut, Freiburg im Breisgau, Federal Republic of Germany, (undated).
5. A.H. Shapiro, "The Dynamics and Thermodynamics of Compressible Fluid Flow," Volume II, The Ronald Press Company, New York, 1954.
6. W. Heilig, Fraunhofer Institut Fur Kurzzeitdynamik, Ernst Mach Institut, Freiburg im Breisgau, Federal Republic of Germany. Private communications, August and September, 1989.
7. D.A. Matuska, and J.J. Osborn, "HULL Technical Manual," Volume 1, Orlando Technology, Inc., P.O. Box 815, Shalimar, FL, 1986.
8. S. Hikida, R.L. Bell, C.E. Needham, "The SHARC Codes: Documentation and Sample Problems. Volume I: Inviscid Fluid Dynamics," SSS-R-89-9878, S-Cubed, A Division of Maxwell Laboratories, Inc., Albuquerque, NM, September 1988.
9. D.M. Hisley and G.A. Molvik, "Axisymmetric Calculations for the Large Blast/Thermal Simulator (LB/TS) Shock Tube Configuration," BRL-TR-2935, US Army Ballistic Research Laboratory, Aberdeen Proving Ground, MD, September 1988.
10. D.M. Hisley, US Army Ballistic Research Laboratory, Aberdeen Proving Ground, MD, Private communication of data for BRL Report draft, March 1990.
11. D.M. Hisley, "BLAST2D Computations of the Reflection of Planar Shocks from Wedge Surfaces with Comparison to SHARC and STEALTH Results," BRL-TR- draft, to be published, US Army Ballistic Research Laboratory, Aberdeen Proving Ground, MD, May 1990.
12. B.S. Chambers, III, and J.D. Wortman, "Two-Dimensional Shore (Partial Island) Cells for BRL HULL," ARBRL-CR-00497, US Army Ballistic Research Laboratory, Aberdeen Proving Ground, MD, December 1982. (AD#A123357)

13. P.L. Roe, "Approximate Riemann Solvers, Parameter Vectors, and Difference Schemes," *Journal of Computational Physics*, Vol. 43, 1981, pp. 357-372.
14. S.R. Chakravarthy, "A New Class of High Accuracy TVD Schemes for Hyperbolic Conservation Laws," AIAA Paper 85-0363, Reno, NV, January 1985.
15. A.H. Shapiro, "The Dynamics and Thermodynamics of Compressible Fluid Flow," Volume I, The Ronald Press Company, New York, 1953.

<u>No of</u> <u>Copies</u>	<u>Organization</u>	<u>No of</u> <u>Copies</u>	<u>Organization</u>
1	Office of the Secretary of Defense OUSD(A) Director, Live Fire Testing ATTN: James F. O'Bryon Washington, DC 20301-3110	1	Director US Army Aviation Research and Technology Activity ATTN: SAVRT-R (Library) M/S 219-3 Ames Research Center Moffett Field, CA 94035-1000
2	Administrator Defense Technical Info Center ATTN: DTIC-DDA Cameron Station Alexandria, VA 22304-6145	1	Commander US Army Missile Command ATTN: AMSMI-RD-CS-R (DOC) Redstone Arsenal, AL 35898-5010
1	HQDA (SARD-TR) WASH DC 20310-0001	1	Commander US Army Tank-Automotive Command ATTN: AMSTA-TSL (Technical Library) Warren, MI 48397-5000
1	Commander US Army Materiel Command ATTN: AMCDRA-ST 5001 Eisenhower Avenue Alexandria, VA 22333-0001	1	Director US Army TRADOC Analysis Command ATTN: ATAA-SL White Sands Missile Range, NM 88002-5502
1	Commander US Army Laboratory Command ATTN: AMSLC-DL Adelphi, MD 20783-1145	(Class. only) 1	Commandant US Army Infantry School ATTN: ATSH-CD (Security Mgr.) Fort Benning, GA 31905-5660
2	Commander US Army, ARDEC ATTN: SMCAR-IMI-I Picatinny Arsenal, NJ 07806-5000	(Unclam. only) 1	Commandant US Army Infantry School ATTN: ATSH-CD-CSO-OR Fort Benning, GA 31905-5660
2	Commander US Army, ARDEC ATTN: SMCAR-TDC Picatinny Arsenal, NJ 07806-5000	1	Air Force Armament Laboratory ATTN: AFATL/DLODL Eglin AFB, FL 32542-5000 <u>Aberdeen Proving Ground</u>
1	Director Benet Weapons Laboratory US Army, ARDEC ATTN: SMCAR-CCB-TL Watervliet, NY 12189-4050	2	Dir, USAMSAA ATTN: AMXSY-D AMXSY-MP, H. Cohen
1	Commander US Army Armament, Munitions and Chemical Command ATTN: SMCAR-ESP-L Rock Island, IL 61299-5000	1	Cdr, USATECOM ATTN: AMSTE-TD
1	Commander US Army Aviation Systems Command ATTN: AMSAV-DACL 4300 Goodfellow Blvd. St. Louis, MO 63120-1798	3	Cdr, CRDEC, AMCCOM ATTN: SMCCR-RSP-A SMCCR-MU SMCCR-MSI
		1	Dir, VLAMO ATTN: AMSLC-VL-D

<u>No of</u> <u>Copies</u>	<u>Organization</u>	<u>No of</u> <u>Copies</u>	<u>Organization</u>
1	Director of Defense Research & Engineering ATTN: DD/TWP Washington, DC 20301	1	Director National Security Agency ATTN: R15 (E. F. Butala) Ft. George G. Meade, MD 20755
1	Assistant Secretary of Defense (Atomic Energy) ATTN: Document Control Washington, DC 20301	9	Director Defense Nuclear Agency ATTN: CSTI (Tech Lib) DDIR DFSP (Ullrich) NANS OPNA SPSD (Goering/Rohr) SPTD (Kennedy/Hrinishin) Washington, DC 20305
1	Chairman Joint Chiefs of Staff ATTN: J-5 (R&D Div) Washington, DC 20301		
2	Deputy Chief of Staff for Operations and Plans ATTN: Technical Library Director of Chemical and Nuclear Operations Department of the Army Washington, DC 20310	3	Commander Field Command, DNA ATTN: FCPR FCTMOF NMHE/CDR Lund Kirtland AFB, NM 87115
1	Director Defense Advanced Research Projects Agency ATTN: Tech Lib 1400 Wilson Boulevard Arlington, VA 22209	10	Central Intelligence Agency DIR/DB/Standard ATTN: GE-47 HQ Washington, DC 20505
2	Director Federal Emergency Management Agency ATTN: Public Relations Office Technical Library Washington, DC 20472	2	Director Joint Strategic Target Planning Staff JCS ATTN: JLTW TPTP Offut AFB Omaha, NB 68113
1	Director Defense Intelligence Agency ATTN: DT-2/Wpns & Sys Div Washington, DC 20301	1	Commandant Interservice Nuclear Weapons School ATTN: Technical Library Kirtland AFB, NM 87115

<u>No of Copies</u>	<u>Organization</u>	<u>No of Copies</u>	<u>Organization</u>
4	Director US Army Harry Diamond Labs ATTN: SLCHD-NW-RA, (L. Belliveau) SLCHD-NW-P, (Corrigan/Gwaltney) SLCHD-TA-L (Tech Lib) 2800 Powder Mill Road Adelphi, MD 20783-1197	1	Director US Army TRAC - Ft. Lee ATTN: ATRC-L (R. Cameron) Fort Lee, VA 23801-6140
1	Director US Army Laboratory Command USASMO ATTN: SLCSM-SE (J. Orsega) 2800 Powder Mill Road Adelphi, MD 20783-1197	3	Commander US Army Materials Technology Laboratory ATTN: AMXMR-ATL SLCMT-MEC (W. Haskell) SLCMT-MRD-S, (K. Ofstedahl) Watertown, MA 02172-0001
2	Commander US Army CECOM ATTN: AMSEL-RD AMSEL-RO-TPPO-P Fort Monmouth, NJ 07703-5301	1	Commander US Army Strategic Defense Command ATTN: CSSD-H-MPL (Tech Lib) CSSD-H-XM (Dr. Davies) P.O. Box 1500 Huntsville, AL 35807
1	Commander, USACECOM R&D Technical Library ATTN: ASQNC-ELC-I-T, Myer Center Fort Monmouth, NJ 07703-5301	2	Commander US Army Natick Research and Development Center ATTN: AMDNA-D (Dr. D. Sieling) STRNC-UE (J. Calligeros) Natick, MA 01762
1	Director US Army Missile and Space Intelligence Center ATTN: AIAMS-YDL Redstone Arsenal, AL 35898-5500	1	Commander US Army Engineer Division ATTN: HNDED-FD P.O. Box 1500 Huntsville, AL 35807
1	Commander US Army Foreign Science and Technology Center ATTN: Research & Data Branch 220 7th Street, NE. Charlottesville, VA 22901	3	Commander US Army Corps of Engineers Waterways Experiment Station ATTN: CAWES-SS-R (J. Watt) CAWES-SE-R (J. Ingram) CAWES-TL (Tech Lib) P.O. Box 631 Vicksburg, MS 39180-0631

<u>No of</u> <u>Copies</u>	<u>Organization</u>	<u>No of</u> <u>Copies</u>	<u>Organization</u>
1	Commander US Army Research Office ATTN: SLCRO-D P.O. Box 12211 Research Triangle Park, NC 27709-2211	2	Chief of Naval Operations ATTN: OP-03EG OP-985F Department of the Navy Washington, DC 20350
3	Commander US Army Nuclear & Chemical Agency ATTN: ACTA-NAW MONA-WE Tech. Lib. 7500 Backlick Rd, Bldg. 2073 Springfield, VA 22150	1	Chief of Naval Research ATTN: N. Perrone Department of the Navy Arlington, VA 22217
1	Director HQ, TRADOC RPD ATTN: ATRC-RPR (Mr. Radda) Fort Monroe, VA 23651-5143	1	Director Strategic Systems Projects Office ATTN: NSP-43, Tech Library Department of the Navy Washington, DC 20360
1	Director TRAC-WSMR ATTN: ATRC-WC (Mr. Kirby) White Sands Missile Range, NM 88002-5502	1	Commander Naval Electronic Systems Command ATTN: PME 117-21A Washington, DC 20360
1	Director US Army TRADOC Center ATTN: ATRC Fort Leavenworth, KS 66027-5200	1	Commander Naval Facilities Engineering Command ATTN: Technical Library Washington, DC 20360
1	Commander US Army Test & Evaluation Command Nuclear Effects Laboratory ATTN: STEWS-TE-NO, (Dr. J.L. Meason) P.O. Box 477 White Sands Missile Range, NM 88002	1	Commander Naval Sea Systems Command ATTN: Code SEA-62R Department of the Navy Washington, DC 20362-5101
		1	Officer-in-Charge Naval Construction Battalion Center Civil Engineering Laboratory ATTN: Tech Lib Port Hueneme, CA 93041
		1	Commanding Officer Naval Civil Engineering Laboratory ATTN: Code L51 (J. Tancreto) Port Hueneme, CA 93043-5003

<u>No of Copies</u>	<u>Organization</u>	<u>No of Copies</u>	<u>Organization</u>
1	Commander David W. Taylor Naval Ship Research & Development Command ATTN: Code 522 (Lib Div) Bethesda, MD 20084-5000	2	Air Force Armament Laboratory ATTN: AFATL/DOIL AFATL/DLYV Eglin AFB, FL 32542-5000
1	Commander Naval Surface Warfare Center ATTN: Code DX-21 (Library) Dahlgren, VA 22448-5000	1	AFESC/RDCS ATTN: Paul Rosengren Tyndall AFB, FL 32403
1	Officer in Charge White Oak Warfare Center Detachment ATTN: Code E232 (Tech Library) 10901 New Hampshire Ave Silver Spring, MD 20903-5000	1	RADC (EMTLD/Docu Library) Griffiss AFB, NY 13441
1	Commanding Officer White Oak Warfare Center ATTN: Code WA501 (NNPO) Silver Spring, MD 20902-5000	3	Air Force Weapons Laboratory ATTN: NTE NTED NTES Kirtland AFB, NM 87117-6008
1	Commander (Code 533) Naval Weapons Center Tech Library China Lake, CA 93555-6001	1	Commander-in-Chief Strategic Air Command ATTN: NRI-STINFO Lib Offutt AFB, NB 68113
1	Commander Naval Weapons Evaluation Fac ATTN: Document Control Kirtland AFB, NM 87117	1	AFIT ATTN: Tech Lib (Bldg. 640/B) Wright-Patterson AFB, OH 45433
1	Commander Naval Research Laboratory ATTN: Code 2027, Tech Library Washington, DC 20375	1	FTD/NIIS Wright-Patterson AFB, OH 45433
1	Superintendent Naval Postgraduate School ATTN: Code 2124, Tech Library Monterey, CA 93940	1	U.S. Department of Energy Idaho Operations Office ATTN: Spec Programs (J. Patton) 785 DOE Place Idaho Falls, ID 83402
		2	Director Idaho National Engineering Laboratory EG&G Idaho Inc. ATTN: Mr. R. Guenzler, MS-3505 Mr. R. Holman, MS-3510 P.O. Box 1625 Idaho Falls, ID 83415

<u>No of</u> <u>Copies</u>	<u>Organization</u>	<u>No of</u> <u>Copies</u>	<u>Organization</u>
1	Director Lawrence Livermore Lab. ATTN: Tech Info Dept L-3 P.O. Box 808 Livermore, CA 94550	1	Director NASA-Ames Research Center Applied Computational Aerodynamics Branch ATTN: MS 202-14, Dr. T. Holtz Moffett Field, CA 94035
4	Director Los Alamos National Laboratory ATTN: Mr. Th. Dowler, MS-F602 Dr. J. Chapyak, MS-F664 Doc Control for Reports Library P.O. Box 1663 Los Alamos, NM 87545	2	Applied Research Associates, Inc. ATTN: N.H. Ethridge J. Keefer P.O. Box 548 Aberdeen, MD 21001
3	Director Sandia Laboratories ATTN: Doc Control 3141 Mr. C. Cameron, Div 6215 Mr. A. Chabai, Div 7112 P.O. Box 5800 Albuquerque, NM 87185-5800	1	Aerospace Corporation ATTN: Tech Info Services P.O. Box 92957 Los Angeles, CA 90009
1	Director Sandia Laboratories Livermore Laboratory ATTN: Doc Control for Tech Library P.O. Box 969 Livermore, CA 94550	1	Agbabian Associates ATTN: M. Agbabian 250 North Nash Street El Segundo, CA 90245
1	Director National Aeronautics and Space Administration ATTN: Scientific & Tech Info Fac P.O. Box 8757, BWI Airport Baltimore, MD 21240	1	Applied Research Associates, Inc. ATTN: R. L. Guice 7114 West Jefferson Ave., Suite 305 Lakewood, CO 80235
1	Director NASA-Langley Research Center ATTN: Tech Lib Hampton, VA 23665	1	The Boeing Company ATTN: Aerospace Library P.O. Box 3707 Seattle, WA 98124
		1	California Research & Technology, Inc. ATTN: M. Rosenblatt 20943 Devonshire Street Chatsworth, CA 91311
		1	Carpenter Research Corporation ATTN: H. Jerry Carpenter 27520 Hawthorne Blvd., Suite 263 P.O. Box 2490 Rolling Hills Estates, CA 90274

<u>No of</u> <u>Copies</u>	<u>Organization</u>	<u>No of</u> <u>Copies</u>	<u>Organization</u>
1	Dynamics Technology, Inc. ATTN: D. T. Hove Suite 300 21311 Hawthorne Blvd. Torrance, CA 90503	2	Kaman-TEMPO ATTN: DASIAC Don Sachs P.O. Drawer QQ 816 State Street Santa Barbara, CA 93102
2	FMC Corporation Advanced Systems Center ATTN: Mr. J. Drotleff Ms. C. Krebs, MDP95 2890 De La Cruz Boulevard Box 58123 Santa Clara, CA 95052	1	Ktech Corporation ATTN: Dr. E. Gaffney 901 Pennsylvania Avenue, N.E. Albuquerque, NM 87111
1	Goodyear Aerospace Corporation ATTN: R. M. Brown, Bldg 1 Shelter Engineering Litchfield Park, AZ 85340	1	Lockheed Missiles & Space Co. ATTN: J. J. Murphy, Dept. 81-11, Bldg. 154 P.O. Box 504 Sunnyvale, CA 94086
4	Kaman AviDyne ATTN: Dr. R. Ruetenik (2 cys) Mr. S. Criscione Mr. R. Milligan 83 Second Avenue Northwest Industrial Park Burlington, MA 01830	2	McDonnell Douglas Astronautics Corporation ATTN: Robert W. Halprin K.A. Heinly 5301 Bolsa Avenue Huntington Beach, CA 92647
3	Kaman Sciences Corporation ATTN: Library P. A. Ellis F. H. Shelton 1500 Garden of the Gods Road Colorado Springs, CO 80907	1	Orlando Technology, Inc. ATTN: Mr. D. Matuska P.O. Box 855 Shalimar, FL 32579
1	Kaman Sciences Corporation ATTN: Mr. F. W. Balicki 6400 Uptown Boulevard N.E. Suite 300 Albuquerque, NM 87110	2	Physics International Corporation 2700 Merced Street San Leandro, CA 94577
		2	R&D Associates ATTN: Technical Library Dr. Allan Kuhl P.O. Box 9695 Marina Del Rey, CA 90291
		1	R&D Associates ATTN: G.P. Ganong P.O. Box 9377 Albuquerque, NM 87119

<u>No of</u> <u>Copies</u>	<u>Organization</u>	<u>No of</u> <u>Copies</u>	<u>Organization</u>
2	Science Applications, Inc. ATTN: W. Layson John Cockayne P.O. Box 1303 1710 Goodridge Drive McLean, VA 22102	3	S-CUBED A Division of Maxwell Laboratories, Inc. ATTN: Technical Library R. Duff K. Pyatt PO Box 1620 La Jolla, CA 92037-1620
1	Science Applications International Corp. ATTN: Mr. J. Guest 2109 Air Park Rd, SE Albuquerque, NM 87106	1	Texas Engineering Experiment Station ATTN: Dr. D. Anderson 301 Engineering Research Center College Station, TX 77843
1	Sparta, Inc. Los Angeles Operations ATTN: I. B. Osofsky 3440 Carson Street Torrance, CA 90503	1	TRW Ballistic Missile Division ATTN: H. Korman, Mail Station 526/614 P.O. Box 1310 San Bernadino, CA 92402
1	Sunburst Recovery, Inc. ATTN: Dr. C. Young P.O. Box 2129 Steamboat Springs, CO 80477	1	Battelle Memorial Institute ATTN: Technical Library 505 King Avenue Columbus, OH 43201
1	Sverdrup Technology, Inc. ATTN: R. F. Starr P.O. Box 884 Tullahoma, TN 37388	1	California Institute of Technology ATTN: T. J. Ahrens 1201 E. California Blvd. Pasadena, CA 91109
3	SRI International ATTN: Dr. G. R. Abrahamson Dr. J. Gran Dr. B. Holmes 333 Ravenswood Avenue Menlo Park, CA 94025	2	Denver Research Institute ATTN: Mr. J. Wisotski Technical Library P.O. Box 10758 Denver, CO 80210
2	S-CUBED A Division of Maxwell Laboratories, Inc. ATTN: C. E. Needham Dr. Lynn Kennedy 2501 Yale Blvd., SE Albuquerque, NM 87106	1	Massachusetts Institute of Technology Aeroelastic and Structures Research Laboratory ATTN: Dr. E. A. Witmer Cambridge, MA 02139

<u>No of</u> <u>Copies</u>	<u>Organization</u>	<u>No of</u> <u>Copies</u>	<u>Organization</u>
1	Massachusetts Institute of Technology ATTN: Technical Library Cambridge, MA 02139	<u>Aberdeen Proving Ground</u> 1	Cdr, USATECOM ATTN: AMSTE-TE-F (L. Teletski)
2	New Mexico Engineering Research Institute (CERF) University of New Mexico ATTN: Dr. J. Leigh Dr. R. Newell P.O. Box 25 Albuquerque, NM 87131	1	Cdr, USATHMA ATTN: AMXTH-TE
1	Northrop University ATTN: Dr. F. B. Safford 5800 W. Arbor Vitae St. Los Angeles, CA 90045		
4	Southwest Research Institute ATTN: Dr. W. E. Baker A. B. Wenzel Dr. C. Anderson S. Mullin 6220 Culebra Road San Antonio, TX 78284		
1	Stanford University ATTN: Dr. D. Bershader Durand Laboratory Stanford, CA 94305		
3	University of Maryland Department of Mechanical Engineering ATTN: Dr. W. Fourney Dr. R. Dick Dr. J. Williams College Park, MD 20742		

INTENTIONALLY LEFT BLANK.

USER EVALUATION SHEET/CHANGE OF ADDRESS

This Laboratory undertakes a continuing effort to improve the quality of the reports it publishes. Your comments/answers to the items/questions below will aid us in our efforts.

1. BRL Report Number BRL-TR-3153 Date of Report SEPTEMBER 1990

2. Date Report Received _____

3. Does this report satisfy a need? (Comment on purpose, related project, or other area of interest for which the report will be used.) _____

4. Specifically, how is the report being used? (Information source, design data, procedure, source of ideas, etc.) _____

5. Has the information in this report led to any quantitative savings as far as man-hours or dollars saved, operating costs avoided, or efficiencies achieved, etc? If so, please elaborate. _____

6. General Comments. What do you think should be changed to improve future reports? (Indicate changes to organization, technical content, format, etc.) _____

**CURRENT
ADDRESS**

Name

Organization

Address

City, State, Zip Code

7. If indicating a Change of Address or Address Correction, please provide the New or Correct Address in Block 6 above and the Old or Incorrect address below.

**OLD
ADDRESS**

Name

Organization

Address

City, State, Zip Code

(Remove this sheet, fold as indicated, staple or tape closed, and mail.)

-----FOLD HERE-----

DEPARTMENT OF THE ARMY

Director
U.S. Army Ballistic Research Laboratory
ATTN: SLCBR-DD-T
Aberdeen Proving Ground, MD 21005-5066
OFFICIAL BUSINESS



**NO POSTAGE
NECESSARY
IF MAILED
IN THE
UNITED STATES**

BUSINESS REPLY MAIL
FIRST CLASS PERMIT No 0001, APG, MD

POSTAGE WILL BE PAID BY ADDRESSEE

Director
U.S. Army Ballistic Research Laboratory
ATTN: SLCBR-DD-T
Aberdeen Proving Ground, MD 21005-9989



-----FOLD HERE-----